The discharge dynamics of distributaries of the Ganges as determined with object-based image analysis

Master of Science Thesis
in Physical Geography

Philip Kraaijenbrink – 3132102

Supervisors:
E.A. Addink
M.G. Kleinhans

Faculty of Geosciences
Utrecht University
May 2012

ABSTRACT

In this thesis, insight is gained in the discharge distribution and channel evolution of meandering distributaries in the Ganges Delta by the development of a method that extracts channels from satellite imagery and that analyses the channel geometry. This focus is part of a project of the Utrecht University Physical Geography Department about the Ganges-Brahmaputra delta and is aimed at unravelling a small part of the delta to gain knowledge about the larger scale. To support the methodology and to compare and interpret the results of this study a comprehensive literature overview is presented additionally.

The image analysis is performed with eCognition Developer 8 software and comprises segmenting a Landsat 5 TM image using six different segmentation scales. Meander objects are delineated by classifying the objects based on shape characteristics. The small meander objects from the different segmentation scales are merged into one dataset containing objects that represent large parts of the channel network. The skeletons of the objects are processed to obtain channel centerlines. The geometry of the centerlines is analysed in MATLAB to obtain inflection points that are used to approximate meander wavelength. This is used to determine discharges and sinuosities of the channels. Larger scale meandering present in the general course of numerous rivers in the area is analysed by fitting a cubic spline through the inflection points and determining the inflections of the spline.

The methods that are developed in the study are successfully able to nearly automatically delineate meander objects, merge objects into large channel representations and obtain channel centerlines. Furthermore, it is proven that the used extraction methods yield the possibility to obtain river and discharge dynamics by analysing the centerline geometry.

The discharge data that results from the analysis seems relatively accurate, taking into account the many potential sources of error of the methods that are used. However, the lack of ground truth of the rivers in the study area causes the accuracy to be uncertain. Therefore further research is needed to calibrate the discharge calculation methods. In terms of the river evolution in the study area it is confirmed that the Hooghly and the Bhairab have been the main Ganges course. For the Jalangi and Gorai this could not be confirmed.

PREFACE

This thesis is written as a part of the Master of Science degree programme in Physical Geography at the Utrecht University, Netherlands. The specific MSc track that I followed prior to the elaboration of this thesis is Natural Hazards and Earth Observation. The thesis is the report on the research stage in the final year of the MSc programme. The research and thesis writing were performed in a period of one semester.

The subject of the research is a continuation of the bachelor research I performed in 2010. Already interested by geo-related image analysis, my interest was drawn to the new possibilities of object-based image analysis that my supervisors pointed out to me. Many new possibilities of object-based image analysis were presented in the past years and I believe there are many more possibilities to appear in the future. I am content that I have been a part of this development.

My MSc research is supervised by dr. E.A. Addink and dr. M.G. Kleinhans, both researchers and lecturers at the department of Physical Geography at the Utrecht University. I would like to thank them both for their good support and supervision during my research. Furthermore, I would like to thank Filip Schuurman for the provided mathematical insight in channel line analysis.

TABLE OF CONTENTS

LIST OF FIGURES

LIST OF TABLES

1. INTRODUCTION

1.1 Background and problem definition

1.1.1 The Ganges-Brahmaputra Delta

Located in the Bengal region in Asia, the Ganges-Brahmaputra delta is one of the largest in the world, i.e. it covers an area of ca. 105 000 km^2. Due to the large catchments of the rivers (fig. 1) as well as the local monsoon climate, the total discharge that is transported through the delta's distributaries towards the Bay of Bengal is enormous, as the annual mean is about 40 000 m^3/s (Sarkar et al., 2009). However, the discharge of the delta varies greatly around the year. This is caused by the climate that, though it is considered to be one of the wettest in the world, is very erratic. Almost all of the rainfall occurs during the summer monsoon in the months June to October (Ahmed & Karmakar, 1993).

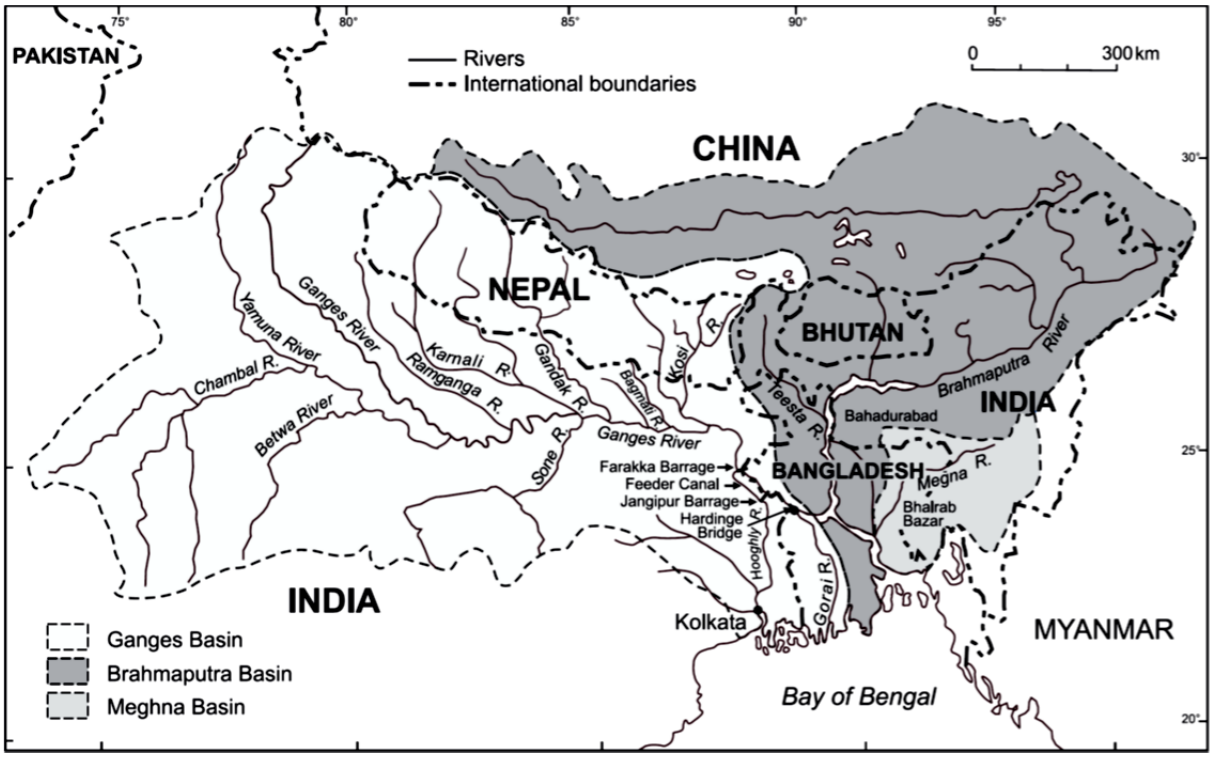

Figure 1: The Ganges-Brahmaputra catchment (Mirza, 2004).

1.1.2 The Holocene development of the Ganges Delta

Studies on the Late Quaternary geology of the Ganges delta state Bangladesh's present coastline was greatly influenced by a rapid Holocene transgression and on-going tectonic subsidence (Umitsu, 1993). The resulting net increase in base level elevation resulted in a strong depositional character of the delta and a fast aggradation of the delta plain. Such a

depositional regime, especially in combination with the large discharges and extremely varying discharge peaks, provides a dynamic delta in terms of shifting channel courses (Slingerland & Smith, 2004). These shifts, called avulsions, can have all sorts of appearances and (time) scales, from complete and partial channel abandonment to small meander cut-offs.

Supported by multiple geological and historical records, a generally accepted thought on the main course of the Ganges is that it has avulsed numerous times towards the east (Goodbred Jr. & Kuehl, 2000). For example, the main course was once following the north-south oriented Hoogly-Bhagirathi channel and passed the major city of Kolkata (formerly Calcutta). Nowadays however, a barrage near Farakka ensures Kolkata is provided with water as the main course flows towards the east instead of the south (Mirza, 1997). Further downstream on the present eastbound course there are some more north-south oriented distributaries that are suggested to have been the Ganges main course for at least some time (Sarker, 2005): the Jalangi, the Bhairab/Mathabanga, the Gorai-Madhumathi, the Kumar and the Ariel Khan. However there are still large uncertainties about the exact evolution of these delta branches.

1.1.3 The study of bifurcation evolution

To get understanding of the evolution and shifting of the Ganges courses and that of its distributaries it is important to know the present and past river dynamics. Conversely, knowledge about time scales and river patterns related to the dynamics of bifurcations are important inputs in determining the delta evolution (Kleinhans et al., 2008). Understanding these processes may cause major improvements to be made in many fields. Not only could the general scientific knowledge about avulsions and bifurcations be improved, but also more practical knowledge about for example flooding risks and shipping capabilities. These are both of great importance in the Ganges Delta, as severe flooding occurs often and the infrastructure is of relatively poor quality (Höfer & Messerli, 2006).

Because a complete and thorough understanding of the long term river dynamics and the related evolution of channels in general is not available (Camporeale et al., 2005), research based on all kinds of different approaches continues on this topic. There are for example physicists, hydrologist, sedimentologists, geologists and engineers working on this subject. In the field of remote sensing there is much research performed as well (Mertes, 2002), as geoscientists more and more realize that viewing and analysing satellite images provides a quick and feasible way to determine and understand geospatial and temporal patterns. This study uses the remote sensing approach as well by using advanced image analysis techniques.

1.1.4 Developments in image analysis

The progress in computer hard and software technologies of the last decades made the analysis of satellite imagery easily accessible to scientists. Advanced image processing algorithms are widely used to explore the image data thoroughly to retrieve 'hidden' information about the pixels present in an image. For a long period of time the image analysis was performed on a pixel level only. Though many studies have utilized such methods with great success, the expert knowledge of a human was always needed to see the pattern in the pixel-wise results (Lillesand et al., 2003). The more recently developed object-based image analysis provides improvements as it comprises the semantic analysis of hierarchical groups of pixels (Blaschke, 2010).

The major improvement with this technology is that not the spectral properties of single pixels are analysed but those of objects that are defined by shape as well, a process that comes much closer to the image analysis approach of the human brain. Furthermore, the created objects hold attributes that can be analysed to obtain results that are far beyond pixel analysis capabilities. The attributes for instance can describe the objects' spectral, shape or relational characteristics.

1.1.5 Image analysis of rivers

Channel delineation in a satellite image may seem easy with traditional pixel-based image analysis, but it is actually impossible. As water has a distinct spectral reflectance, water pixels are easily distinguished from non-water pixels (Lillesand et al., 2003). However no distinction can be made between lakes or channels, and overgrown or fossil channels cannot be delineated. The biggest problem though lies in the fact that a true channel will never be delineated, only its pixels. To identify these pixels as a channel, a subjective human view remains necessary, just as it would on a non-processed satellite image.

To provide a solution to this deficiency, the use of object-based image analysis for the delineation of as well fossil as active meanders is assessed (Addink & Kleinhans, 2008). The presented object approach is able to delineate meanders as shapes in the image. In addition, the resulting objects contain attributes that hold information on their metrics. This is suggested to be able to provide a way to determine discharge dynamics by using empirical relations between meander geometry and discharge.

The latter was assessed by Kraaijenbrink (2010) who shows that there are still major difficulties in the method. Different object scales are needed to obtain a good coverage of the channel network in the study area. Though various different approaches were assessed, the presence of the multiple datasets with many small objects hampered a proper analysis of

the channel objects' metrics. The geometry information held within the small objects was too limited and it did not describe the channel geometry sufficiently to calculate realistic discharges.

1.2 Research aim

The preceding section shows the need for spatial and temporal data of discharges to improve our understanding of river dynamics. An assessed approach that tries to gain such data by using image analysis techniques is presented, though the methods used were not able to yield proper results. The framework of the research remains promising however, because if proper discharge results are obtained it will provide a feasible quick way of determining river discharges in an area.

This research therefore aims at substantially improving this approach by establishing a method that does yield useful relative discharge data. Furthermore it is aimed at improving the knowledge about the river dynamics of the study area by interpreting the results, which may lead to an improved understanding of river dynamics in general. The method is aimed to be universally applicable to naturally meandering river systems.

The main question that is answered by the research is:

- ***What are the discharge dynamics of the meandering distributaries in the Ganges Delta, as can be derived from satellite images using object-based image analysis*?**

Additional questions that are used to answer the main question are:

- *How can the sets of meander objects that result from the different segmentation levels be combined to form one set of objects?*
- *How can individual meander objects be combined into a larger part of the channel?*
- *How can discharge be derived from the resulting channel objects?*
- *What are the river dynamics that can be derived from the analysis results?*

1.3 Guide to the reader

The outline of this thesis is as follows. First a literature review is presented to clarify the aim of this study and to provide a framework for the methods, discussion and terminology presented in this thesis. River meandering and related aspects are discussed as well as past and current river dynamics in the study area. Also relevant information about image analysis techniques is presented, in particular object-based image analysis, as well as a comprehensive view on the river delineation and analysis that has been performed in prior research.

Then first the basic methodology is presented that describes the study area, the used data and data pre-processing. Then the methodology that is developed in this study is explained in terms of meander delineation, object processing, channel network enhancements and geometry analysis. It is presented in a step by step manner and conceptualizes the work that is performed to obtain the results.

Subsequently, the results that follow from the developed methods are presented. This section mainly comprises tables, maps and other figures that show the intermediate and final results. These are accompanied by concise descriptions and explanations of directly notable features in the figures or tables.

The discussion section explains the issues that are inherent to the used method and tries to elaborate on the research questions and aim of the study. This is performed by discussing and explaining patterns, relationships and trends that are found in the results, using various hypotheses. Likely causes for the patterns are discussed as well as agreements or disagreements with literature. The significance and implications of the results to other scientific research and a brief overview of proposed further research are presented. Brief, point-wise conclusions that follow from the discussion are presented in the subsequent conclusion section.

A list of references is presented at the final pages of the thesis. Appendices are included digitally on a DVD. They comprise a set of large maps of figures that are presented in the thesis, the MATLAB script used to perform the river dynamics calculations, various data files and the digital version of this thesis.

2. LITERATURE REVIEW

2.1 Introduction

This review provides an overview of information presented in existing literature that is relevant to the research presented in this thesis, as well as other important background information that is needed for discussing and interpreting the research results. It is aimed at clarifying the relations between the presented research and conducted research by identifying the gaps that are present in the current understanding of related processes and available methods. Furthermore it explains all terminology that is involved with the proposed research. Questions that are answered in this review to achieve these aims are:

- What is known about the evolution and dynamics of meanders?
- What is the role of bifurcations and avulsions in river evolution?
- How can the river planform geometry be defined and used in research?
- What is known about the evolution and dynamics of the rivers in the study area?
- How can satellite image analysis be used for the determination of discharge?

The outline of this review is as follows. First an overview of meandering rivers and about processes related to meandering rivers is presented. Known methods for the characterization of the meander planform, theory on meander evolution, theory on bifurcations and empirical relations between meander geometry and river dynamics are presented. Subsequently an overview of the evolution and dynamics of the rivers that are located in the study area of this research is presented. Then a general overview of the image analysis techniques related to the delineation of meanders is discussed as well as a method to obtain discharge values using image analysis. To conclude the answers to the research questions will be discussed, focusing on the gaps present in the literature.

2.2 Meandering nature of rivers

The rivers that are present on earth can be classified in many different ways. An example of one of these classifications is shown in figure 2. The differences between river types are caused by various factors, e.g. the type of substrate, the amount of sediment input, the discharge regime and the bed slope (Eaton et al., 2010; Kleinhans, 2010). Though these differences are evident, there are distinct similarities as well. One of these is the fact that all natural river channels show a change in curvature in a frequent sinuous manner, albeit to various extents. These curving bends that occur are referred to as meanders.

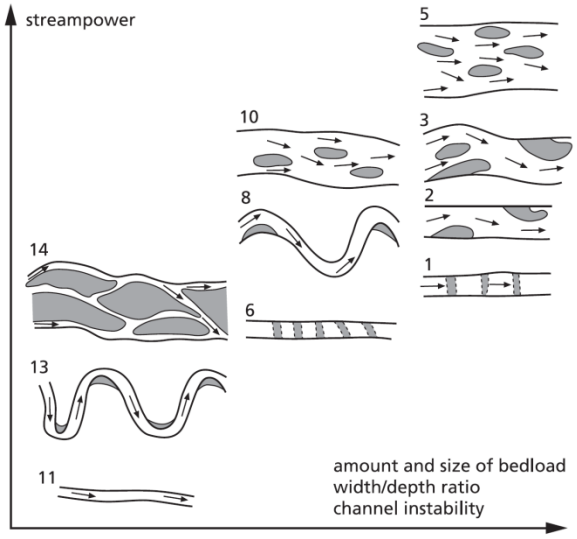

Figure 2: Example of a river classification showing existing river types (after Ferguson, 1987).

The initiation of the curves has long been debated by geomorphologists and various causes were proposed. Examples are the Coriolis force, bank erosion due to local disturbances, theory of most probable path and alternate bars (Rhoads & Welford, 1991). More recently the bed shaping effects of horizontal bursts caused by small bed perturbations were suggested to be an important factor in the initiation of channel curvature (Da Silva, 2006).

The general idea about meander initiation is however based on the feedback related to the bar-bend theory and bank stability. The balance between floodplain formation and bank erosion determines channel width and depth, which in turn determines the bar pattern. The bar pattern has an effect on the bank erosion, which is controlled by the bank stability as well (Kleinhans, 2010). This knowledge about the initiation provides a framework for better understanding of all the complex processes related to channel curvature.

2.3 Planform of meandering rivers

2.3.1 The basic meander planform

As the curving nature of channels is a distinct characteristic, many studies have tried to define it by parameterizing the river planform (Bridge, 2003), i.e. the geometry of the top view. The true meandering river type (comparable to stream type 8 and 13 in fig. 2) is characterized by a single, highly curved channel. For clarity reasons, an idealized geometry that resembles this river type is generally used in the parameterization, though the meander bends can have a significantly more complex planform. The following paragraphs present the basic meander planform parameters as well as other approaches for the mathematical characterization of meander curvature.

The basic description of a meander is based on the characteristics of a sine function (Williams, 1986). The definition of the parameters wavelength and amplitude are therefore analogous to that of a sine. Further important to mention are the channel width, the channel belt width and the radius of curvature. These and more meander related parameters are shown schematically in figure 3. Together the parameters are nearly able to describe the full geometry of meanders. One more parameter is needed, which the maximum angle the upward and downward paths make at the inflexion point (Langbein & Leopold, 1966). Examples of different angles are presented in figure 4. An additional parameter that is widely used in literature is the sinuosity, i.e. the channel length divided by the downvalley, or the channel belt length (Leopold et al., 1957).

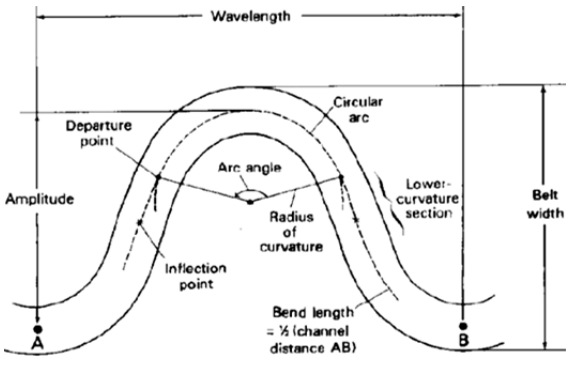

Figure 3: Standard parameters describing meander geometry (Williams, 1986).

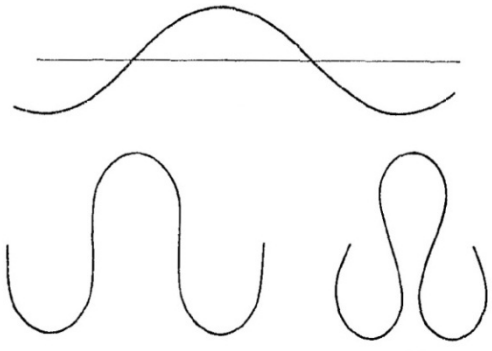

Figure 4: Examples of possible angles between upward and downward paths (Langbein & Leopold, 1966).

The described parameterization holds for single, ideal meanders. Meandering rivers on earth however show significant variability in the geometry of curves along their courses. Various causes lie at the root of this, e.g. changes in substrate, bank cohesiveness or sediment load. To be able to make a comparison between different rivers and to be able to do statistical analyses, a meaningful statistical characterization is needed. Therefore numerous researchers have proposed to use averages, medians, modes or distributions of the parameters (Bridge, 2003; Dury, 1976; Leopold & Wolman, 1960; Williams, 1986)

These values are all difficult to calculate, as many bends in a river have to be sampled to obtain a precise value. It is also hard to say which statistical value is best to describe meanders. This problem resulted in the use of many different statistical methods different studies, strongly limiting comparability. To date there is still the need for a good statistical measure that describes meandering rivers that is universally adopted and used in the scientific community.

2.3.2 Determination of curvature

The idea that meander migration is closely related to local channel curvature established the need for accurate parameterizations of the meander curvature. The classical methods namely have significant limitations. One of the methods comprises the fitting of a circular arc to an individual meander bend to determine the radius of curvature (Brice, 1974; Crosato, 2007; Hickin, 1974). Assumed with the use of this method is that the curvature is uniform over an individual bend and discontinuous from one bend to another. Furthermore it involves subjectivity in identifying the centres of radius (Güneralp & Rhoads, 2008). Another classic method is to use mathematical functions, such as sines and polynomials, to represent the curvature of the bends (R. I. Ferguson, 1975; Leopold & Wolman, 1960). The functions are however unable to handle the common irregular patterns that meander bends have with a significant precision.

Recently a study by Camporeale (2005) that focusses on developing a numerical meander evolution model, suggests a new geometric framework to describe meander curvature. With his method, points that represent the channel's inner bend line are linearly linked at a small distances along the channel ($\mathrm{d}S$). The coordinates of the points are described by r, which is the distance from the origin of the x,y coordinate system (fig. 5). The curvature is then calculated using:

$$C = |\partial^2 r / \partial s^2| \quad (1)$$

As the framework is used in a model environment, $\mathrm{d}S$ can be set to be infinitely small to increase accuracy of the calculations. For a non-model application of the framework however, the precision of the method strongly depends on the number of data points available for a river centerline as that defines the size of $\mathrm{d}S$. Regridding the channel centerline can be applied to remedy this problem. This has to be performed using curved splines, as linear interpolation will yield consecutive centerline points in between the old points that have no curvature.

Another approach to determine the curvature is a method that directly fits a parametric cubic spline through the channel points (fig. 6). From the combination of mathematical functions that is used for (parts of) the spline, the curvature can be calculated at any point along the spline (Güneralp & Rhoads, 2008). This method is able to precisely determine channel geometry and related curvature, even of highly irregular meandering channels.

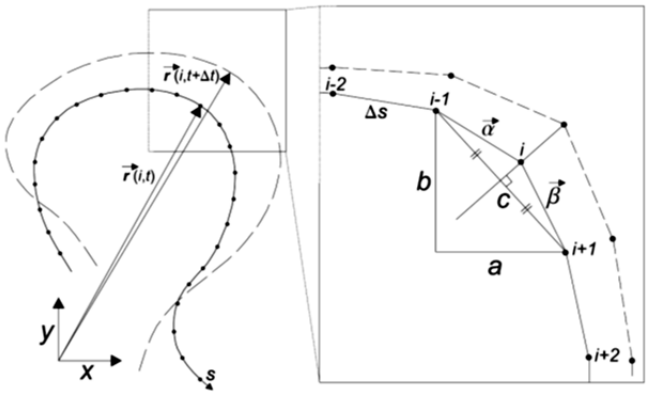

Figure 5: The geometric framework used in the meander evolution model (Camporeale et al., 2005).

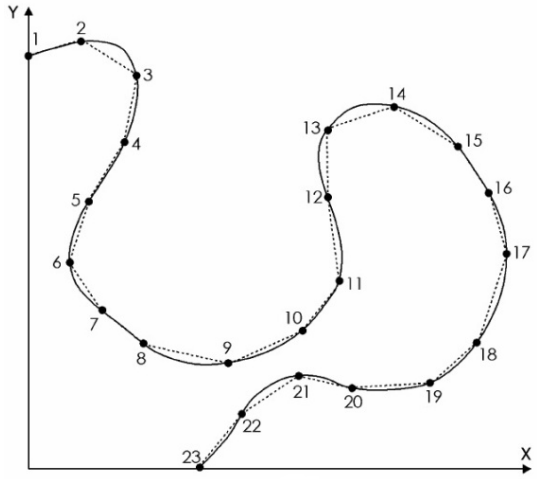

Figure 6: Plot of channel points with a linear connection (dotted line) and with a cubic spline (continuous line) (Güneralp & Rhoads, 2008).

A simpler, more straightforward definition and calculation of the curvature is presented by Chen & Duan (2006). The definition is developed as a part of a framework of a numerical meander widening model. They use the length between two points along the channel centerline $\mathrm{d}S$ and the angle $\mathrm{d}\theta$ between those points (fig. 7) to calculate the curvature C using:

$$C(s) = \frac{\mathrm{d}\theta}{\mathrm{d}S} \tag{2}$$

The radius of curvature at that specific point is then defined as

$$r = \frac{1}{C} \tag{3}$$

Compared to the previous mentioned methods, this one is more easy to use outside of a model environment to define the curvature of any digitized meander. It only uses the channel centerline, which is easier to digitize than the inner bend line that is used in the framework of Camporeale (2005). This is valid for both manual as automatic digitalization, as is does require resp. subjectivity in determining the inner bend and advanced algorithms. Compared to the method of Güneralp & Rhoads (2008) it is easier and more computationally efficient as it does not require splines to be calculated.

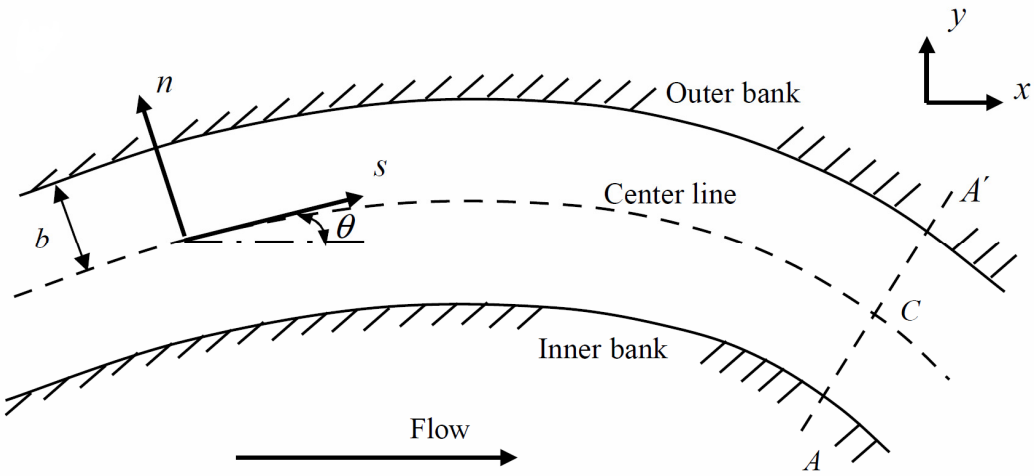

Figure 7: A sketch showing the parameters of a simpler framework used to define curvature (Chen & Duan, 2006).

2.4 Evolution of meandering rivers

The evolution of the planform of a natural unconfined meander is caused by the forces exerted by water flow. Changes in the dynamics, for instance the discharge regime or sediment input, can have major effects on the water flow and consequently on the planform as well. This section presents a concise overview of the major processes that are related to the planform evolution of meanders.

2.4.1 Relation between morphology and processes

Meander planform evolution is caused by dynamics within the water flow caused by the forcing of the inert water through its channel. It is part of a complex feedback that acts within the self-organizing system of river channels. Though not all of the involved feedbacks between process and form that are present in the system are yet entirely clear (Camporeale et al., 2005), well developed principles are available.

The meander forming feedback is caused by pressure differences within the water flow that are due to forcing of the water against the curved bank or small irregularities in the river bed. The pressure differences result in differences in the directions and velocity of the water particles present in the flow, i.e. a non-uniform flow. Consequently, the shear stress that is exerted on the river bed by the water particles is non-uniform as well, causing patterns of erosion and deposition of bed and bank material. It results in changes of the channel morphology (Kleinhans & van den Berg, 2011), which in turn results in internal changes in the water flow to close the feedback.

2.4.2 Processes that drive planform evolution

In terms of velocity, the water in the outer bend flows faster as it has to travel over a longer distance. Due to the bed scour that this generates the channel is deeper there, i.e. the thalweg, resulting in less friction in the local flow. At the same time, the inner bend experiences a slower flow that results in deposition of the coarser fractions of transported sediment (Bridge, 2003). On top, there is a secondary flow developed that increases the pattern of erosion and deposition, the so-called helicoidal flow (fig. 8).

Figure 8: Schematic cross-section of the helicoidal flow in a meander bend and at the inflection point, resp. left and right (Rhoads & Welford, 1991).

The helicoidal flow is caused by the raised water levels in the outer bend that are due to the inertia of the water flow. The raised water level, in combination with the deeper water column above the thalweg, increases water pressure and consequently causes a lateral near bed flow (Rhoads & Welford, 1991). This flow transports sediment laterally from the thalweg towards the channel banks. The process increases the development of the inner bend point bars and causes erosion of the outer bank levees by undercutting. These outer bank levees are formed during floods when there is a large flow deceleration of the overbank flow in the outer bend due to diffusion. This decreases transport capacity and causes deposition of relatively coarse sediment (Bridge, 2003).

2.4.3 Migration of meandering channels

In figure 9 six subsequent stages of meander bend evolution are shown. The change in planform over time is caused by the higher flow velocity of the outer bank as well as the helicoidal flow (Rhoads & Welford, 1991). Both result in undercutting of the outer bends and the related lateral migration. However, the inertia of the water acts on the outer bank both at and right after the point of highest curvature. This causes an additional longitudinal migration to take place in the downvalley direction (Brice, 1974; Da Silva, 2006)(Brice, 1974).

2.4.4 Development of oxbow lakes

Over time the meanders will migrate in such a way that upward and downward paths will be positioned very closely to each other (Hooke, 1984). During floods a direct flow over the levee can then develop an interchannel current at this location. This current scours out a cut-off channel that gradually develops to become the main channel. It can also occur that the meander necks touch, causing a failure of the shared levee. During the cut-off process the old meander loop encounters a gradual decrease of flow velocity. Consequently deposition of sediment occurs in a fining upwards sequence (Constantine & Dunne, 2008), until the old meander gets closed off completely to form an oxbow lake (fig. 10). The timescale related to these events can vary from days to decades. Through this system a river can develop a large number of fossil meander loops that are located in the floodplains around the main channel. It is not unusual for a river to cut through its own channel depositions and to reoccupy the former channel (Aslan et al., 2005).

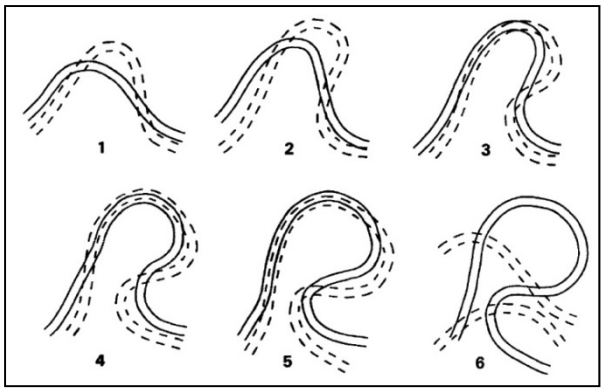

Figure 9: The development of a meander loop in six stages (Hooke, 1984).

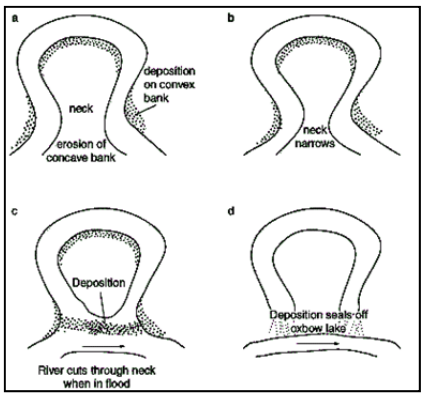

Figure 10: The development of an oxbow lake (Bangladesh Studies, 2006).

2.4.5 Effects of changes in river dynamics

If the long-term river dynamics change, the internal forces of the water flow will change as well. As the shear stress exerted on the river bed and bank toe is related to the flow velocity by a power of at least two (Kleinhans, 2005), an increase in the peak discharges will cause a large increase in sediment transport rates and consequently a fast change of the geomorphology and the planform. Conversely, a decrease in peak discharges causes a significant deceleration or even stagnation of the change in channel morphology.

2.4.6 Discharge related to channel morphology

The principle presented in § 2.4.5 led to the related idea that most of a channel's geometry is determined by high discharge events that have a relatively low occurrence. The discharge related to such event is called the channel-forming discharge (Bridge, 2003). The most commonly applied discharge measurements that are taken to represent the channel-forming discharge are the effective discharge Q_{eff}, the bankfull discharge Q_{bf} or a discharge with a certain recurrence interval Q_{ri}. In some stable channels or in stable flume experiments $Q_{eff} \approx Q_{bf} \approx Q_{ri}$ (Doyle et al., 2007).

The Q_{eff} is the discharge that over time transports the largest amount of sediment. It is computed by finding the maximum of the curve that results from multiplying the flow frequency curve with a sediment discharge rating curve. Q_{bf} is defined as the maximum discharge that can be hold within the channel banks without an overspill occurring. The definition of Q_{ri} is as easy as the name suggest, it is a high discharge event that occurs at a determined interval. The recurrence period that is used is mostly in the range of 1.5 to 2 years (Copeland et al., 2005).

2.5 Bifurcations and avulsions

2.5.1 The principles of bifurcation initiation

Another important process that is involved with the evolution of meandering rivers is the occurrence of bifurcations and avulsions, i.e. resp. partial and complete diversions of the main water flow into a new course through the adjacent floodplain (Slingerland & Smith, 2004). These comprise the already mentioned meander cut-offs, but more importantly also complete changes of the river course. A selection of different flow diversion types is presented in figure 11.

The initiation of a shift in course is conceptualized and modelled by Slingerland & Smith (1998). It starts with a crevasse channel that is cut into the levee of a meandering river during high water levels (fig. 12). Because the water entering the crevasse channel is derived from relatively high in the main flow (H), it contains relatively low concentrations of suspended solids. Consequently, the crevasse flow is under its transport capacity and the entrance is eroded, deepening the entrance (h) and increasing the crevasse channel discharge (V). As the sediment load of the river water increases with depth, the crevasse channel gradually deepens until the sediment-carrying capacity is satisfied by the suspended solids entering from the main channel.

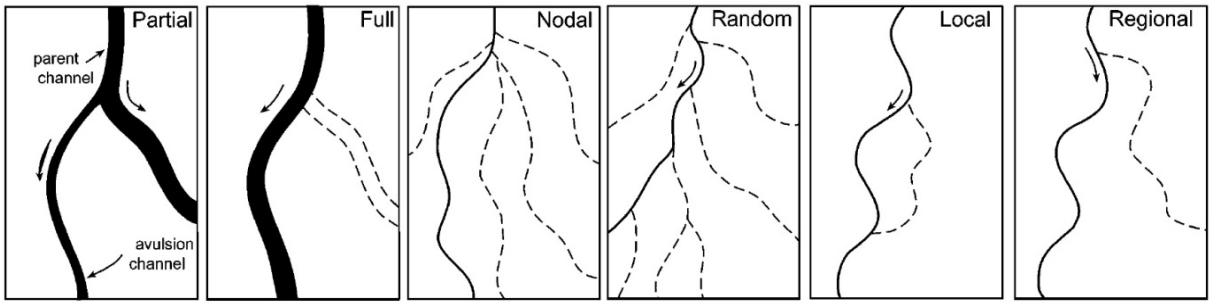

Figure 11: Different types of flow diversions (Slingerland & Smith, 2004).

2.5.2 Modelling of bifurcation asymmetry

Further evolution of the crevasse channel depends on the dynamics in the asymmetry of the water and sediment load between the main and the bifurcation channel. This determines the stability and thereby the bifurcation/avulsion duration, i.e. the time until the old channel is completely abandoned. Modelling efforts (Kleinhans et al., 2008) showed that the ratio between sediment transport and flow discharge in the two branches tends to remain relatively equal over time. When the total distribution of water and sediment between the branches becomes very asymmetrical the steady ratio is lost. At that moment the amount of

sediment transport in the former main channel relatively rapidly decreases, causing retention of the water flow of that channel. The model furthermore shows that most bifurcations, i.e. for a wide range of boundary conditions, usually result in a highly asymmetrical sediment and discharge distribution but do not tend abandon the old channel quickly, i.e. not within 200 model years. Overall the model provides an improved view on the bifurcation dynamics. It is however useful to perform an additional field test to validate the outcomes.

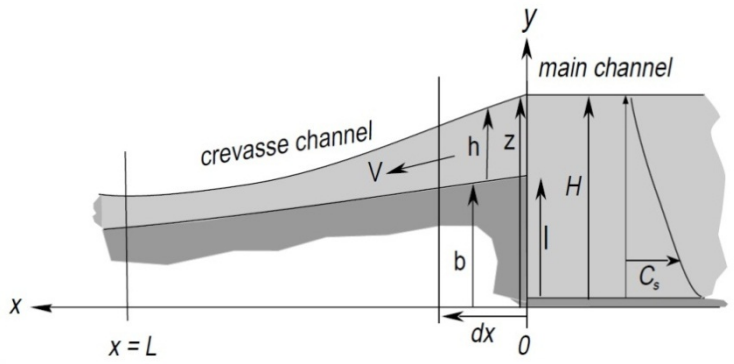

Figure 12: Side view sketch of the initiation concept of a bifurcation (Slingerland & Smith, 1998).

2.5.3 Driving forces of bifurcation dynamics

The main drivers behind the dynamics of bifurcation asymmetry can be attributed to many complex relations and on-site geomorphology, e.g. the gradient difference between the two channels, the presence of a resistant substrate, the bifurcation angle, sediment sorting, the upstream meander configuration and bar pattern (Kleinhans et al., 2008). The widely adapted view in the field of physical geography that the bifurcation asymmetry is primarily dominated by gradient advantages is therefore misleading. Research on avulsions of the Mississippi in the Late Holocene validates this as it proves that other factors can be critical for avulsion occurrence and development (Aslan et al., 2005). In their case the erodible substrate of a network of crevasse floodplain deposits led to the avulsions.

2.5.4 Time scales related to bifurcations

An indication for the time scales that are related to avulsions is presented in a study of the Rhine-Meuse delta (Stouthamer & Berendsen, 2001). The results of the study are based on 32 different avulsion sites and hundreds of core samples. Avulsion duration varied from 0 to 1250 years. A large 58% of the avulsions were classified as instantaneous. This contradicts the model findings of Kleinhans et al (2008). The instantaneous events found by this study were randomly distributed over time, which suggests that the found ratio between

instantaneous and gradual avulsion durations is natural for the long term of this particular river system and is not caused by other short-period external effects on the river dynamics. The time scales found in the study can be an indication for other lowland deltas that have similar boundary conditions as well.

2.5.5 Indication of avulsion duration

Hypothetically, an indication for the avulsion duration can be found in the distribution of the size of the oxbow lakes that belong to both channel branches that are downstream of an avulsion. The size of a meander bend has a relation with the amount of discharge. Therefore, a wide range in sizes represents a slow change, i.e. such bifurcation channels had time to generate differently sized oxbow lakes during the gradual increase/decrease in discharge. If there is a sudden avulsion more selected widths are found, indicating that only a short period of discharge increase/decrease occurred and that there was insufficient meander evolution to form differently sized oxbow lakes.

2.6 Relation between geometry and discharge

With use of datasets containing information on both the geometry and discharge of meandering rivers around the world, empirical relations between them have been determined since the early twentieth century (Leopold & Wolman, 1960). Although of empirical nature, they are supported by the complex physical relations between channel width and discharge, width-depth ratio and bar pattern, and meander bend erosion and bar pattern (Kleinhans, 2010). Many publications are available concerning these relations and therefore this section only presents a selection.

The empirical relation between meander wavelength and channel width is given by (Leopold & Wolman, 1960):

$$\lambda = \alpha W^{\beta} \tag{4}$$

where λ is the meander wavelength (m) and W is the channel width (m). Based on 50 rivers in different conditions, the dimensionless values for α and β found by Leopold & Wolman are 10.9 and 1.01 respectively. Other studies show slightly different figures (Dury, 1976; Yang, 1971), especially the value of α can differ, up to a factor of two. This is probably caused by the use of different methods as well as datasets in each study.

Empirical relations between channel width and discharge are more intensively researched and are discussed extensively in literature. The form of the general equation is (Hey & Thorne, 1986):

$$W = \alpha Q^{\beta} \tag{5}$$

where Q is the flow discharge (m^3/s). Values for α range from about 3 to 7 and for β from 0.45 to 0.11 (Carlston, 1965; Dury, 1976; Hey & Thorne, 1986; Knighton, 1974; Yang, 1971). There is however a general trend. The coarser the bed material, the lower is the value for α and the higher is the value for β. It is caused by the high bed shear stress of coarse bed rivers compared to that of sand-bed rivers. This results in a larger width increase per unit discharge (Kleinhans, 2005). Data analysis of 300 rivers confirms the presence of the relation (fig. 13), as well as the values for α and β (Kraaijenbrink, 2010). The power relations found by the trend fitting are:

$$W_{combined} = 3.09 Q^{0.58} \qquad W_{gravel\ bed} = 2.67 Q^{0.61} \qquad W_{sand\ bed} = 5.14 Q^{0.51}$$

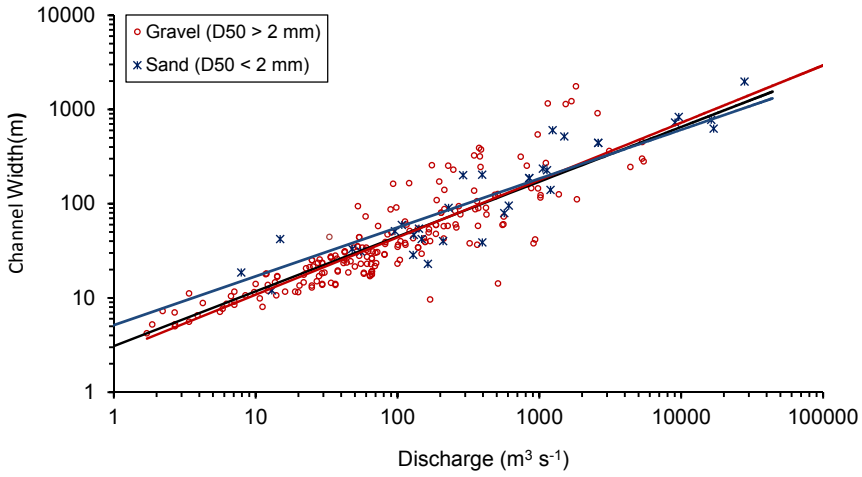

Figure 13: Relation between discharge and channel width (Kraaijenbrink, 2010).

Many suggested the use of meander wavelength for the calculation of discharge by combining equation 1 and 2 into (Bridge, 2003):

$$\lambda = \alpha Q^{\beta} \tag{6}$$

A range of different values were also found for α and β. Trends observed directly from data are e.g. α = 166 and β = 0.46 (Carlston, 1965). The trend found by Carlston explains 98 % of the variation in the data that comprised 14 large rivers in the United States. Similar analysis

in another study however shows a less significant relation (Schumm, 1967). Here only 48% of the variation is explained by the trend.

The explanation for this difference is that Carlston (1965) used data on the same river type, i.e. meandering, while Schumm (1967) mixed the data of sand-bed and gravel-bed rivers. It is unclear which precise statistical methods were used by both studies and which specific parts of the channel were sampled. Furthermore, the discharge data retrieved for the different studies were probably not based on the same type of discharge measurement. While Carlston based its trend on the mean annual flow, the discharge type used by Schumm is unknown. The values found for α and β can differ up to a factor of 10 as a result of the latter (Bridge, 2003).

A table showing a selection of values found in different studies for α and β for the described relations between meander wavelength, channel width and discharge, is shown as table 1. The best relation to use for the calculation of meander wavelength by discharge depends on the application. Though favourable is one that uses the channel-forming discharge (Copeland et al., 2005).

The related uncertainties can be significant due to the influence of many complex factors that differ per river type and can even differ per stretch of a single channel. Hence the results are definitely not precise and can therefore not be firmly trusted to be accurate. For indicative or comparing purposes however they can be very useful. Using them for relative comparison of rivers within a single study area for example, is thought to works reasonably well (Bridge, 2003). As in the research presented in this thesis the relative river dynamics within one study area are determined to yield information about the local river and bifurcation evolution, the empirical relations are useful and therefore utilized.

Equation				Author
	$w = 8.8Q^{0.5}$	$L = 3.03w$		Inglis (1949)
$L = 49.6Q^{0.5}$				Various data sets
$L = 65.9Q^{0.5}$		$L = 6.46w$		
$L = 65.2Q_b^{0.5}$		$L = 7.32w_b^{1.1}$		Leopold & Wolman (1957)
		$L = 11.03w^{1.01}$	$L = 4.5r \quad r = 2.3w$	Leopold & Wolman (1960)
$L = 166.6Q_{ma}^{0.46}$	$w = 10.99Q_{ma}^{0.46}$			Carlston (1965)
		$L = 10w^{1.03}$		Zeller (1967)
$L = 61.2Q^{0.47}$	$w = 9.81Q^{0.42}$			Ackers & Charlton (1970c)
$L = 35.6Q^{0.63}$		$L = 11w_b^{1.14}$		Ferguson (1975)
$L = 35.7Q_b^{0.55}$	$w_b = 3.08Q_b^{0.54}$	$L = 10.71w_b$		Dury (1976)
		$L = 7.5w_b^{1.12}$	$L = 4.53r \quad r = 1.5w_b^{1.12}$	Williams (1986)
$L = 72.16Q_b^{0.49}$	$w_b = 4.33Q_b^{0.49}$	$L = 14.14w_b^{0.99}$	$r = 1.92w_b^{1.05}$	Mackey (1993)

Table 1: Relations between meander wavelength, channel width and discharge. L = meander wavelength, w = channel width, r = radius of curvature, Q = discharge, b = bankfull, ma = mean annual (Bridge, 2003)

2.7 River dynamics in the Ganges Delta

To evaluate discharge values that are obtained with object-based image analysis, it is important to have knowledge about the current and past dynamics of the distributaries in the study area (fig 14). Therefore this section provides a concise overview of the recent and present dynamics of the major rivers in the study area, i.e. the Hooghly and the Gorai. To place them in a larger perspective, an overview of the general Holocene river evolution in the study area is presented first.

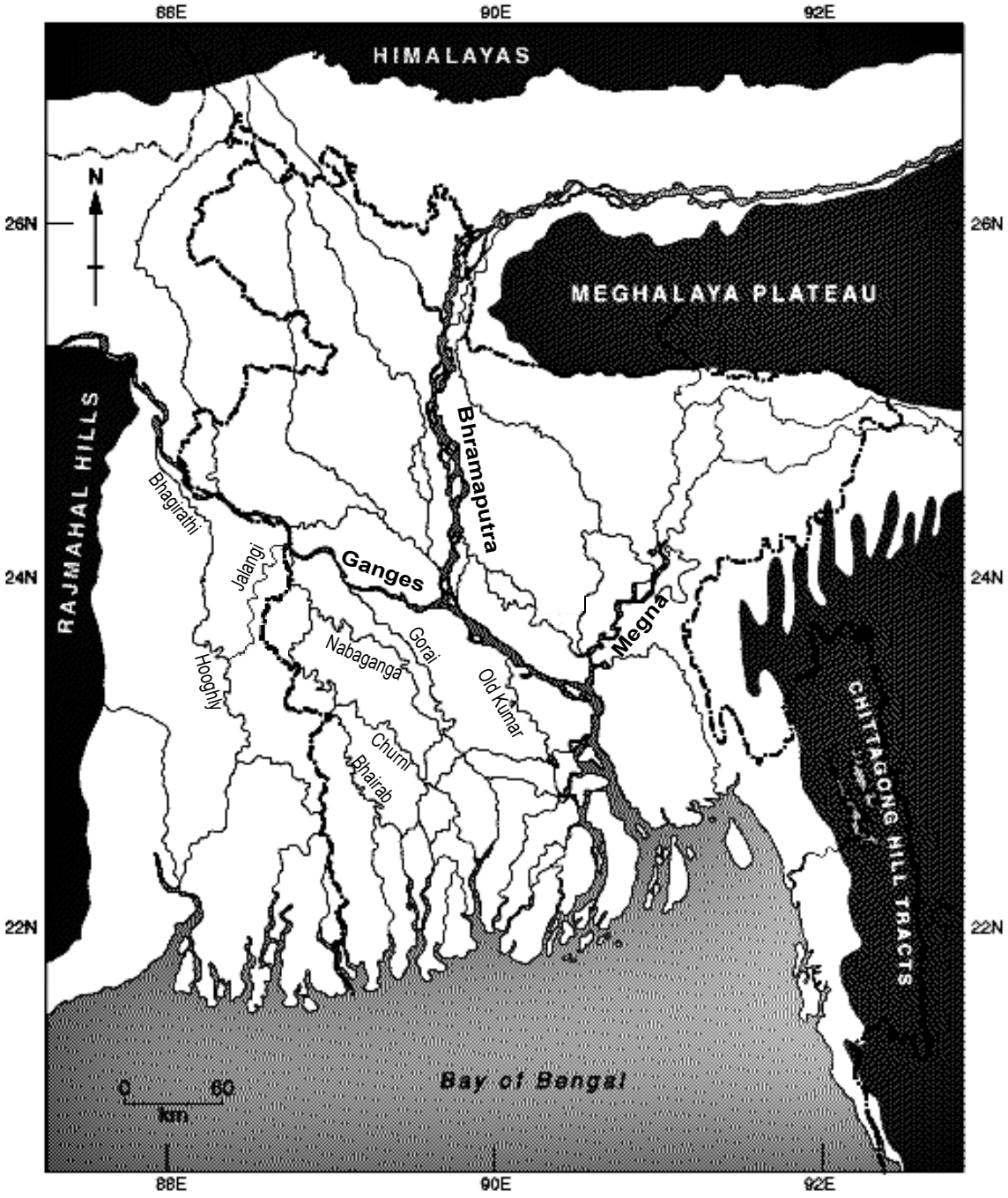

Figure 14: Map of the Bengal basin with relevant rivers labelled with their name (after Bangladesh Studies, 2006).

2.7.1 General Holocene evolution of the Ganges Delta

Supported by multiple geological and historical records, the general theory on the main course of the Ganges is that it has shifted numerous times towards the east in the Holocene (Goodbred Jr. & Kuehl, 2000). The shifting is thought to be induced by the net sea-level rise that caused aggradation of the delta plain. Such a depositional regime, especially in combination with the large discharges and extremely varying discharge peaks, provides a dynamic delta in terms of shifting channel courses (Slingerland & Smith, 2004).

Goodbred Jr. & Kuehl (2000) suggest the main course of the Ganges avulsed in multiple stages from the Hooghly-Bhaghirati channel towards its present course that flows to the east, also referred to as the Padma River. Geological evidence for this comes from coastal peats found in the so-called Thin Mud facies. The peats are present in the estuary at the major outflow of the Hooghly in the Bay of Bengal, and they indicate increased tidal processes that result from a sudden decrease in discharge.

With the bifurcation nodes located further downstream on the present eastbound course of the Ganges, more north-south oriented distributaries (fig. 14) are suggested to have been the Ganges' main course for at least some time are present: the Jalangi, the Bhairab/Mathabhanga, the Gorai, the Old Kumar and the Ariel Khan (Sarker, 2005). There are however large uncertainties about the exact evolution of the distributaries and the exact nature and evolution of the Ganges avulsions (Rudra, 2010). The uncertainties are mainly caused by the lack of undoubted evidence for many of the distributaries. An indication for the difficulties are already noticeable from a look at satellite imagery of the region, as for the Hooghly and the Bhairab/Mathabhanga rivers oxbow lakes and fossil meander bends that have Ganges dimensions are clearly noticeable (fig 15), while for the other distributaries these are practically absent.

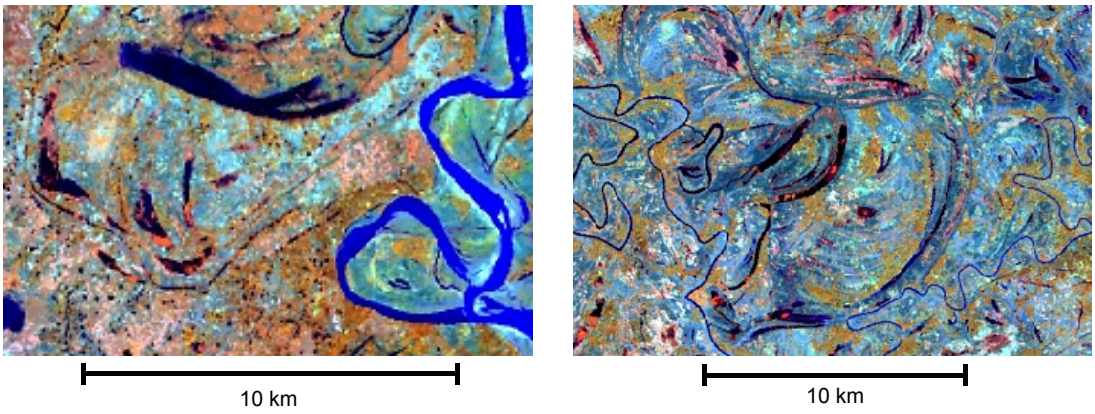

Figure 15: Subsets of Landsat image clearly showing large fossil meander bends near the Hooghly (left) and in the Bhairab (right).

A series of palaeographic maps shows the shifting of the Ganges main course (fig. 16). The figure shows that 7000 years BP the main flow was located at the present course of the Hooghly, i.e. the southward pointing arrow on the left figure. At 5000 years BP the channel shifted to about the course of the present day Gorai, the lower arrow in the middle figure. In the period in between the Jalangi, that is located in between the Hooghly and the Gorai and flows back westward into the Hooghly in the south, as well as the and Mathabhanga are considered to have shortly functioned as the main course of the Ganges (Sarker, 2005). 3000 years BP the course changes again as the Old Kumar River took over the main water flow, represented by the lower left arrow in the right image.

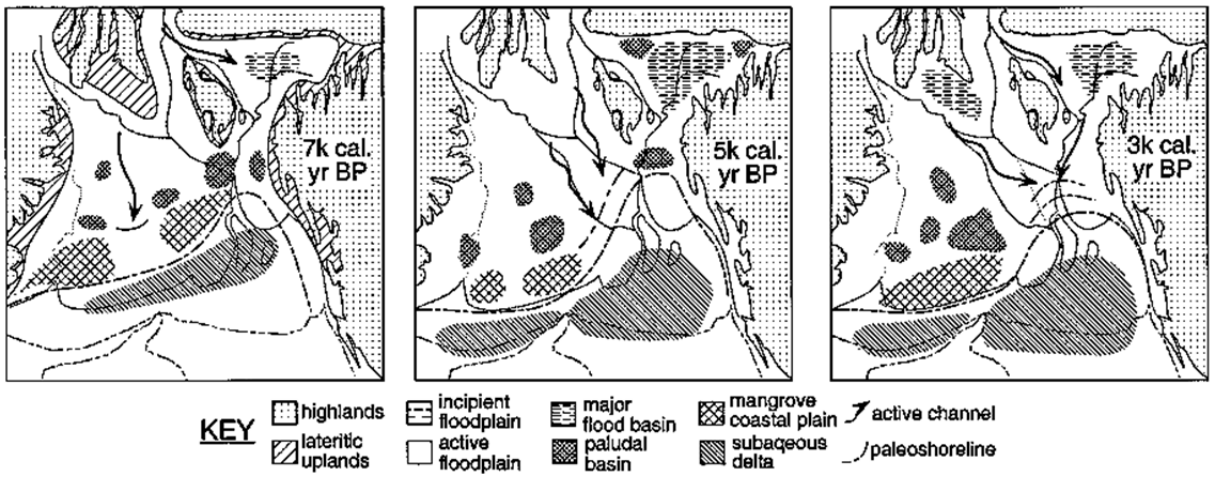

Figure 16: Selection of palaeographic maps of the Bengal basin (Goodbred Jr. & Kuehl, 2000)

2.7.2 Recent dynamics of the Ganges distributaries

In the last few centuries the Hooghly experienced a further decrease of the amount of discharge (Biswas, 2002). As this trend continued over the course of the last century and the important metropolis of Kolkata is located downstream, measures were taken. A barrage and canal were constructed near Farakka in 1975 (fig. 17) to assure a water flow of ca. 1150 m^3/s into the Bhaghirati (Sarker, 2005), i.e. the upstream section of the Hooghly. The barrage however seem to have had notable effects on the rivers that bifurcate from the Ganges downstream.

Namely, water flow stopped at some point in the dry season for many rivers in the area including the Jalangi, the Mathabhanga and the Gorai (fig. 18). The first two already showed major problems in terms of dry season discharge long before the barrage was build, but were completely shut off after the construction (Maniruzzaman, 2008). The Gorai experienced gradual discharge reductions after the construction of the barrage until in 1988 water flow

completely halted for a few months in the dry season. This situation continued until 1998. In that year a large scale dredging project started to allow perennial water flow again (de Groot & van Groen, 2001; Sarker et al., 1999). Table 2 and figure 19 both show the decline in discharge of the Gorai around the commissioning of the barrage.

Though an effect of the barrage is likely, the discharge decreases found in the Gorai could very well be caused by the natural evolution of the bifurcation into an avulsion. It is however unknown to what extent each factor has played a role (Sarker, 2005).

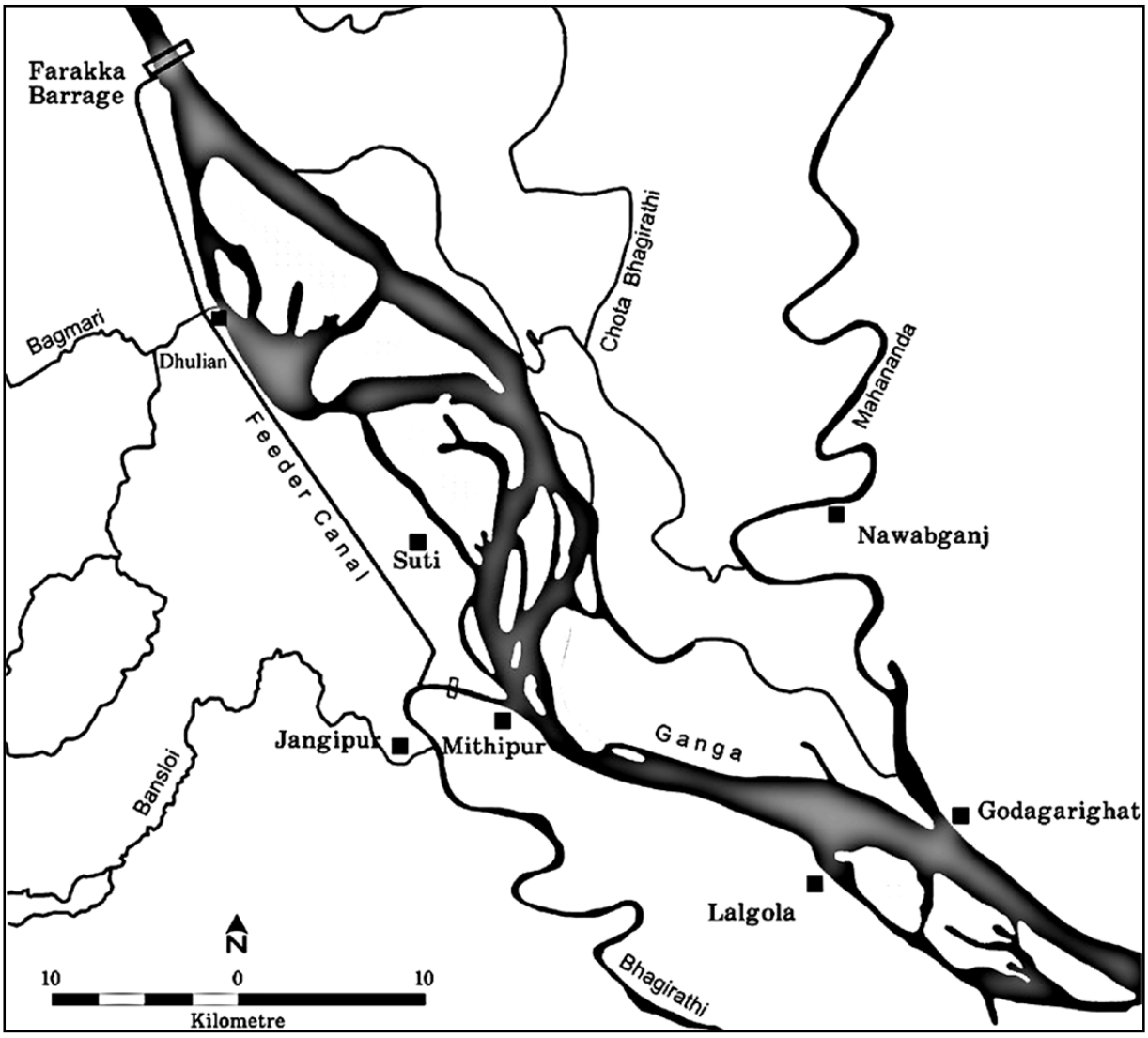

Figure 17: The course of the Ganga between Farakka and Lalgola in 1982. Note the position of Farakka barrage, the feeder canal and the highly angled off-take of the Bhaghirati near Mithipur (Rudra, 2010).

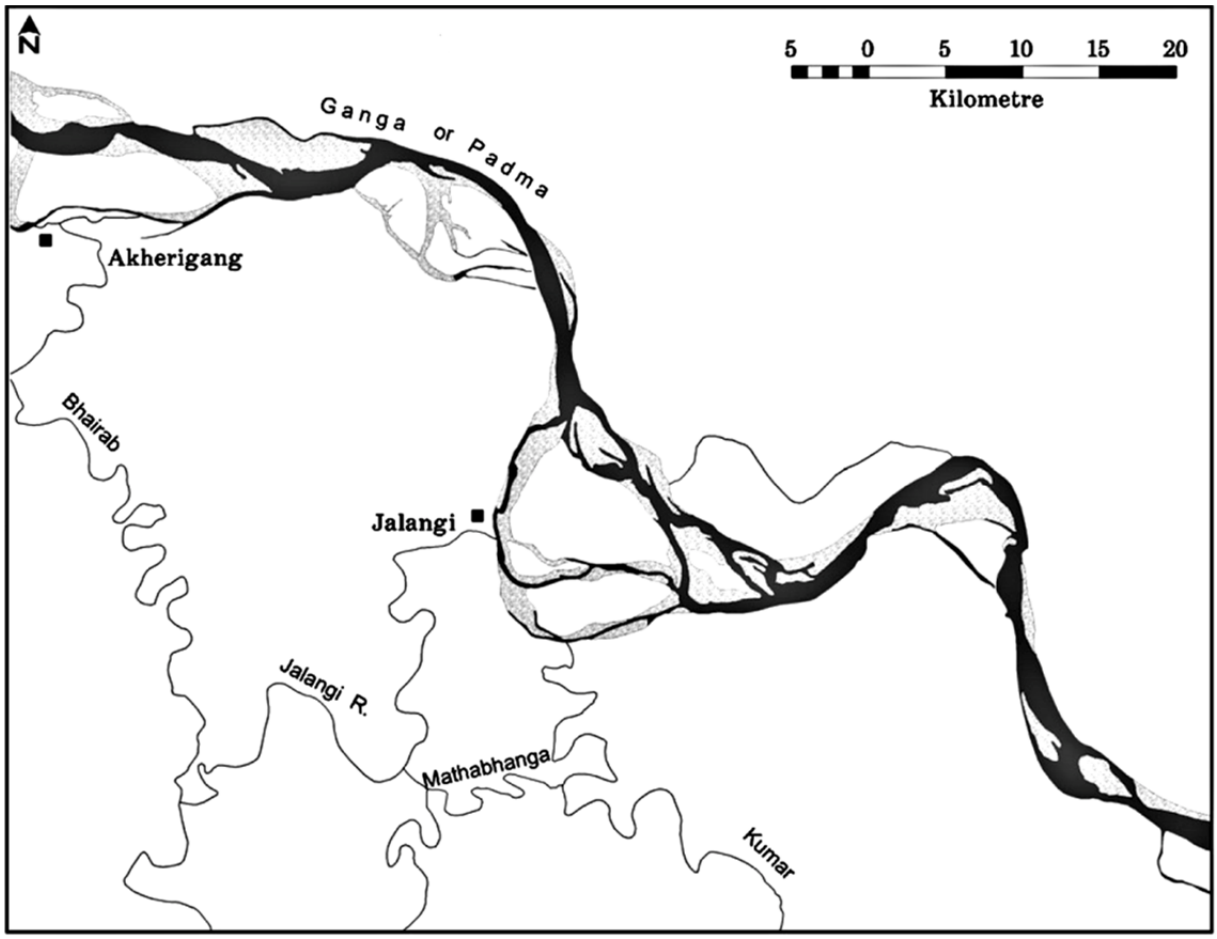

Figure 18: The course of the Ganga between Akherigang and Jalangi. Note the relatively highly angles off-takes of the Jalangi and Mathabhanga, as well as the Gorai's in the far bottom right corner (Rudra, 2010).

	Nov.	Dec.	Jan.	Feb.	Mar.	Apr.	May.
1965-1974 (Pre-Farakka)	913	490	314	232	170	149	215
1975-1988 (Post-Farakka)	683 (-25)	293 (-40)	143 (-54)	100 (-57)	69 (-59)	72 (-52)	141 (-34)
1988-1996 (Post-Farakka)	261 (-71)	68 (-86)	11 (-96)	0 (-100)	0 (-100)	0 (-100)	18 (-90)
1997-1998 (Year with lowest discharge)	245 (-73)	272 (-44)	57 (-82)	0 (-100)	0 (-100)	0 (-100)	-

Table 2: Dry season monthly mean flows (m^3/s) of the Gorai River at different periods. The numbers between the brackets are the differences in percentages with the Pre-Farakka period (Maniruzzaman, 2008).

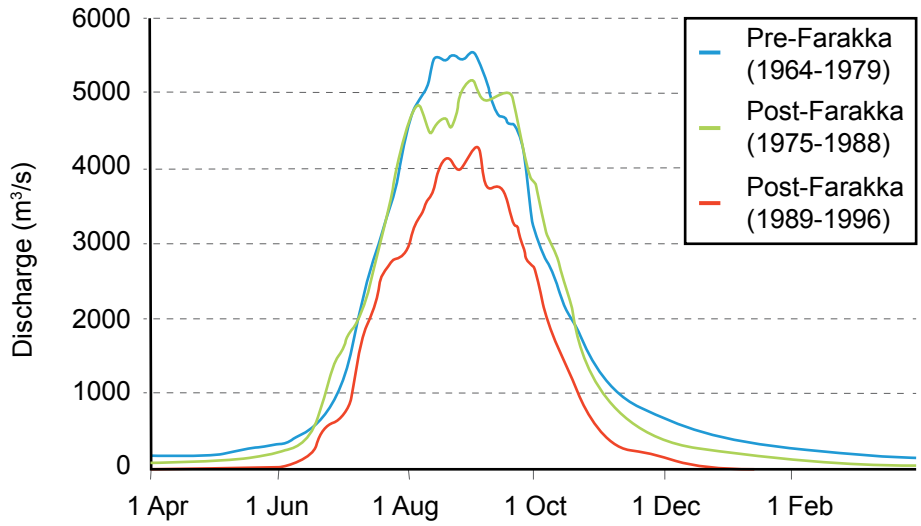

Figure 19: Mean daily discharges of the Gorai River for different periods (Sarker, 2005)

2.7.3 Effects of the off-take planform on bifurcation evolution

The fact that the Hooghly-Bhaghirati, Jalangi and Mathabhanga all showed a significant decrease in discharge in the Pre-Farakka period implies that, although the barrage definitely had its impacts on downstream rivers, another process must be occurring as well. It is hypothesized that this is part of the natural progress of the local bifurcations. Rudra (2010) states that the Ganges' extremely high monsoon discharges, i.e. up to ca. 70000 m^3/s, can easily erode the middle bank at a bifurcation. This is not only due to the vast amounts of shear stress exerted by the water, but also due to the high erodibility of the banks that completely dry out in-between the monsoons. The process causes a downstream migration of the distributary off-takes along the course of the Ganges, as the inner bank simultaneously encounters the normal slow flow conditions and related loss in transport capacity and sedimentation. The relatively large bifurcation angles found for the distributaries (fig. 17 & 18) and the fact that Rudra (2010) found that the Hooghly-Bhaghirati off-take was considerably less angled about 150 years ago support this hypothesis.

The change of the bifurcation angle over time could be an explanation for the decreases in discharge found for the Bengal delta distributaries. As the angle increases there is less forcing of water into the distributary and more of bed material. The succession of discharge decreases, i.e. Hooghly-Jalangi-Mathabhanga-Gorai-Old Kumar, supports this explanation. This because it is the same as the succession of channel abandonment by the main flow (Goodbred Jr. & Kuehl, 2000; Rudra, 2010), that coincides with the start of the increase in bifurcation angle and thus the start of the decrease in discharge.

For the Gorai, a somewhat similar cause is suggested by Sarker (2005). This is however not based on the migration of the off-take but on the change in morphology of the Ganges bend at the off-take. It however involves changes in the bifurcation angle as well. He states that the off-take position was favourable for water flow in 1973, because it was located in the outer bend of the Ganges (fig. 20). Then in 1992 a very unfavourable situation established due to the bend erosion that had occurred. The off-take was no longer located in the outer bend and the resulting loss in transport capacity within the off-take caused severe sedimentation to occur. Landsat TM images from 2000 and 2010 (fig. 21) show the unfavourable position of the off-take continued although the planform configuration appeared to have become slightly better in 2010 (Kraaijenbrink, 2010).

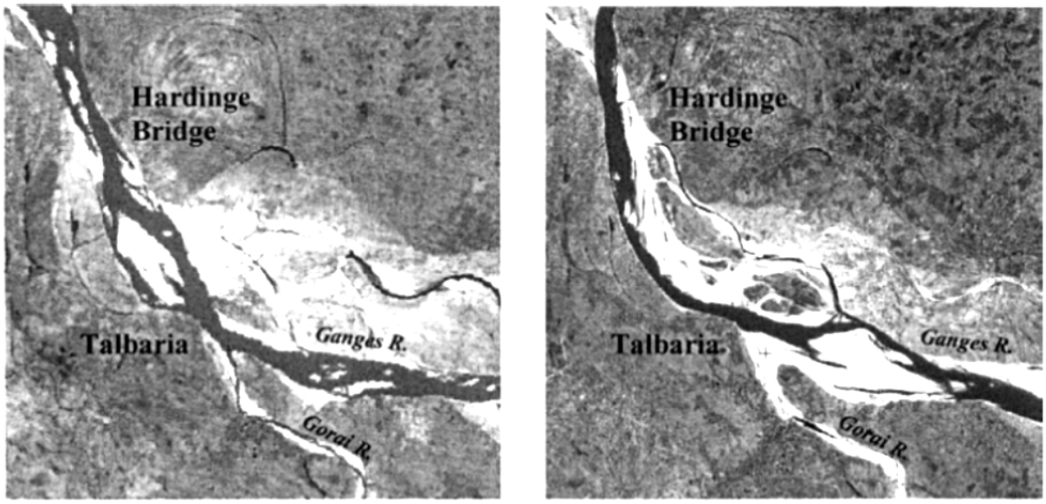

Figure 20: Different morphologies of the Ganges bend at the Gorai off-take. Left = 1973, right = 1992 (Sarker, 2005).

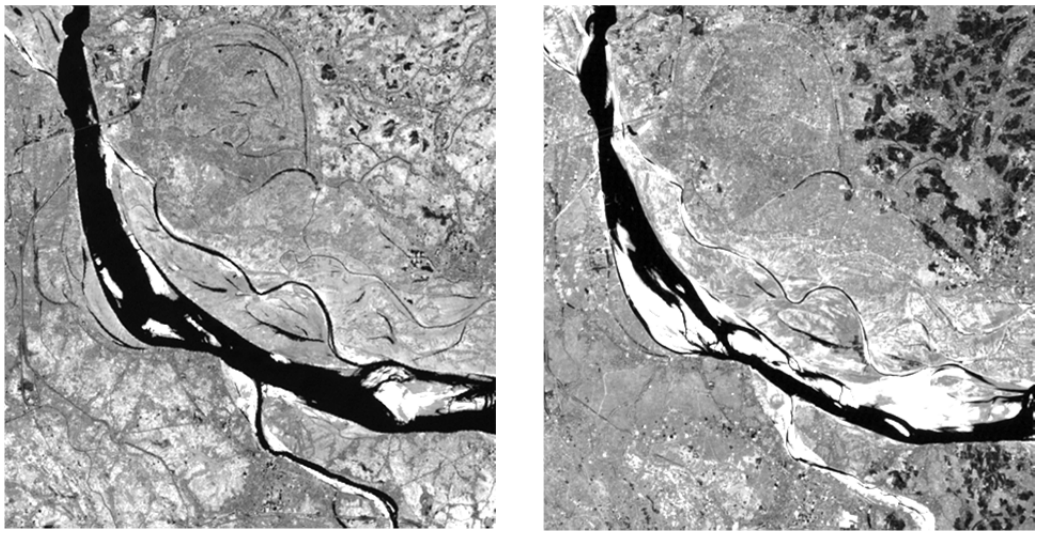

Figure 21: Near-infrared Landsat TM images of the Gorai off-take. Left = November 2000, right = February 2010 (Kraaijenbrink, 2010).

2.8 Main image analysis techniques

2.8.1 Principles of pixel-based image classification

For a long time, pixel-based classification procedures were the main image processing means (Blaschke, 2010). The two traditional methods that are used are the supervised and unsupervised classification. For both methods features are delineated by assigning pixels to a pixel cluster, or class. This is done by means of statistical analysis of the image's pixel-values of the different bands. This can be performed using different statistical algorithms, e.g. minimum distance to cluster mean, maximum likelihood or Euclidean distance (Lillesand et al., 2003). The algorithms compare the unclassified pixel to pixel clusters within the feature space, i.e. an n-dimensional plot of the pixel values for the different bands.

The difference between supervised and unsupervised classification is that supervised classification requires the input of predefined pixel clusters by the user. This is done by providing training sets of pixels that represent the classes that are to be delineated (Lillesand et al., 2003). The unknown pixels are then assigned to the predefined clusters by the chosen algorithm. In unsupervised classification the clusters are not predefined. The user only defines the algorithm used and the number of clusters that is desired. The algorithm then automatically defines clusters that are statistically the most distinct.

2.8.2 Development of object-based image analysis

In 1998 German researchers at Definiens AG in Munich presented the Cognition Network Technology. The technology made the already existing object-based image analysis technique widely available to scientist via their developed eCognition software (Definiens AG, 2008). The semantic analysis of hierarchical groups of pixels it performs, is a major improvement to pixel-based analysis as attributes that hold information on object shape can be analysed.

The objects are created by a segmentation of the image that is based on spectral characteristics of the image and the shape characteristics of the objects that are to be defined (Definiens AG, 2007). The objects are presented as polygons, each consisting of multiple pixels (fig. 22). They hold all kinds of object attributes that are based on spectral, shape, or relational characteristics. This new way of image analysis has a much wider applicability as opposed to pixel-level analysis, because besides spectral information there are also shape, relational and neighbourhood related attributes present that can be used for the development of classifying rules (van der Werff & van der Meer, 2008).

Figure 22: Example of a segmentation of with the objects being outlined in black. Note that the grassland is represented by larger objects than the trees as its pixels are more homogeneous (Baatz & Schäpe, 2000).

2.8.3 Parameters used in multiresolution segmentation

The image segmentation is the most important process in object-based image analysis. The so-called multiresolution segmentation algorithm available within the eCognition software creates the most useful objects for classification and analysis that is based on the object metrics (Benz et al., 2004). This segmentation algorithm has three input parameters to define: the scale parameter, the shape criterion and the compactness criterion (Definiens AG, 2007).

The scale parameter sets the maximal internal heterogeneity of the created objects and shows a positive relation to the resulting object sizes, though the resulting sizes are data driven (Addink et al., 2007) as they depend on the image homogeneity (fig. 22). A higher setting of the scale parameter results in larger objects. There is a tool developed that is able to determine the optimal scale parameter to classify the image in a certain amount of distinct classes (Drăguţ et al., 2010), however most geo-related image analysis is aimed at specific subjects or goals prohibiting the use of this generalized approach. The exact optimal values for the scale parameter therefore usually have to be estimated by means of trial and error.

The shape criterion ranges from 0 to 0.9 and it represents how much the segmentation results will be based on shape or spectral properties. A higher value means more influence of shape and less of spectral characteristics. Both properties are important when it comes to creating useful objects, as the shape of image entities is always defined by the spectral properties. For this reason the shape properties cannot be set to be of higher influence than 90%.

The shape properties used in the segmentation are controlled by the compactness criterion that defines whether the shape of an object should be dominated by compactness or smoothness. Compactness is used when the image entities are rather compact, but are separated from non-compact objects only by a relatively weak spectral contrast. Smoothness should be used when working on relatively heterogeneous data to inhibit the objects from having frayed borders, while maintaining the ability to produce non-compact objects (Definiens AG, 2007). Both the shape and compactness criteria are application specific and therefore have to be estimated by reasoning and by trial and error.

2.9 Methods to delineate meanders

1.1.1 Pixel-based river classification

A pixel-based classification of a satellite image aimed at delineating meandering channel pixels is only partly possible, as there are clear limitations to this method. A simple unsupervised classification is usually sufficient, although other techniques can be used (Mertes, 2002). From the resulting classes a selection is made of those that represent water bodies, which are then separated. There will practically always be a class with pixels representing the water bodies, because water is a distinct feature in the feature space. This is caused by the significant difference between the spectral signature of open water and the rest of the landscape. The main discriminator is the very low reflectance of infrared wavelengths by water (Lillesand et al., 2003). The image that is used for the classification thus must at least contain data on infrared wavelengths for a correct classification.

As a pixel-based classification can in principle only delineate water pixels, actual meanders will never be classified. Their shape is the main characteristic of meanders and this is not accounted for in the pixel analysis. As meanders are usually not the only water features on a satellite image, there is often abundant pollution of non-channel water pixels. This is hard to remove due to the great similarities of the spectral signatures between these different open water types (van der Werff & van der Meer, 2008).

1.1.2 Object-based river classification

The delineation of meandering channels with use of object-based image classification was recently assessed (Addink et al., 2007; Addink & Kleinhans, 2008; van der Werff & van der Meer, 2008). The idea behind it is that because meanders have distinct elongated planform characteristics, a method that uses shape characteristics should be able to delineate them. As expected both studies show that the use of the object-based method allows to delineate meanders and that it additionally yields improvements over a pixel-based

classification. Namely, the pollution by other open water bodies is not present and fossil channels can be delineated as well (Addink & Kleinhans, 2008), i.e. if they are still apparent by elongated geomorphology. Furthermore, it does not require the subjectivity of a human to determine if the classified pixels, held within the objects, are channels, as it would with pixel based analysis.

For the meander delineation, Landsat 5 TM image bands are pre-processed with a radiometric normalization, to a common mean and standard deviation of resp. 120 and 20, to give them equal weight during the segmentation (Addink & Kleinhans, 2008). Band 6 is removed because its high temporal variability and coarser resolution would hamper the segmentation. As van der Werff & van der Meer (2008) use a combined spatial-spectral classification, they rescale the 8-bit (0-255 digital numbers) to floating values in the range of 0-1 digital numbers. This to obtain equal ranges and weighting for the shape measure values and the spectral values.

The multiresolution segmentation algorithm is applied multiple times with different settings of the scale parameter (Addink & Kleinhans, 2008). This because meanders of different sizes often show different internal spectral variation on Landsat images. The scale parameters used in this case were 5, 7, 10, 15 and 20. The higher scale parameters used do cause pollution of the channel objects with elongated riparian features, e.g. forests or urban areas.

Classification of the objects yielded by the segmentations is done by applying a threshold condition on the object shape features. To determine the optimal attribute(s) to use for meander delineation, Addink & Kleinhans (2008) have performed a classification tree analysis on multiple shape related object features. The result of their analysis is that the so-called shape index is the best object feature to distinguish meander objects. All other shape features are found to be less distinctive. Besides, using an additional shape feature is found to not improve accuracy significantly. The shape index (fig. 23) is defined as (Definiens AG, 2007):

$$s = \frac{e}{4\sqrt{A}} \tag{7}$$

where e = the object border length and A = the object surface area.

Examples of values for the shape index for different standard shapes are: circle = 0.88; square = 1.00; rectangle (4x1) = 1.25; rectangle (50x1) = 3.61. The minimum shape index possible is that of the circle. There is no maximum shape index value, as the longer the object the higher the shape index value will be. Typical threshold values found for delineating

meanders in Landsat imagery range from 2.5 to 3.2. All objects above the threshold were classified as meanders (Kraaijenbrink, 2010).

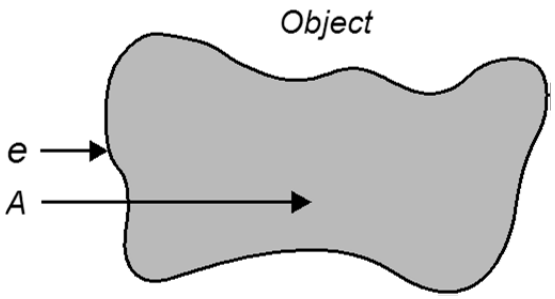

Figure 23: Schematic representation of parameters used to calculate shape index (Definiens AG, 2008).

2.10 Conducted river geometry analysis

Following from the object-based meander classification method and the empirical relations between meander geometry and discharge, Addink & Kleinhans (2008) suggested the use of the shape information held by the delineated meander objects to calculate the channel discharges. The suggestion is assessed in previous work (Kraaijenbrink, 2010). Although the methods that were applied did not all yielded realistic discharge values, the results provided new insights in the complications that are involved. The methods and results of this study are presented in this section.

2.10.1 Methodology

The area of interest for the study by Kraaijenbrink (2010) was a part of the Ganges-Brahmaputra Delta, located in Bangladesh. It focused on the Gorai, one of the north-south distributaries of the Ganges. A subset of a Landsat 5 TM scene from the year 2000 was used that encompasses an area of about 4000 km^2 (fig 24). The area consists of a floodplain with many active and fossil channels surrounded by agricultural, forests and urban areas. The image was classified according to the method of Addink & Kleinhans (2008). A scale parameter value of 200 was used additionally to properly delineate the Gorai itself. The results of the classifications are shown in figure 26, 27 and 28.

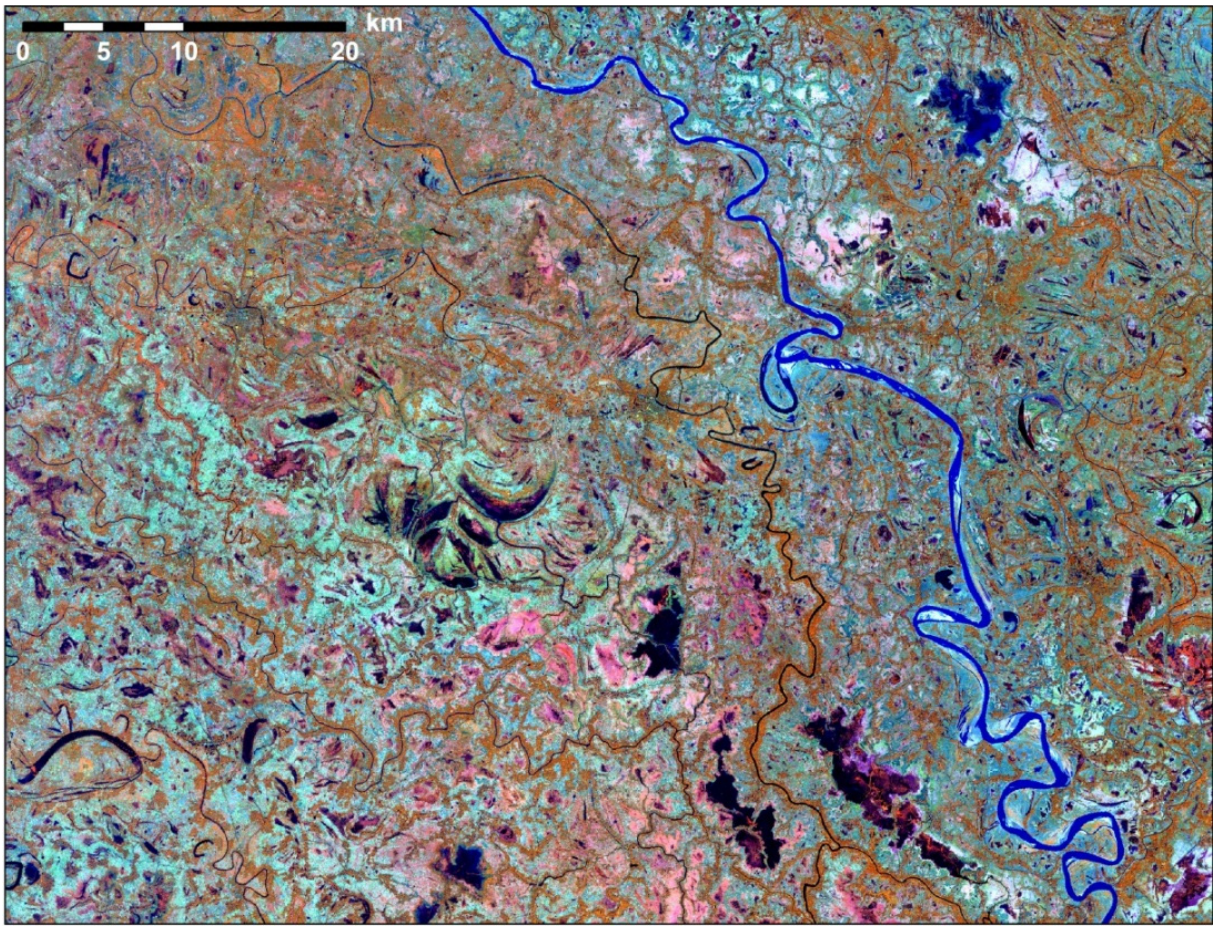

Figure 24: Landsat TM image of the study area, RGB=453 (Kraaijenbrink, 2010).

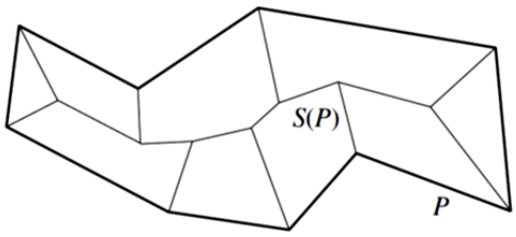

Figure 25: Example of a skeleton with *P* = polygon and *S(P)* = skeleton (Vyatkina, 2008)

For the calculation of discharge various shape related object features, as available in the eCognition software, were used. The features that were used are related to the skeletons of the polygonal objects: *the curvature/length ratio*, *the skeleton width* and *the skeleton length.* The skeletons (fig. 25) consist of straight line segments that are pieces of angular bisectors of the polygon edges that together describe polygon geometry (Aichholzer et al., 1995).

All angles present in the polygon are split in two parts with equal degrees by vertices that are connected by the centerline. The skeleton is created using a so-called linear wavefront. The wavefront moves along the polygon edges at equal speed, so it remains parallel to the polygon. Meanwhile it determines its current width and thereby the location of the centerline, while keeping track of the movement of the vertices (Vyatkina, 2008).

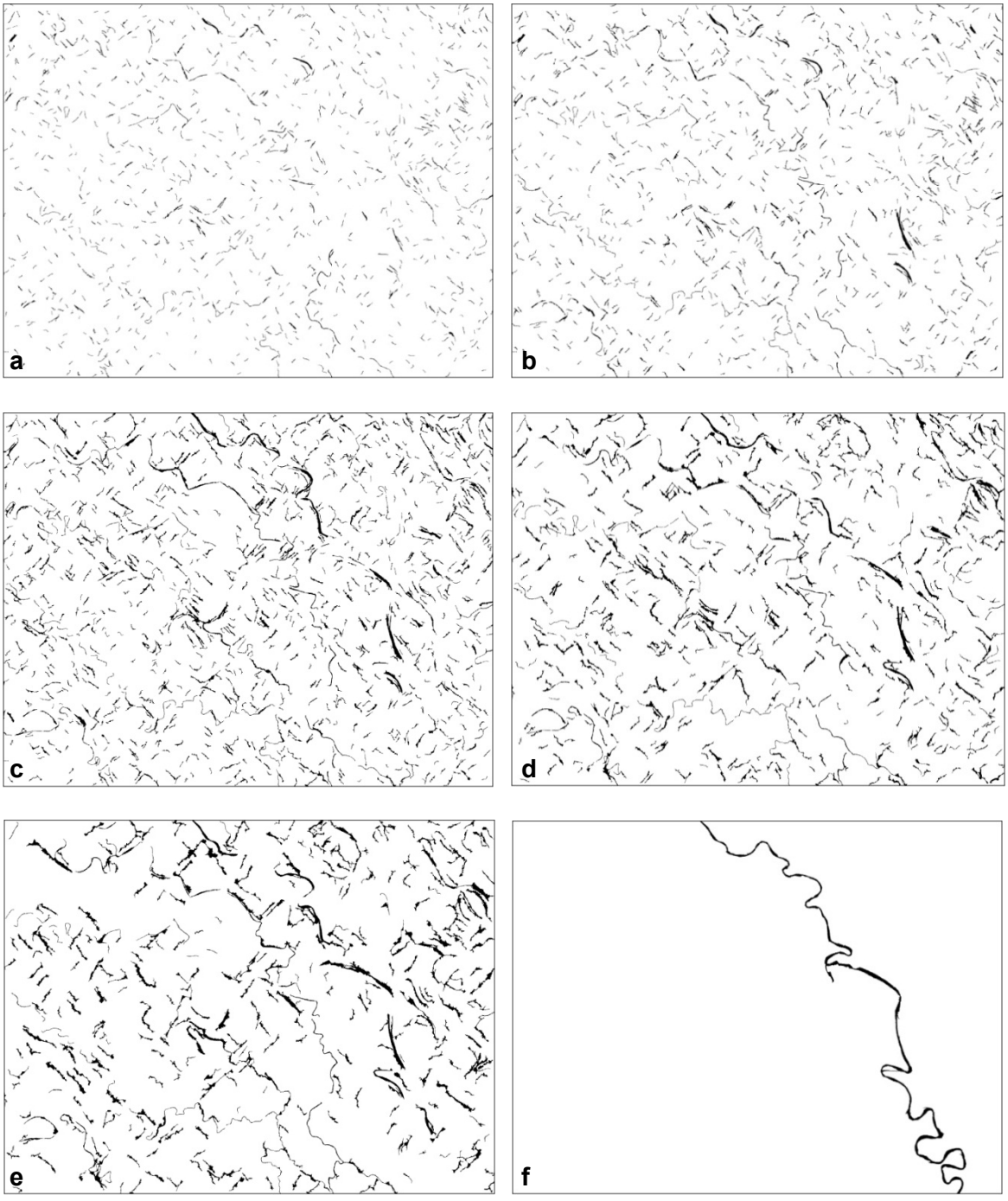

Figure 26: Object-based classifications for the different heterogeneity levels, a-f show the results of scale parameter 5, 7, 10, 15, 20 and 200 respectively (Kraaijenbrink, 2010).

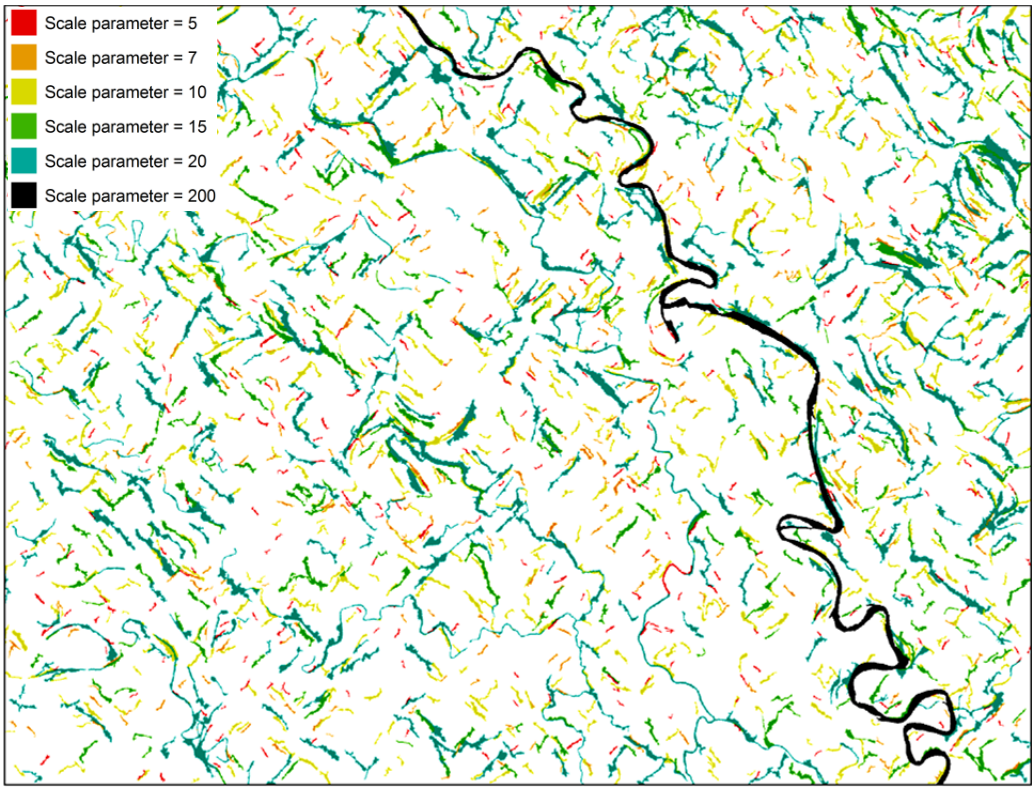

Figure 27: Classifications combined with larger scale parameters projected on top of smaller scale parameters (Kraaijenbrink, 2010).

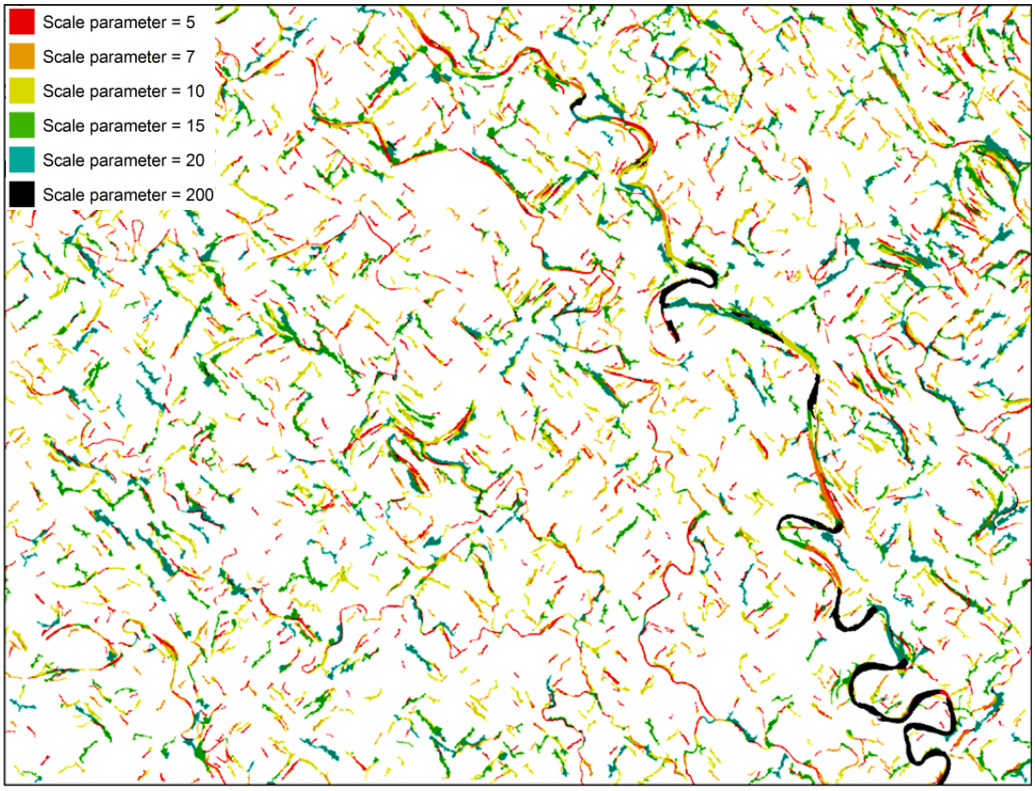

Figure 28: Classifications combined with smaller scale parameters projected on top of larger scale parameters (Kraaijenbrink, 2010).

Within eCognition, the length of a skeleton is defined as the added distances of the skeleton's main line sub-sections (Definiens AG, 2008). The curvature is described as being the cumulative absolute changes in direction along the main line (fig. 29.a). All the direction changes are added by cumulatively iterating from each end point towards the most central sub-section. The skeleton-based width is defined as the average width of the triangles the main line crosses (fig. 29.b).

Two extent related features are used in the approach as well, i.e. the object *main direction* and *the bounding box length* and *width*. The main direction is equal to the direction of the largest eigenvector derived from the covariance matrix of the spatial pixel distribution of an object (fig. 30a). The bounding box length and width are calculated from the length to width ratio and the number of pixels of an object (fig. 30b).

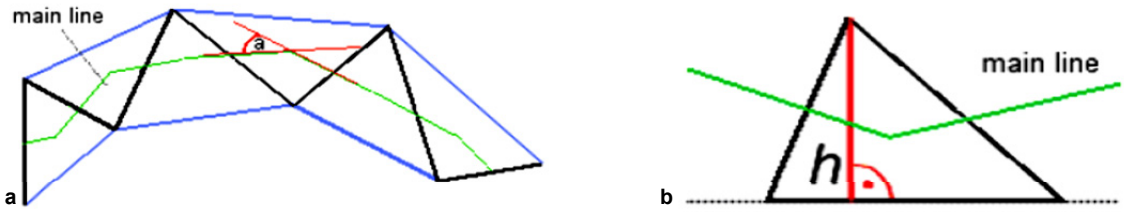

Figure 29: Definition of skeleton length (a, green line), example of one of the direction changes used to calculate the curvature (a, angle α) and the width of single triangle the main line crosses (b, red line) (Definiens AG, 2007)

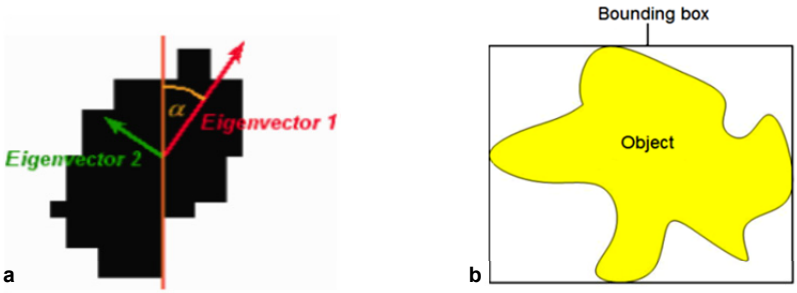

Figure 30: Definitions of the main direction (a) and the bounding box (b) that are used in the discharge calculations (Definiens AG, 2007).

Three different methods were assessed to calculate discharge from the object metrics (Kraaijenbrink, 2010). The first one comprised a calculation of the discharge with object curvatures. This was done by assuming that the average meander object resembled a sine shape meander that has a cumulative direction change of 180 degrees per one complete meander wave. Backtracking the skeleton main line length related to that amount of direction

change was done using both *curvature/length ratio* and *skeleton length*. The wavelength was calculated by multiplying this length with the ratio between the length of a sine and the related x-axis. The wavelength was then used in equation 6 to obtain discharges, using α = 100 and β = 0.5.

The second method consisted of trigonometric transformations of the main direction and the bounding box length to obtain a so-called smallest enclosing rectangle (fig. 31). Combining the length of this rectangle with *skeleton length* yielded an approximation of the sinuosity. The sinuosity was suggested to be converted subsequently into wavelengths by a calculation involving the width of the rectangle, i.e. an approximation the meander channel belt width as well as the meander amplitude. The last performed method used the *skeleton widths* to directly calculate discharge using equation 5.

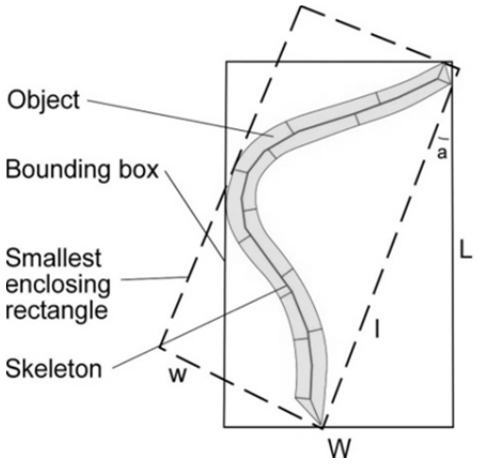

Figure 31: Sketch of the geometric variables used in the sinuosity calculation process (Kraaijenbrink, 2010).

2.10.2 Results

The calculation of meander wavelength and related discharge through the sine transformation of the curvature/length ratio resulted to be incorrect because the resulting wavelengths were unrealistically short. The discharge calculation therefore resulted in unrealistic low values, i.e. 95% of the values were below 1 m^3/s, compared to values found in literature.

The method that calculated sinuosity did not result in correct results either. Values for the main line length were often smaller than that of the rectangle length. This resulted in many sinuosities below 1. This is theoretically impossible as the curving channel path can never be shorter than the shortest downvalley path. The single object representing the Gorai did show a realistic sinuosity of 1.55, although this is significantly larger than the value found in literature for this particular stretch of the river, namely 1.39 (Sarker, 2005).

The range of discharges that resulted from inserting the skeleton width in equation 5 are more realistic (fig. 32), namely in the range of 35 to 5000 m3/s. As can be noted in the figure the mean widths shift towards higher values when the scale parameter increases. Furthermore, the distributions show an increase of variance. The distributions are skewed as well, i.e. they have a larger right hand tail, although they become more normal when the scale parameter increases.

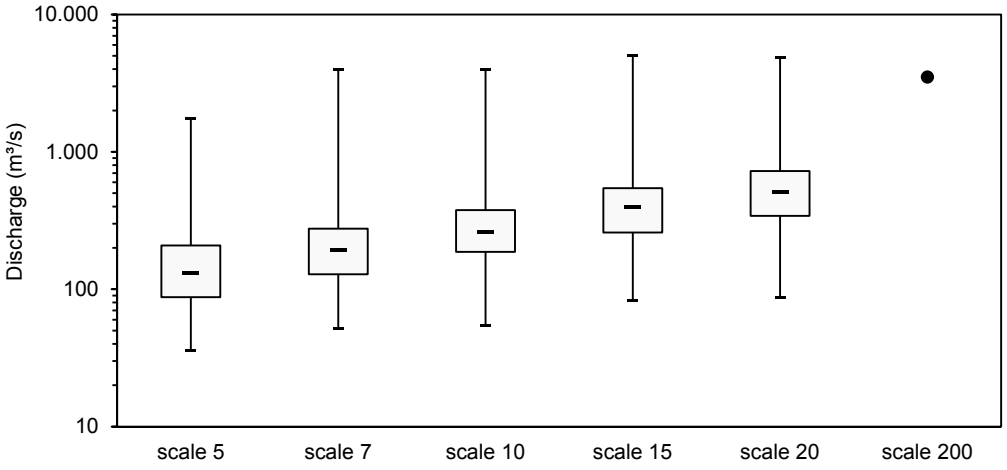

Figure 32: Box plots of the discharges resulting from the skeleton widths for every heterogeneity level (Kraaijenbrink, 2010)

2.10.3 Insights in complications

It was expected the results of the discharge calculations with skeleton curvature were not correct, as many ill-founded assumptions were made in this method. The extreme differences between the calculated and measured discharges were however unexpected. It is thought that they were mainly due to the many small direction changes of the skeleton main line that are not related to changes in channel direction (fig. 33). Concluding, the curvature as defined within eCognition is not usable for the determination of meander wavelength. Other curvature concepts were hypothesized to be able to improve the results, such as the one of Camporeale et al. (2005) and Chen & Duan (2006) presented in § 2.3.2.

The problem with a method that calculates sinuosity using trigonometric transformations is thought to be caused by the definition of the skeleton main line length. Namely the main line does not represent the whole object length as the end of the skeleton generally consists of skeleton branches (fig. 25). With small objects the part of the skeleton length that is described by the end-branches is significant, resulting in skeleton lengths that are shorter than the calculated rectangle lengths. The objects sets contained many relatively short objects, hence most of the sinuosities are below 1.

Another complication is that the calculation of the meander wavelength from the sinuosity and meander amplitude is not very straightforward (Langbein & Leopold, 1966). This is due to the differences in angle between upward and downward parts of the meander that result in different channel lengths while the wavelength and sinuosity are remain constant (fig. 34).

Though the discharge calculations through skeleton width showed more realistic values, there are some major complications with this method as well. First of all, the abundant pollution of non-channel pixels causes a great overestimation of the discharge values, especially for the objects that resulted from the higher scale parameters. Secondly, the skewness of the distributions of lower scale parameters is caused by the hard lower limit of the image resolution, resulting in incorrect width and discharge distributions.

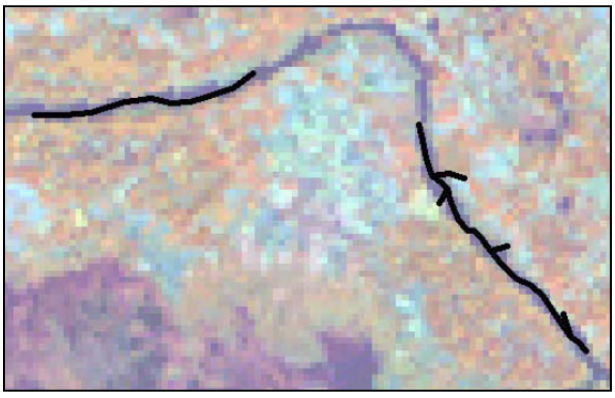

Figure 33: Example of non-channel related skeleton direction changes (black lines), i.e. the skeleton has abundant curvature that is not present in the channel itself (Kraaijenbrink, 2010).

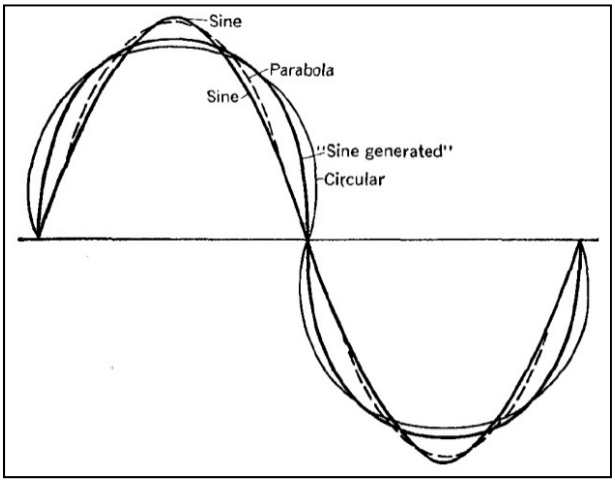

Figure 34: Examples of differences in channel length with constant meander wavelength and sinuosity (Langbein & Leopold, 1966).

A problem related to all of the methods in this study is that to obtain a good coverage of classified meander objects, multiple scale parameters have to be used. This results in different sets of meander objects that held similar as well as complementary information, i.e. they partly describe the same meanders (fig. 27 & 28). As is known from basic statistics theory, meaningful analysis of data can only be performed when the dataset does not contain any form of duplicates (Davis, 2002). A hypothesized solution is that the complementary objects from the different scale parameters are algorithmically merged to form one object set (Kraaijenbrink, 2010).

Another overall problem in classification was that not all meander objects were recognized or recognized correctly. This led to gaps in the meander object network. It is hypothesized that the gaps may be removed by defining a classification rule based on the spectral and shape characteristics of neighbouring objects or by the direction (or direction trend) of the ends of a neighbours skeleton main line. An algorithm combining the bordering meander objects can then generate objects representing complete, individual channels. As those objects have a much more defined geometry they are thought to be more analysable (Kraaijenbrink, 2010).

2.11 Conclusions

2.11.1 Knowledge about river dynamics and evolution

In the last decades a vast amount of research dedicated to all sorts of processes related to the dynamics of rivers has been conducted. Still, knowledge about the exact physical mechanisms driving these processes is limited. The theory behind river dynamics is still largely of a conceptual nature.

The last decade however has brought an improved understanding of the physical processed due to a large amount of conducted research. The empirical approaches are however not to be abandoned yet, as empirical knowledge provides an important framework for the development of an even more improved understanding.

2.11.2 Definitions of meander geometry

There are three relevant empirical relations known in literature. The values used for the dimensionless parameters used within these equations can vary greatly. The latter is caused by the dependency of the parameters on many factors, which are predominantly unknown or just poorly provided by the researchers. It is therefore difficult to pick the best set of parameters for a specific application. The main issue lies with fact that many studies use

different statistics or measurement techniques prohibiting a proper comparison. It is therefore important to apply good and clear statistics to river data.

The basis for physical and empirical meander research lies in the parameterization of the river planform. Many different parameterization methods have been used to date, depending on the specific application. In new scientific approaches a standard parameterization concept is often insufficient and a new or a revised parameterization is needed and developed.

2.11.3 Evolution of bifurcations and avulsions

One of the river processes that is still not entirely clear in terms of exact physics is the mechanism of bifurcations and avulsions. To be able to improve the understanding of this mechanism, knowledge about discharge regimes and their temporal characteristics is important, as they are closely related to the process. Major changes in discharge regime namely cause disturbances in the channel's quasi-equilibrium state which may lead to bifurcations. Conversely, bifurcations due to for example a failure of a natural levee will lead to major changes in discharge in the old channel.

Studying the discharge dynamics of river systems that are known for their abundant bifurcations is useful, especially if extensive datasets are available. The latter is however rarely the case as discharge gauges are generally not implemented in a manner that provides sufficient data for this purpose.

2.11.4 River evolution and dynamics in the Ganges Delta

The general Holocene evolution of the Ganges Delta as well as it recent river dynamics is known. The Ganges bifurcated numerous times to the east leaving distributaries in its old course. Usage of this knowledge to improve the understanding about river evolution processes is limited, as it applies to a very different process scale. Nevertheless, it does provide an indication for the natural evolution characteristics of the river system. In combination with more recent work it also gives rise to theories about the bifurcation dynamics in the area and its influence on the local river network evolution. The understanding of the exact processes involved with the bifurcation evolution is however still unaided by this present knowledge.

2.11.5 Complications of current river delineation and analysis

The delineation of rivers in satellite imagery with pixel-based image analysis is possible. There are however serious limitations inherent to this method. It only can distinguish water

carrying channels and the results can be heavily polluted by non-river water bodies. The more recently developed object-based image analysis technique is a great improvement in this field, as it has the capability to include shape properties during the classification. It can be used to delineate rivers relatively well, as they have a very distinct shape. The classified shapes can be extensively analysed due to availability of many shape related object attributes.

The possibility of analysing meander shape attributes using object-based image analysis leads to the suggestion of a method that uses this principle in combination with the known empirical relations between meander geometry and discharge. The method is suggested to be able to obtain data about the spatial and temporal distribution of discharges in a river system.

An assessment of the suggested discharge calculations shows that there were numerous complications in the implementation. A major difficulty was to obtain a delineation of all the differently sized meanders and different processing scales had to be applied to the image. This yielded multiple object sets that led to erroneous results due to oversampling of channel parts.

Another issue was the fact that many small objects together represented a larger part of a channel. These individual objects were too small to give sufficient geometry information. It is hypothesized that significant improvement of the results is gained when these two major difficulties are overcome by merging the different processing scales and the small objects.

Due to the erroneous results, the study by Kraaijenbrink (2010) did not provide further data about the spatial and temporal distribution of discharges in the river system. Therefore the need to improve the analysis results to obtain significant and correct discharge data is evident.

3. METHODOLOGY

3.1 Study area

3.1.1 Location of the study area

The area that has the focus of this study consists of a part of the Ganges-Brahmaputra Delta. The delta is primarily located in Bangladesh though the western part extends into India for about 100 km. The specific subsection of the delta that is of interest lies on the border of Bangladesh and India. It includes a part of Bangladesh in the east and a part of the Indian region West Bengal in the west (fig. 35). The main meandering distributaries of the Ganges that flow through the area are, from west to east, the Hooghly-Bhagirathi, the Jalangi, the Bhairab/Mathabhanga and the Gorai-Madhumati (appendix A1).

The area of interest is roughly bounded by the Hooghly River in the west and the Gorai River in the east. They are both thought to have been the main channel of the Ganges for some time in the past and are therefore meaningful to be considered if to gain knowledge about changes in river dynamics with discharge data. The east-west oriented area they enclose, has an extent of about 145 kilometres. In terms of north-south extent, the presence of the current main channel of the Ganges in the north and the tidal influences that are present in the southern seaward part of the delta have to be taken in to account. Both are to be left out to reduce complications inherent to respectively large scale differences and changes in river system dynamics that are not of interest in this study. A Landsat 5 TM satellite image of the study area is shown as figure 36, a larger image is included as appendix A2.

3.1.2 Geographic characteristics of the study area

The local geography comprises floodplains crosscut by many active and fossil meanders. Topographically, the study area is dominated by agricultural land and fisheries. There are however many concentrated urban areas in the region as well, as its population density is among the densest on earth. The urban areas are mainly located next to the rivers, as water ways are an important part of the local infrastructure due to the lack of a developed road network in this relatively underdeveloped region. The presence of the dense population and the extensive use of waterways must be kept in mind, as it is probable that it resulted in anthropogenic alterations of the channel morphology that may hamper the channel analysis in this study.

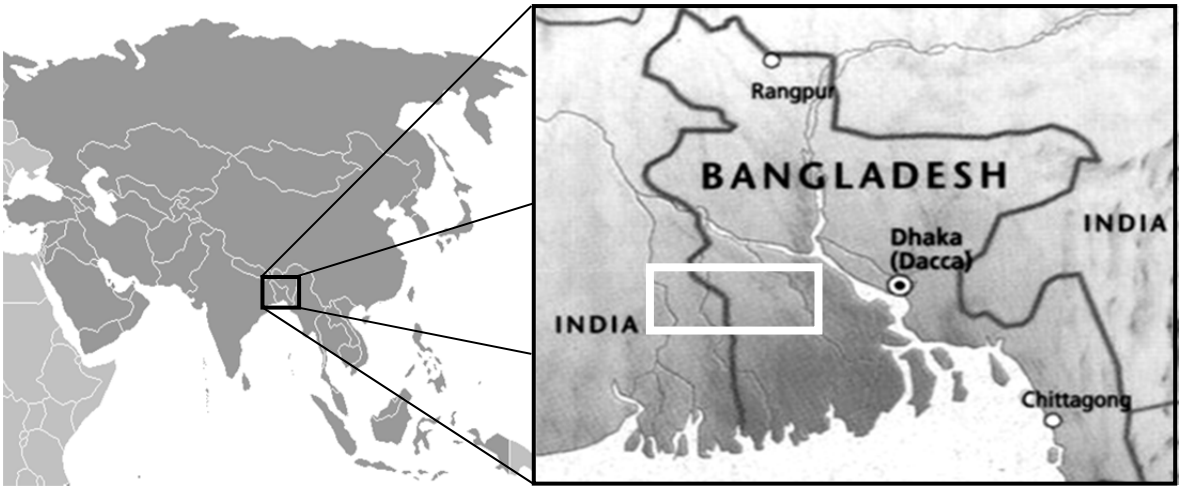

Figure 35: Location of the study area outlined in white.

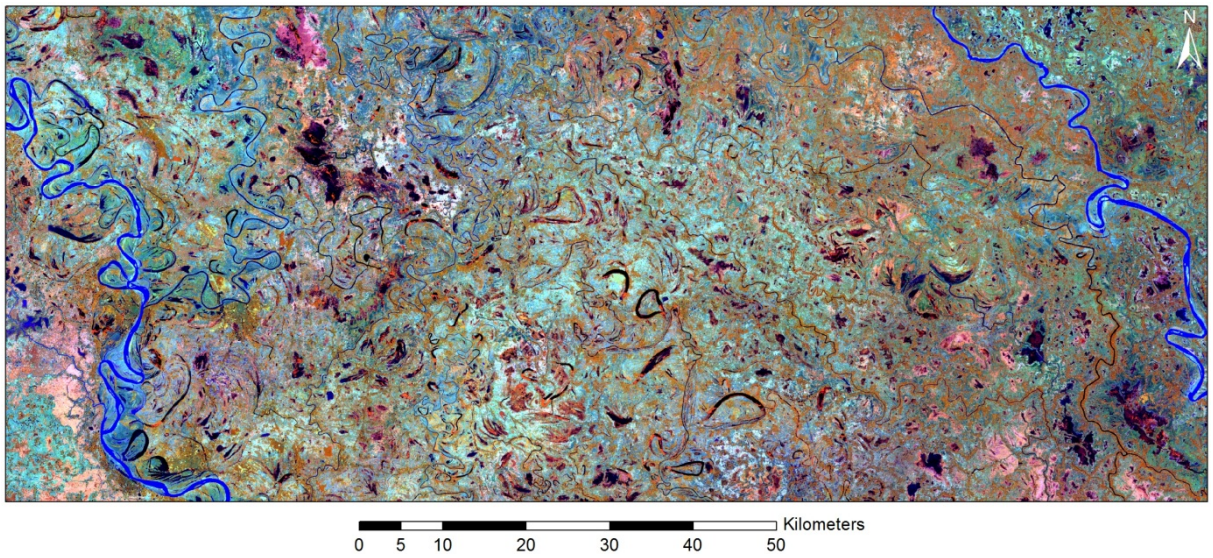

Figure 36: Landsat 5 TM image of the study area, RGB = 453.

3.2 Data

3.2.1 Data type used in the study

The method to obtain discharge values from the geometry of meander objects on satellite imagery is applied to data that originates from the Thematic Mapper sensor aboard the Landsat 5 satellite. The images from the satellite consist of seven image bands holding 8-bit data with a pixel size of 30 meters. An exception to this is the thermal infrared band 6 which has a pixel size of 60 m. The sensed spectral wavelengths of the bands of the Thematic Mapper range from visual to short wave infrared (fig. 37). The data is obtained from the data distribution website Glovis (USGS, 2012) of the United States Geological Survey (USGS). The path and row of the Landsat scene that includes the study area are respectively 138 and 44.

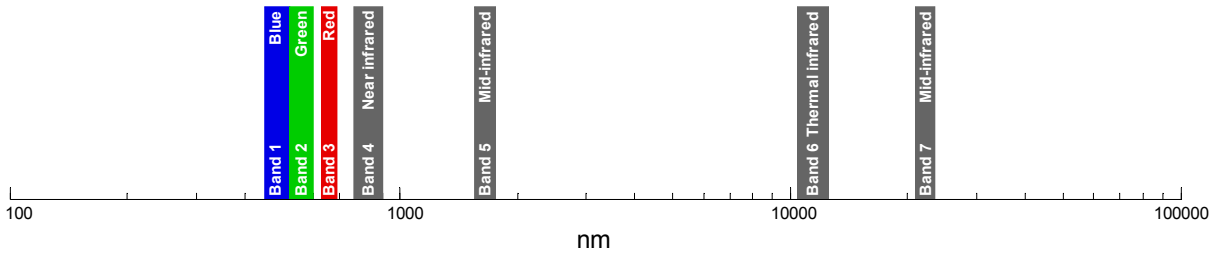

Figure 37: Spectral distribution of the Landsat 5 TM bands (according to Lillesand et al., 2003).

3.2.2 Choice for the Landsat 5 TM scene

The best channel detection results are obtained if an image is acquired during a relatively dry period. The reason for this is that at such a period the right amount of discharge is present in the rivers and the image is more likely to be clear of clouds. The amount of discharge present in the rivers is important as satellite images taken at relatively low discharge moments are superior for channel detection (Addink & Kleinhans, 2008).

The higher water levels at high discharge cause river banks to be wetter and channels to appear wider. In addition, the general wetness of the area is higher and thus the contrast between the rivers and the surroundings is less distinct, particularly in the infrared part of the spectrum. Choosing a period with very low discharge is however not favourable as well, as channel width may reduce to sub pixel size or water flow may even have seized in certain channels.

The ideal amount of discharge in rivers of the study area is reached at the transition of the wet and dry season in November. As a cloud free image is important as well, all scenes that were acquired in November are downloaded from the Landsat Legacy Collection of the USGS, as this collection consists of high quality, cloud free data only. Only two available images, dating from 1990 and 2000, fulfilled the criteria completely. From these two the scene dating November 14th 1990 is chosen arbitrarily.

3.3 Data pre-processing

3.3.1 Clipping of the Landsat scene

Before further image and river analysis can be performed the Landsat data is pre-processed. First the entire scene is clipped to the extent of the chosen study area. The definite north-south extent of the clipped image is forced to be a bit smaller than the ideal extent of study area. This is caused by limitations imposed by the available amount of random access memory in the computer during the image segmentation. The final clipped image has an extent of 5060 by 2085 pixels, which is ca. 145 by 60 km (fig. 36).

3.3.2 Determination of the at-sensor radiance

As multi-temporal analysis was intended in this study, ground reflectance data is estimated from the 8-bit digital number (DN) data of the obtained Landsat scene (fig. 38). For this the DN are converted into at-sensor radiance first (fig. 39) using the standard linear relation (Lillesand et al., 2003), given by

$$DN = G \cdot L + B \tag{8}$$

where *DN* is the digital number, *G* is the channel gain, *L* is the at-sensor radiance and *B* is the offset. The gain and offset are recorded by the sensor's internal calibrator and were obtained from the database of the USGS.

Band 6 has a coarser resolution and greater temporal variability that would both negatively influence the segmentation (Addink & Kleinhans, 2008) . This because the smaller meanders are not significantly recognized with its 60 m resolution and overall blur has a negatively influence on the usability of the other bands. It is therefore left out of all processing stages in this study.

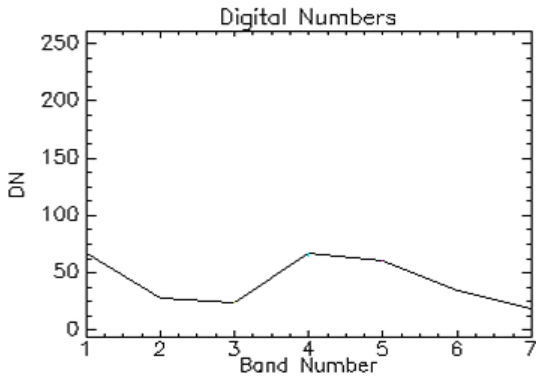

Figure 38: Example plot of a pixel's digital numbers per image band.

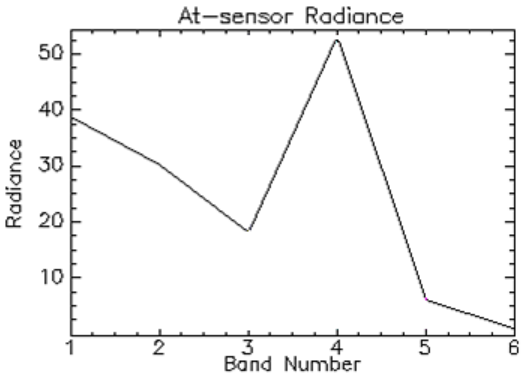

Figure 39: Example plot of the at-sensor radiance of the pixel. Band 6 represents band 7 of figure 38.

3.3.3 Estimation of the ground reflectance

To estimate the ground reflectance (fig. 41) of the Landsat image an Internal Average Radiometric Reflectance (IARR) operation is performed on the six remaining bands of the at-sensor radiance image. To reduce the required computer power in further processing the resulting floating point data are multiplied by 1000 and stored as 16-bits unsigned integers. This generates small differences in relative pixel values with respect to the original data, but these are so small that they do not significantly influence the image segmentation.

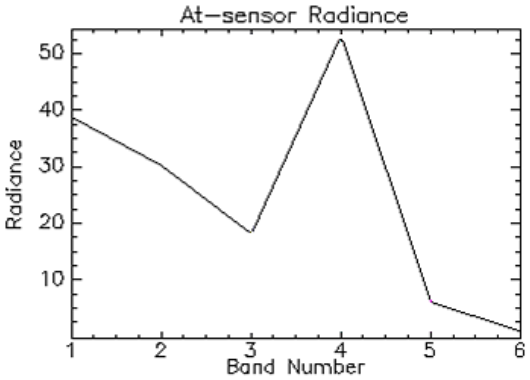

Figure 40: Example of the at-sensor radiance (equal to figure 39).

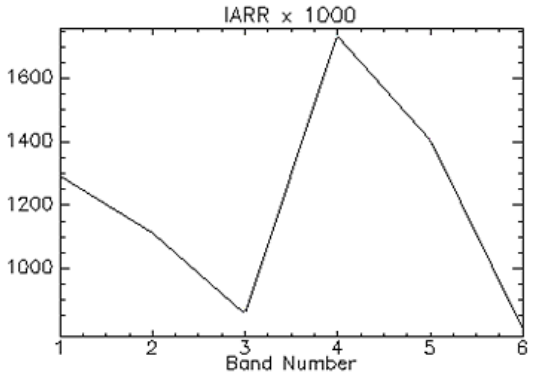

Figure 41: Example of the estimated ground reflectance of the pixel.

3.3.4 Normalization of the image bands

The resulting ground reflectance data of the different spectral bands have a wide range of means and standard deviations. This is a problem for further analysis because the bands will have a different weight in the image segmentation process (van der Werff & van der Meer, 2008). To resolve this problem a relative radiometric normalization is performed. Equal band distributions are obtained with a mean-standard deviation normalization (Yuan & Elvidge, 1996), which has the form:

$$u_k = \frac{S_{yk}}{S_{xk}} x_k + \left(\overline{y}_k - \frac{S_{yk}}{S_{xk}} \overline{x}_k \right) \quad (9)$$

where u_k = normalized digital value of band k, x_k = digital value of band k, S_{y_k} = target standard deviation, S_{x_k} = standard deviation of band k, $\overline{y}_k$ = target mean and $\overline{x}_k$ = mean of band k. The equation is translated into a static computer model and the image is processed by executing the model with a target mean of 120 and a standard deviation of 20. After the normalization process the pre-processing of the Landsat image is completed and it is ready for the object-based image analysis (fig. 36).

4. DEVELOPED METHODOLOGY

4.1 Schematic overview of developed methods

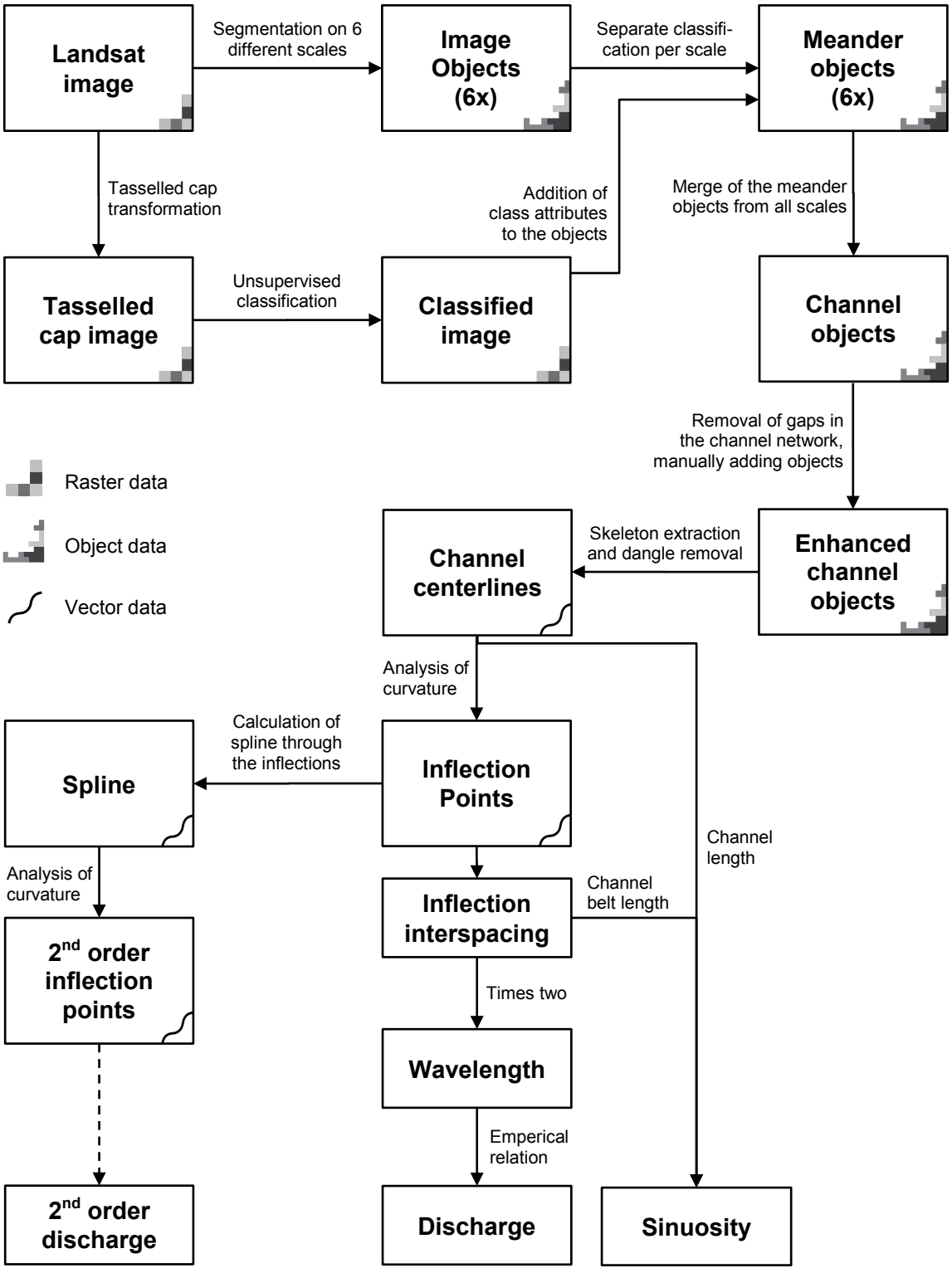

Figure 42: Flowchart of the developed object-based channel extraction and river analysis methods.

4.2 Obtainment of meander objects

4.2.1 Segmentation of the image

The image classification, i.e. the delineation of the meander objects, is performed according to the assessed object-based approach (Addink & Kleinhans, 2008). For this task the object-oriented image analysis software suite eCognition Developer 8 (Trimble, 2009) is used. To create the classifiable objects the Landsat image is segmented first. In order to identify the differently scaled channels in the image seven separate segmentations are performed using different scale parameter values: 5, 7, 10, 15, 20 and 100. The specific values are based on the values that are used in comparable research (Addink & Kleinhans, 2008; Kraaijenbrink, 2010). Other input parameters of the segmentation are the shape and compactness criteria. The shape criterion is set to 0.5, as both shape and spectral characteristics are important for the delineation of meanders. The compactness is set to 0, as meanders have an elongated shape and are not at all compact features in the landscape.

4.2.2 Classification of the objects

For the classification of the objects threshold values are first determined for the shape index attribute. This is performed separately for every segmentation level by applying statistical classifications trees on a training set of 30 manually selected meander and 30 randomly selected non-meander objects (fig. 43). In prior research abundant pollution by non-meander objects appeared in the classification stage (Kraaijenbrink, 2010). To reduce this pollution a stricter selection procedure is applied for the meander training objects, i.e. only objects that are clearly elongated are selected.

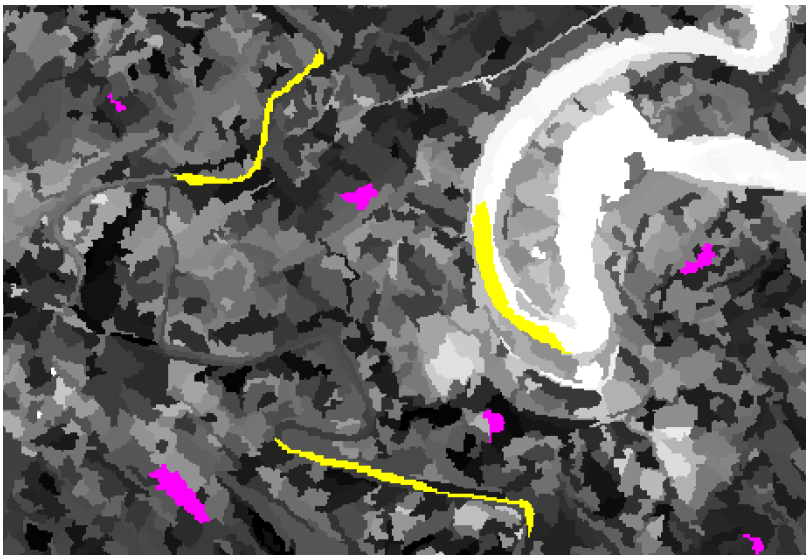

Figure 43: An example of a training set that contains meander (yellow) and non meander (magenta) objects.

The determined threshold values are applied separately to all objects of every segmentation level by using logical operators to discriminate between objects that are above and below the defined thresholds. Objects that have a shape index value that is larger than or equal to the threshold are classified as meanders, the remainder as non-meander.

4.2.3 Determination of basic object contents

To gain insight in the pixel-wise land cover of the classified meander objects the Landsat image is first processed using a tasselled cap transformation. This transformation converts the data present in the image bands into composite values, representing wetness, greenness and brightness, by means of linear relations weighted sums (Crist & Cicone, 1984). Subsequently the tasselled cap transformed image is classified using an unsupervised k-means classification process. The classification is performed with three desired clusters to obtain the classes water, vegetation and (semi-) bare.

To obtain the internal class distribution of the meander objects, the objects of all segmentation levels are used in six separate vector driven segmentations of the k-means classified image. This procedure results in six object sets that are identical to the input objects, except that they contain the pixel information of the classified image instead of the Landsat image. To delineate the meander objects from the non-meander objects in these new object sets the previously determined shape index thresholds are used.

The three classes of the k-means classified image are represented by three bands with mutually exclusive boolean data, i.e. if a pixel value is 1 for one band it must be 0 for the others. This causes the mean band value of an object to be the fraction of pixels of the corresponding class within the object. Thus, combining the mean band values of the three bands yields the fractional distribution of water, vegetation and (semi-) bare within an object.

4.3 Obtainment of a single object set

As the different segmentation levels have partly similar data on certain channel parts, they cannot be used to make a proper determination of the river dynamics in the study area due to statistical oversampling. Furthermore, many gaps are present in the channel network of each segmentation level (Kraaijenbrink, 2010). Together however, they have a comprehensive coverage of the channel network and it is therefore evident that the levels and objects need to be combined into a single dataset. An important detail of this action is that is leads to both an improvement of the data as well as a great data reduction which makes further processing better manageable.

To combine the meander objects of all the segmentation levels the different object sets are merged into one dataset by calculating their geometric union. Subsequently, to obtain objects that represent larger parts of the channels, all objects that overlap or border each other are merged into single objects.

The meander objects have lost their geometric attributes as their geometry was altered in the merge. To recompute the geometric information a new vector driven segmentation is performed, similar as in § 4.2.3. However, as non-meander objects are required in the channel network enhancing later on as well, the merged meander objects are first placed in a grid of non-meander objects from scale 7, i.e. the outline of the merged meander objects is cut out of the object set of segmentation level 7 after which both are merged.

4.4 Removal of gaps in the channel network

At his moment the delineated channel network is clearly shaping up with the presence of large objects that represent most of the channels in the area. However, multiple types of errors still exist in the network that cause channel discontinuity as well as other errors that hamper a proper river dynamics analysis of the channel centerlines (fig. 44):

1. Diagonally bordering pixels
2. Small gaps
3. Large gaps
4. Missing channels
5. Erroneous connections
6. Islands

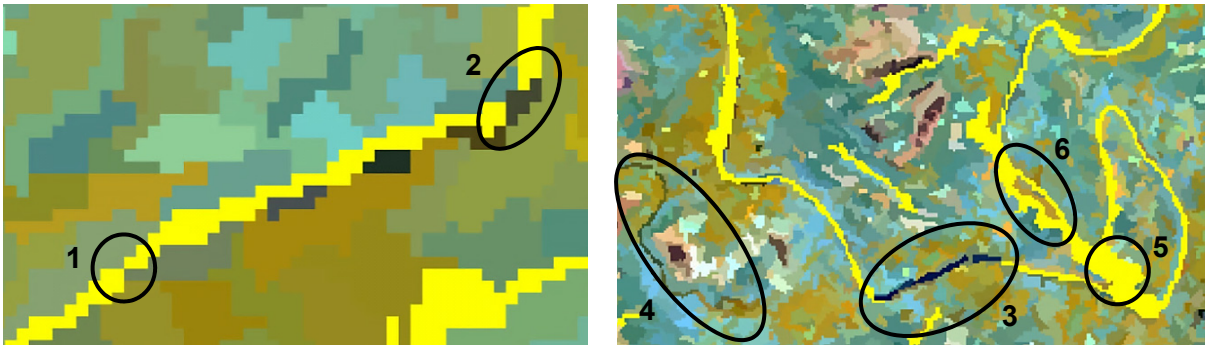

Figure 44: Examples of the errors still present in the channel network. Meander objects are shown in bright yellow. The numbering of the error types is the same as in the above presented list.

4.4.1 Connection of diagonal pixels and closure of small gaps

To solve the object discontinuity at the diagonal pixel borders, a border growth process is applied that grows the meander objects by one pixel in all directions. The newly bordering objects are subsequently merged to finalize the channel continuity. A positive side effect of this process is that gaps in the channel network that are smaller than or equal to 2 pixels are removed as well, such as error number 2 in figure 44.

4.4.2 Removal of gaps by manual classification of objects

To fix the channel discontinuity caused by the larger gaps the missing objects are classified manually. This is performed by classifying non-meander objects in the object set that resulted from § 4.3.2. For the non-meander objects in this object set segmentation scale 7 was used to retain the possibility to classify gaps of relatively small channels but not hamper the classification of gaps of larger channels. For the classification only objects that make up a gap in the network whilst clearly representing a channel are used. Then the manually added meander objects are merged with the already existent meander objects to finalize the gap removal.

The action of manually adding objects to the classification resulted from an assessment of multiple computer automated methods for the removal of gaps:

- Merging bordering objects with meander objects if their spectral difference is smaller than a specified threshold.
- Merging bordering objects with meander objects if their shape index is larger than a specified threshold.
- A combination the previous two methods.
- Pixel growing the channel ends if the candidate pixels have a spectral difference smaller than a threshold.

Namely, these procedures were not capable of accurately classifying the missing meander objects and therefore did not improve the network quality. Nevertheless, an improvement of the channel network was required for further meaningful river analysis.

4.4.3 Removal of skeleton artefacts due to islands

The islands present in some channel objects are hampering geometry analysis of the object skeleton. Namely, the skeleton will contain a circular main line around the island with the rest of the object represented by branches that branch off the main line (fig. 45). As for

the river geometry analysis the only workable situation is a single channel line with no artefacts, the skeleton looping needs to be addressed.

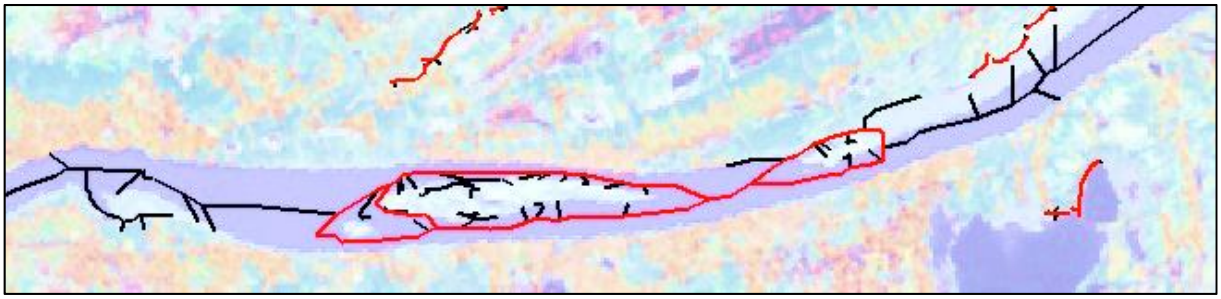

Figure 45: Example of the skeleton looping artefact at an island location. The skeleton main line and its branches are shown in resp. red and black.

The islands are removed by first finding objects that are entirely enclosed by a meander object. The island objects are then classified and bordering island objects are merged to yield a single object per island. The islands are now to be merged with the regular channel though one issue obstructs direct appliance of this merge. Namely, there are five large islands that are due to active meander cut-offs (fig. 46). These must be left out of the merge because it is not desirable to generate a wide bulbous channel at these locations as that would significantly influence the geometry analysis.

The solution is the removal of island objects that have a larger pixel count than the with trial and error determined threshold of 1000 pixels from the island class before merging the islands objects with the meanders. At this moment, the large islands that were not incorporated in the merge remain an issue as they cause skeleton looping to still occur. To resolve this, the chute cut-off is deleted from the meanders to finalize the object processing.

Figure 46: Example of an island that is created by an active meander cut-off. Meanders objects are shown in yellow and islands in blue.

4.4.4 Obtainment of channel centerlines by skeleton alteration

Besides the skeleton looping, the skeletons still have numerous small (sub)branches that are attached to their main lines (fig. 45 & 47) and they can therefore not yet be used in the river geometry analysis. To remove the branches, algorithms that alter the polyline skeletons are applied.

First the skeleton polylines are divided into lines that go from node to node (fig. 47a). This is performed by first converting the polylines to singlepart lines, after which they are merged if two endpoints are coincident, but not if the number of endpoints is larger than two.

To remove the branches a dangle removal process is applied three times, i.e. the removal of lines that are not connected to another line at one of their endpoints. The first dangle removal only removes dangles shorter than 2000 m. This is performed to make sure that the large end parts of the skeleton that are part of the channel centerline are not removed, such as the leftmost dangle in figure 47a. Lines that now have become coincident with two endpoints due to the removal on or more dangles along their paths are merged (fig. 47b).

The process is repeated two times using dangle removal thresholds of 3000 and 6000 m to remove almost all branches of all skeletons. Additionally, relatively small isolated channel parts that cannot be analysed due to the lack of geometric information are removed by the process as well. The result is a channel network of lines that go from node to node, i.e. from bifurcation to confluence.

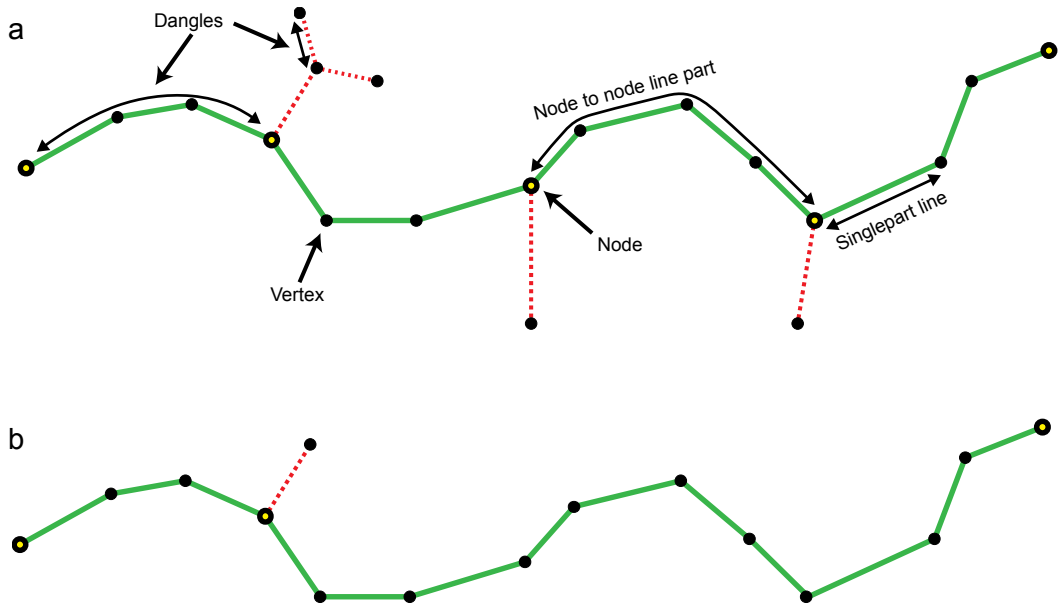

Figure 47: Sketches showing an initial skeleton (a), a skeleton after the first dangle removal (b) and the definitions used in this section. The main line and the branches are shown in resp. green and dashed red.

Some minor issues with the network remain due to the presence of some unwanted branches that cannot be analysed in the river planform analysis due to the lack of a clear meandering shape. These are to be removed manually because the use of a larger dangle removal threshold jeopardizes the preservation of channels that are useful in further analysis. A handful of other channel parts are too small to be analysed properly while they belong to river of which much larger line parts are present. To increase the analysability of those rivers the small lines are merged to the larger lines manually.

4.4.5 Analysis of the manually added objects

To determine if the characteristics of the manually added objects (§ 4.4.2) can be used to improve the automatic classification of similar channel objects the attribute data of all objects of scale 7, the meander objects of scale 7 and the manually added objects is evaluated by producing boxplots. The attributes that are used are nine shape and content related attributes that were found to be discriminants in terms of meander recognition in other research (Addink & Kleinhans, 2008; Kraaijenbrink, 2010): *border index*, *curvature-length ratio*, *compactness*, *polygon compactness*, *shape index*, *length-width ratio*, *water class contents, vegetation class contents* and *(semi-) bare class contents.*

4.5 Preparation of channel lines for geometry analysis

4.5.1 Determination of the channel line attributes

As the channels are now represented by lines and are edited as well, their attributes no longer correspond to the objects attributes. However, some of the object attributes are useful in the geometry analysis. Therefore they are derived from the attributes of the merged meander objects (§ 4.3.1).

To derive the attributes the meander objects are first split into smaller objects (fig. 48). The attributes of those smaller objects are then linked to the correct channel line by a spatial relation, i.e. a split meander object spatially coincides with a channel line (fig. 48). If multiple split objects coincide with a single channel line their attributes are aggregated based on a predefined merge rule (table 3).

In case of the skeleton width attribute, not all split objects that coincide with a channel line are used in an aggregation. This because the attribute is used to estimate the channel width and this is performed poorly if objects that have abundant riparian pollution are used as well. Therefore only objects that contain at least 80% water pixels are used in the attribute aggregation of the skeleton width.

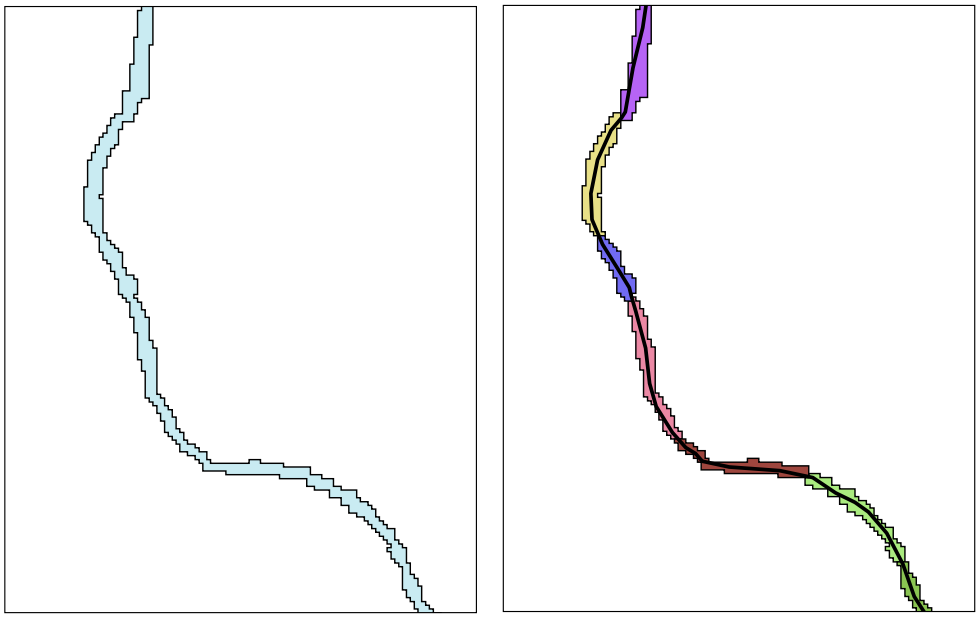

Figure 48: Example of channel objects before (left) and after (right) the splitting of the object. The black line in the right figure is a coinciding channel line. Different colours denote the different objects.

Attribute	Merge rule
Mean water class	Mean
Mean vegetation class	Mean
Mean (semi-)bare	Mean
Skeleton width	Mean
Skeleton length	Sum
Area (m^2)	Sum
Number of pixels	Sum

Table 3: The attributes that are determined for the channel lines and their corresponding merge rules.

4.5.2 Smoothing and regridding of the channel lines

The channel lines are spatially smoothed (fig. 49) to remove the negative effects of small irrelevant curvature changes and straight line sections to the curvature analysis that is performed during the river geometry analysis. The channel lines are significantly altered by this process though it is inevitable as the small curvature changes truly hamper the determination of a wavelength of the river lines.

For the geometry analysis it is furthermore important to have a (more or less) equal point interspacing of the line data. The smoothed lines are therefore regridded (fig. 49) to a point interspacing of 30 m.

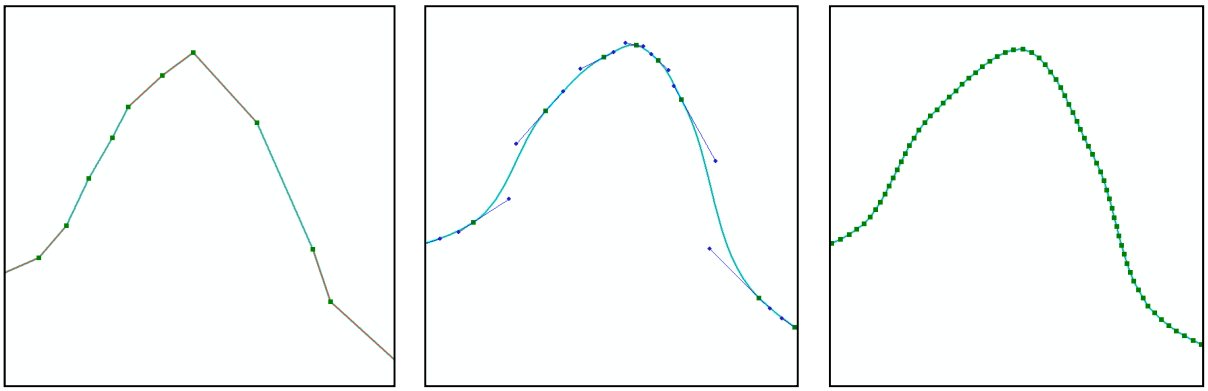

Figure 49: Example of the change in vertices after smoothing and regridding a line. Left: vertices of the processed skeleton. Middle: Vertices (arcs) of a smoothed line. Right: vertices of a regridded, smoothed line.

4.6 River geometry analysis

The remaining river dynamics analysis is performed in MATLAB (The Mathworks, 2011). This section provides an overview of the calculations that are performed to achieve the results. Not all specific calculations as well as the script build-up are presented here as that would be tedious. The MATLAB script is enclosed as appendix B.

The analysis briefly comprises that:

- The curvature of the channel lines is analysed to find inflection points.
- The interspacing of the inflection points is used to approximate the meander wavelength.
- The meander wavelength is used determine the channel forming discharge.
- The channel length and inflection interspacing are used to approximate sinuosity.
- A second order analysis is performed to determine the discharge of larger scale meandering that is present in the general course of numerous rivers in the study area.

4.6.1 Determination of vertex lengths

The dynamics calculations performed in this section is based on the length along the river, i.e. the length along the river is used as the independent variable. The x and y-coordinates of the vertices are treated as dependant variables of the length along the channel. To be able to do this, the exact along channel position of every point needs to be known. Though the regridding of the lines performed in the previous section is set to create vertices every 30 m the interspacing varies slightly and therefore needs to be calculated exactly first. This is performed on a per line basis using the following equation:

$$S_n = \sqrt{[(x_n - x_{n-1}) + (y_n - y_{n-1})]^2} \quad (10)$$

where x is x-coordinate, y is the y-coordinate and n is the index of the point that is currently calculated. From the vertex lengths the cumulative (Sc) and total channel lengths (Ss) of a line are derived

4.6.2 Determination of vertex angles and curvature

Because the meander wavelength is estimated using the inflection points of the river lines, it is necessary to determine on which locations along the river there is a change in the direction of the bends. To do this first a quantification of the direction at each line point is needed and therefore the angles at each point are determined. More specifically, the counter clockwise angle around the origin between two consecutive sets of points (fig. 50) is determined, which is calculated by:

$$\theta_n = \text{atan2}\left(A, B\right) \cdot \frac{180}{\pi} - 180 \tag{11}$$

where A and B are defined as

$$A = (x_{n-1} - x_n) \cdot (y_{n+1} - y_n) \; - \; (x_{n+1} - x_n) \cdot (y_{n-1} - y_n)$$

$$B = (x_{n-1} - x_n) \cdot (x_{n+1} - x_n) \; + \; (y_{n-1} - y_n) \cdot (y_{n+1} - y_n)$$

and where atan2 is defined as (The Mathworks, 2011):

$$\text{atan2}(y,x) = \begin{cases} \arctan(\frac{y}{x}) & x > 0 \\ \arctan(\frac{y}{x}) + \pi & y \geq 0, x < 0 \\ \arctan(\frac{y}{x}) - \pi & y < 0, x < 0 \\ +\frac{\pi}{2} & y > 0, x = 0 \\ -\frac{\pi}{2} & y < 0, x = 0 \\ \text{undefined} & y = 0, x = 0 \end{cases}$$

As slight differences exist in the interspacing of the points, the angle between two consecutive sets of points is not yet a fully accurate description of the direction of the river line at each point. To obtain the true curvature, the angle at each point needs to be normalized by the vertex length at that point. This is done by using the curvature definition from Chen & Duan (2006) that is given in equation 2 as follows:

$$C_n = \theta_n / S_n \tag{12}$$

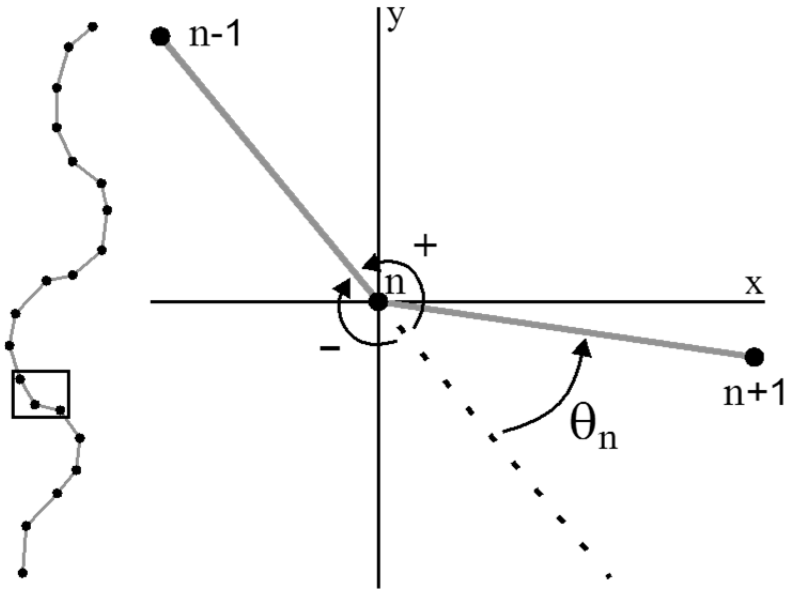

Figure 50: Sketch showing the counter clockwise angle around the origin between a consecutive set of points.

4.6.3 Calculation of weighted average of the curvature

Though the lines that are imported into MATLAB are already smoothed to reduce the negative effects of irrelevant small curvature changes and straight channel sections on the determination of inflection points, the effects still persist to a small extent. To further reduce it, the weighted average (Anton et al., 2005) of the curvature is determined using:

$$\overline{C_n} = \frac{1}{22}(C_{n-8} + C_{n-7} + \ldots + C_{n-2} + 2C_{n-1} + 4C_n + 2C_{n+1} + C_{n+2} + \ldots + C_{n+8}) \quad (13)$$

4.6.4 Determination of the inflection points

The inflection points are defined as the position along the channel where the direction of the bend changes, i.e. where the sign of the angle or curvature changes. These positions are determined for both C and $\overline{C}$. If a sign change exists at $\overline{C_n}$ there is searched in the vicinity of point n for a sign change in C. Searching is done by stepwise checking C at:

$$n-1 \rightarrow n+1 \rightarrow n-2 \rightarrow n+2 \rightarrow \ldots \rightarrow n-10 \rightarrow n+10$$

At the first sign change of C that is found (at C_{fsc}), C is evaluated to determine which point on each side of the sign change has the smallest angle (at C_{sa}) and thus lies closest to the true inflection position where the angle theoretically is 0. The point with the smallest angle is assigned as the inflection point, i.e. $\mathrm{I}_{sa} = 1$ (fig. 51). The inflection coordinates $\mathrm{I}x_{sa}$ and $\mathrm{I}y_{sa}$

are equal to x_{sa} and y_{sa}. At all points of a line where there is no inflection point present I_n, $\mathrm{I}x_n$ and $\mathrm{I}y_n$ are set to *NaN* (Not a Number).

The inflection point interspacing is calculated similarly as the vertex lengths in § 4.6.1, yielding S_n^{Inf}, Sc_n^{Inf} and Ss^{Inf}. The along channel length between consecutive inflection points is determined using the differences in Sc at the consecutive n indices where $\mathrm{I}_{sa} = 1$.

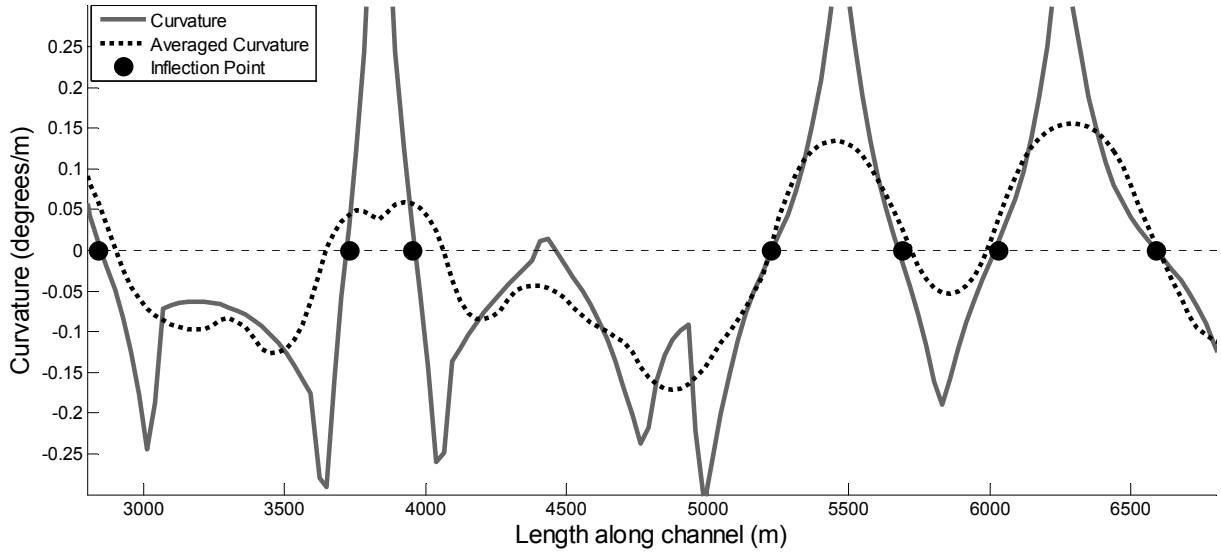

Figure 51: Example of the curvature C, its weighted average $\overline{C}$ and the determined inflections I.

4.6.5 Calculation of discharge and sinuosity

Though the wavelength of a freely flowing meander can be difficult to determine (Leopold & Wolman, 1960), especially when generalizing for a whole river, an approximation is made by using two times the inflection points interspacing. As mentioned in the literature review it is difficult to choose the right statistic to describe a meandering river. Therefore the wavelength is calculated for six different inflection interspacing statistics: the minimum, first quartile, median, mean, third quartile and maximum. The mainly used statistic however is the median.

Using the meander wavelength the discharge is subsequently estimated with the following empirical relation:

$$\lambda = \alpha Q^{\beta} \qquad \rightarrow \qquad Q = \left(\frac{\lambda}{\alpha}\right)^{1/\beta} \tag{14}$$

The values for α and β used here are resp. 72.16 and 0.49 (Mackey (1993), according to Bridge (2003)(Bridge, 2003)). These specific values are used as they were determined for

the bankfull discharge and, as already mentioned, this discharge measurement is closely related to the channel forming discharge (Copeland et al., 2005). Assumed is that the latter is more precise and accurate in its results here, as discharge is purely deducted from the channel form. Furthermore the relation between channel forming discharge and meander geometry is thought to be less variable for different rivers than other types of discharge measurements.

A first approach to calculate sinuosity is performed using the total along channel length and the total inflection point interspacing:

$$\mathrm{SN} = \frac{Ss}{Ss^{\mathrm{Inf}}} \tag{15}$$

4.6.6 Fitting of a spline through the inflections

Larger meander scales of past discharge regimes are clearly visible for various channels in the study area (fig. 15 & 53). To determine the mean wavelength and subsequently the discharge of these larger meanders, second order inflection points are calculated. The second order inflection points are determined for a spline that is fitted through the inflection points. The spline is only calculated for channels that have at least 6 inflection points, as channels with fewer points are assumed to be too small to analyse on potential larger meander scales.

The spline that is used is based on a weighted-factor cubic function. It calculates the line segment between two consecutive inflection points using two second-degree functions that are both fitted through tree points: the two inflection points and the next or the previous indexed point (fig. 52). The two second degree functions are defined by (Hildebrand, 1990):

$$\begin{aligned} x_n &= \mathrm{a}t^2 + \mathrm{b}t + \mathrm{c} & x_{n+1} &= \mathrm{g}t^2 + \mathrm{h}t + \mathrm{i} \\ y_n &= \mathrm{d}t^2 + \mathrm{e}t + \mathrm{f} & y_{n+1} &= \mathrm{j}t^2 + \mathrm{k}t + \mathrm{l} \end{aligned} \tag{16}$$

The parameters used in these functions are defined by:

$$\mathrm{a} = \frac{x_{n-1} - 2x_n + x_{n+1}}{2} \qquad \mathrm{b} = \frac{x_{n+1} - x_{n-1}}{2} \qquad \mathrm{c} = x_n$$

$$\mathrm{d} = \frac{y_{n-1} - 2y_n + y_{n+1}}{2} \qquad \mathrm{e} = \frac{y_{n+1} - y_{n-1}}{2} \qquad \mathrm{f} = y_n$$

$$g = \frac{x_n - 2x_{n+1} + x_{n+2}}{2} \qquad h = \frac{-3x_n + 4x_{n+1} - x_{n+2}}{2} \qquad i = x_n$$

$$j = \frac{y_n - 2y_{n+1} + y_{n+2}}{2} \qquad k = \frac{-3y_n + 4y_{n+1} - y_{n+2}}{2} \qquad l = y_n$$

With $0 \le t \le 1$, the parametric cubic function is computed by:

$$x(t) = (1-t)x_n + tx_{k+1}$$
$$y(t) = (1-t)y_n + ty_{k+1} \qquad (17)$$

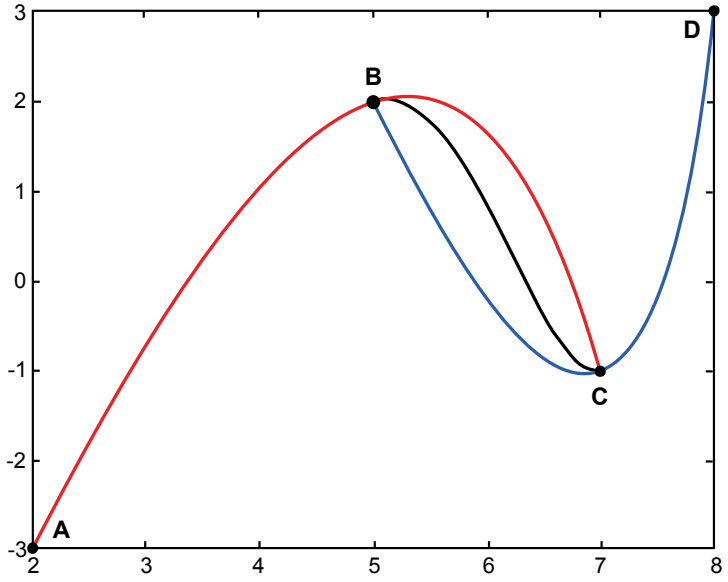

Figure 52: Line segment between B and C is interpolated. A and D are used to compute the coefficients for two second-degree functions (blue and red). Both functions are used to determine the cubic function between B and C (black) (Schuurman, 2008).

The x and y coordinates of 500 equally spaced points, i.e. at a *t* interval of 0.002, are computed from these functions to represent the spline between two consecutive inflection points. At the first and last two points of a line the weighted-factor cubic function cannot be calculated and one second order function (eq. 16) is used instead. Combining the computed points for every line segment into one set yields the full spline.

The inflections spline is yet too spatially detailed to detect the inflection points of the larger scale meanders. To generalize the x and y-coordinates of the spline they are smoothed. In this process the span of the averaging moving window can be varied by altering the defined smoothing parameter *sp.*

After smoothing, the spline has to be regridded before it can be used in the second order inflection calculation. This because the point interspacing along the meander is variable, caused by the fact that the inflections are unequally spaced while equal amount of points are drawn between them. Furthermore, the smoothing causes changes to occur in the interspacing of the spline points. The new interspacing of the points is determined using the skeleton width of the channel (§ 4.5.1) as follows:

$$\text{Interspacing} = ip \cdot \mathrm{W} \tag{18}$$

where ip is the interspacing parameter and W the skeleton width. For channels where the width is absent, it is first derived from the calculated first order wavelength by using eq. 4:

$$\text{Interspacing} = \gamma \cdot ip \cdot \left(\frac{\lambda}{\alpha} \right)^{1/\beta} \tag{19}$$

where α = 11.03, β = 1.01 (Leopold & Wolman, 1960) and γ is a calibration parameter which is set to 5 by determining it with trial and error.

The following variables are all computed with methods similar to those in described in previous sections:

- Spline vertex lengths (S_n^{Spl} , Sc_n^{Spl} , Ss^{Spl})
- Angles between the spline vertices (C_n^{Spl} , $\overline{C_n^{\mathrm{Spl}}}$)
- Second order inflection points ($\mathrm{I}_n^{\mathrm{2nd}}$)
- Second order inflection interspacing (S_n^{Inf2} , Sc_n^{Inf2} , Ss^{Inf2})
- Second order Wavelength (λ^{2nd}). It is only calculated using the mean second order inflection interspacing due to the limited amount of second order inflections.
- Second order Discharge (Q^{2nd})
- The spline based sinuosity of the channels is determined by $\mathrm{SN}^{\mathrm{Spl}} = \frac{Ss}{Ss^{Spl}}$

By varying the smoothing parameter, the inflection points of different meander scales can be determined. Though an overall relatively good accuracy of second order inflections is achieved, it appears impossible to define a smoothing and interspacing parameter that yields the most accurate second order inflections for every river in one model run. Therefore a separate version of the script is created that allows subjective fine-tuning of the smoothing

and interspacing parameter on a per river basis as well as the option to set the endpoints of a river line as second order inflections, which is useful for some river lines.

A downside to this method is that the spline based sinuosity is calculated differently for every channel, which makes statistical analysis incorrect. Therefore the sinuosity is determined in a separate model run that uses constant smoothing and interspacing parameters of resp. 600 and 1, which are thought to result in a spline that approximates the channel belt centerline most accurately (fig. 53).

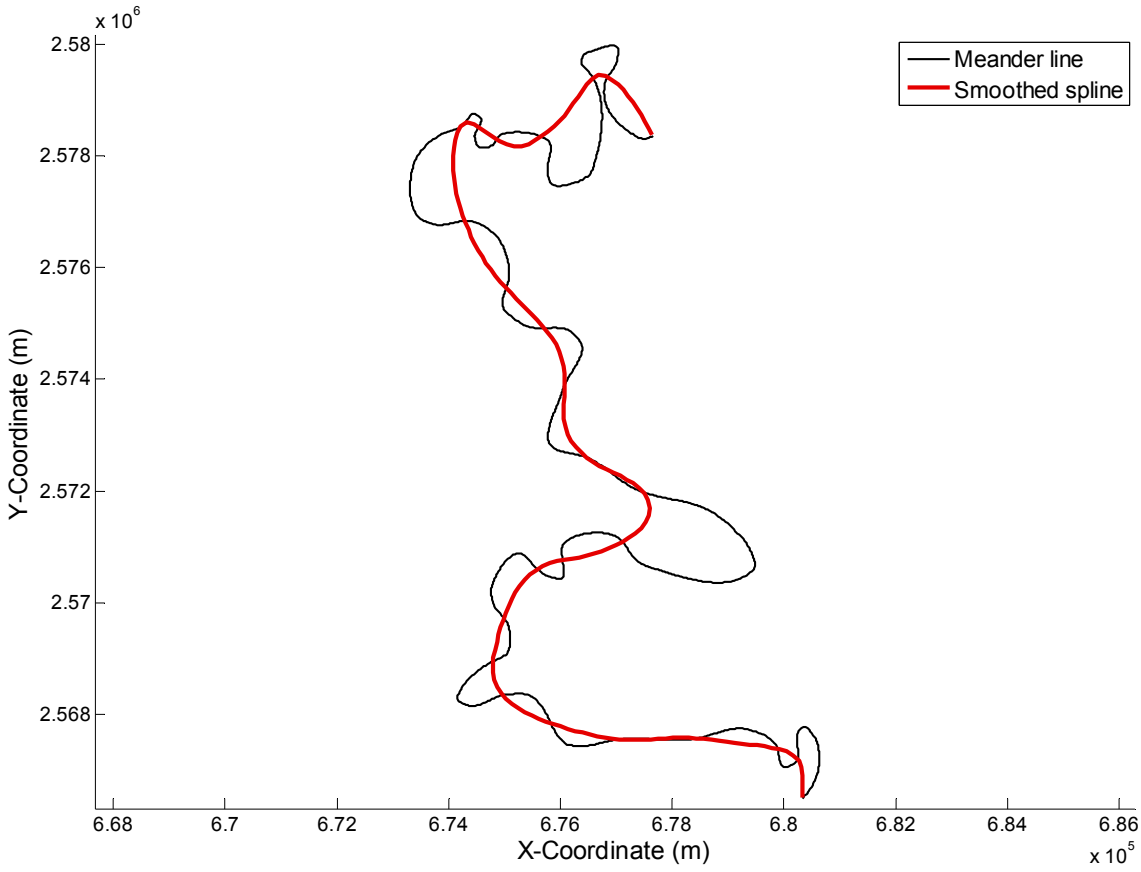

Figure 53: Example of meander line and its spline (sp=600 and ip=1) that is used to approximate the channel belt centerline.

5. RESULTS

5.1 Obtained meander objects

5.1.1 Delineation of the meanders

Subsets of the segmentations performed with the different scale parameter values (§ 4.2.1) are shown in figure 54. The number of objects that result from the segmentation decrease exponentially with an increase of the scale parameter (table 4).

The shape index values that best discriminate between meander and non-meander objects in the training sets are shown in table 5. The accuracy of these thresholds ranged from 91-96% within all training sets. The shape index value for the classification of the segmentation that resulted from scale parameter 100 is set to 2.1, determined by trial and error due to the lack of training objects. The threshold for scale 100 is lower than for the other scales due to the fact that the meanders it delineates are from a truly larger scale, which causes the contrast in heterogeneity with their surroundings to be relatively larger.

After applying the shape index threshold to the objects of the different segmentation levels, the number of resulting objects that are classified as meanders are shown in table 4. Subsets of the meander objects of all levels are shown in figure 55. The different levels have similar as well as complementary information about the meanders present in the image. A combination of the meander objects from the different levels is shown in figure 56 and 57, with resp. segmentation levels that resulted from smaller scale parameter values on top of larger values and vice versa. For comparison the same subset of the Landsat image is shown in figure 58.

Scale parameter	Objects	Meander objects
5	286916	1408
7	152041	1063
10	75935	893
15	34542	716
20	19682	411
100	642	40

Table 4: The number of objects that are present and the number of meander objects that result from the classification for each segmentation level.

Scale parameter	5	7	10	15	20	100
Shape index threshold	2.64	28.525	30.225	3.184	34.645	2.1

Table 5: The determined shape index thresholds per segmentation level.

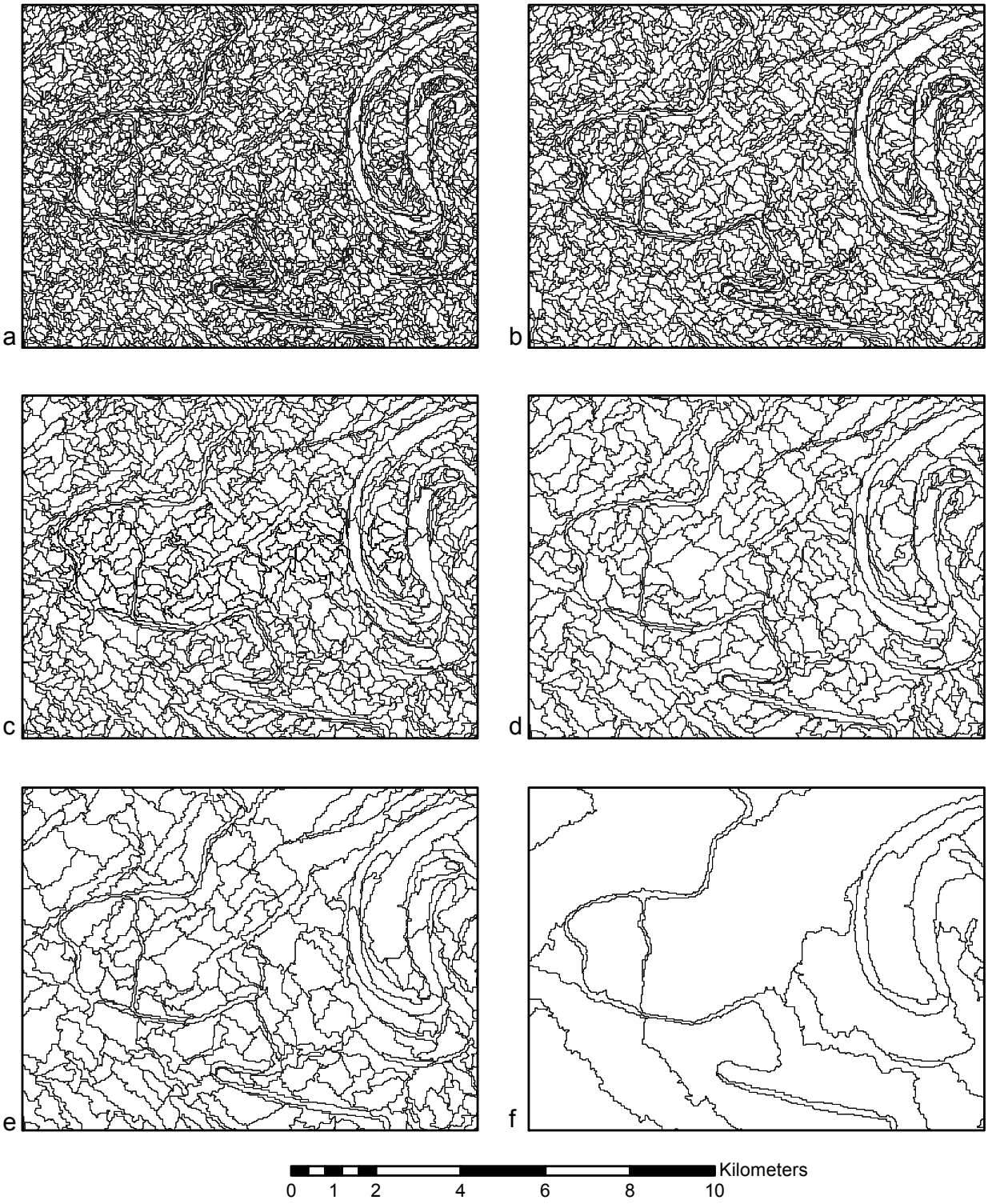

Figure 54: Subset of the objects that result from the different segmentation scales. Subfigures a-f resp. show the segmentations that result from scale parameter 5, 7, 10, 15, 20 and 100.

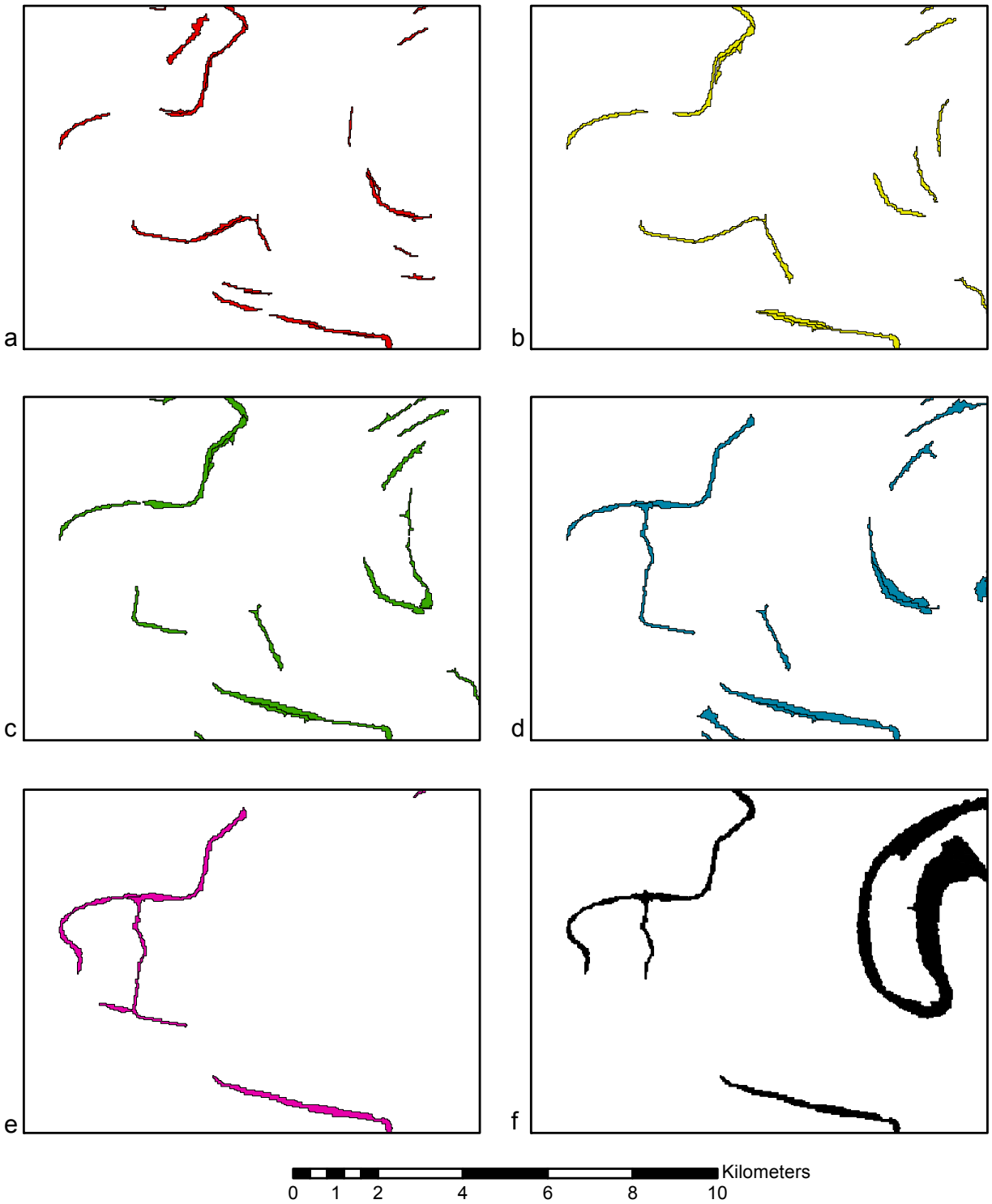

Figure 55: Subset of the meander objects that result from the different segmentation scales. Subfigures a-f respectively show the meander objects that result from the use of scale parameter 5, 7, 10, 15, 20 and 100.

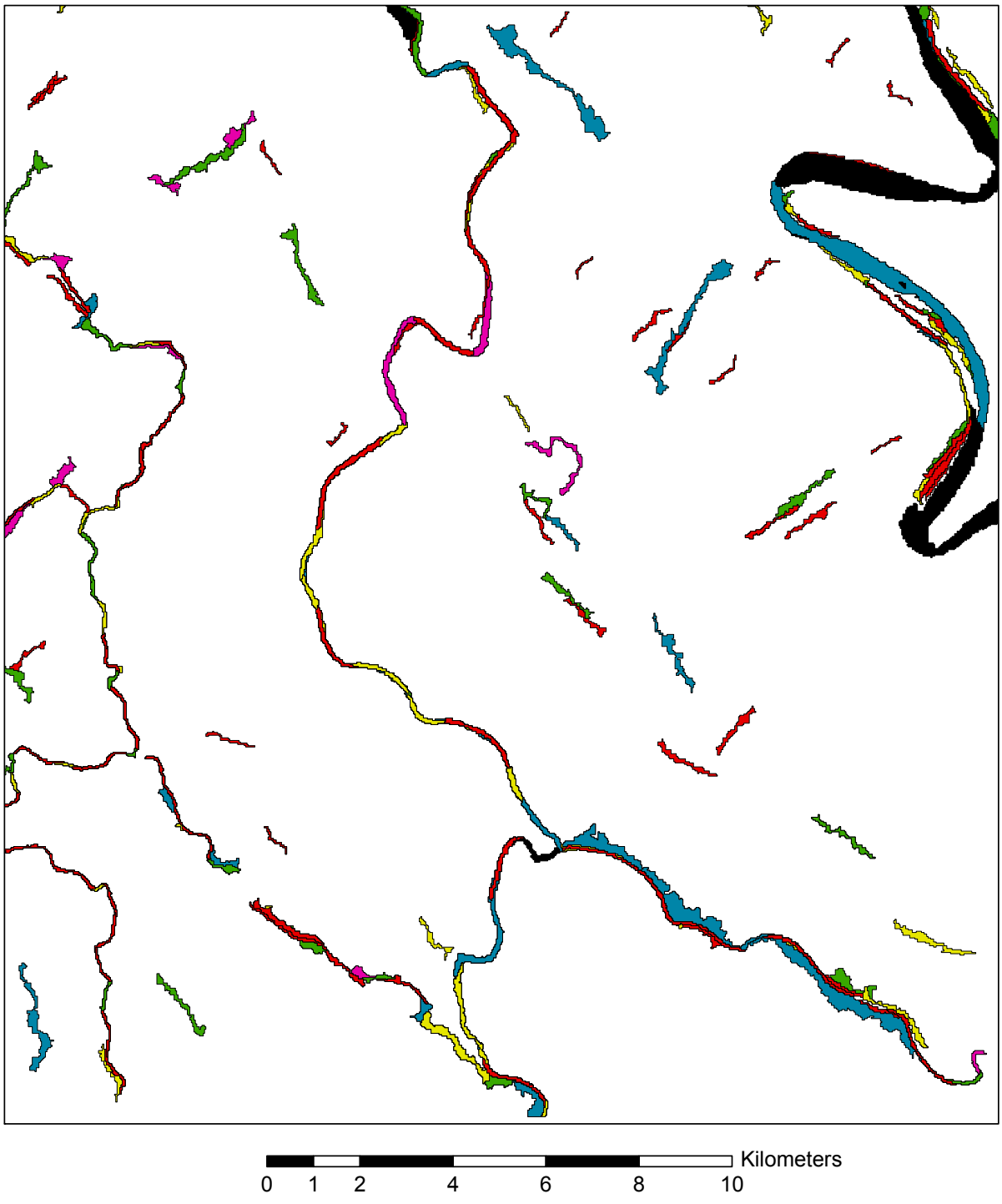

Figure 56: Subset of all meander objects combined showing objects that resulted from smaller scale parameters values on top of those that resulted from larger values. The scale colours are the same as presented in figure 59.

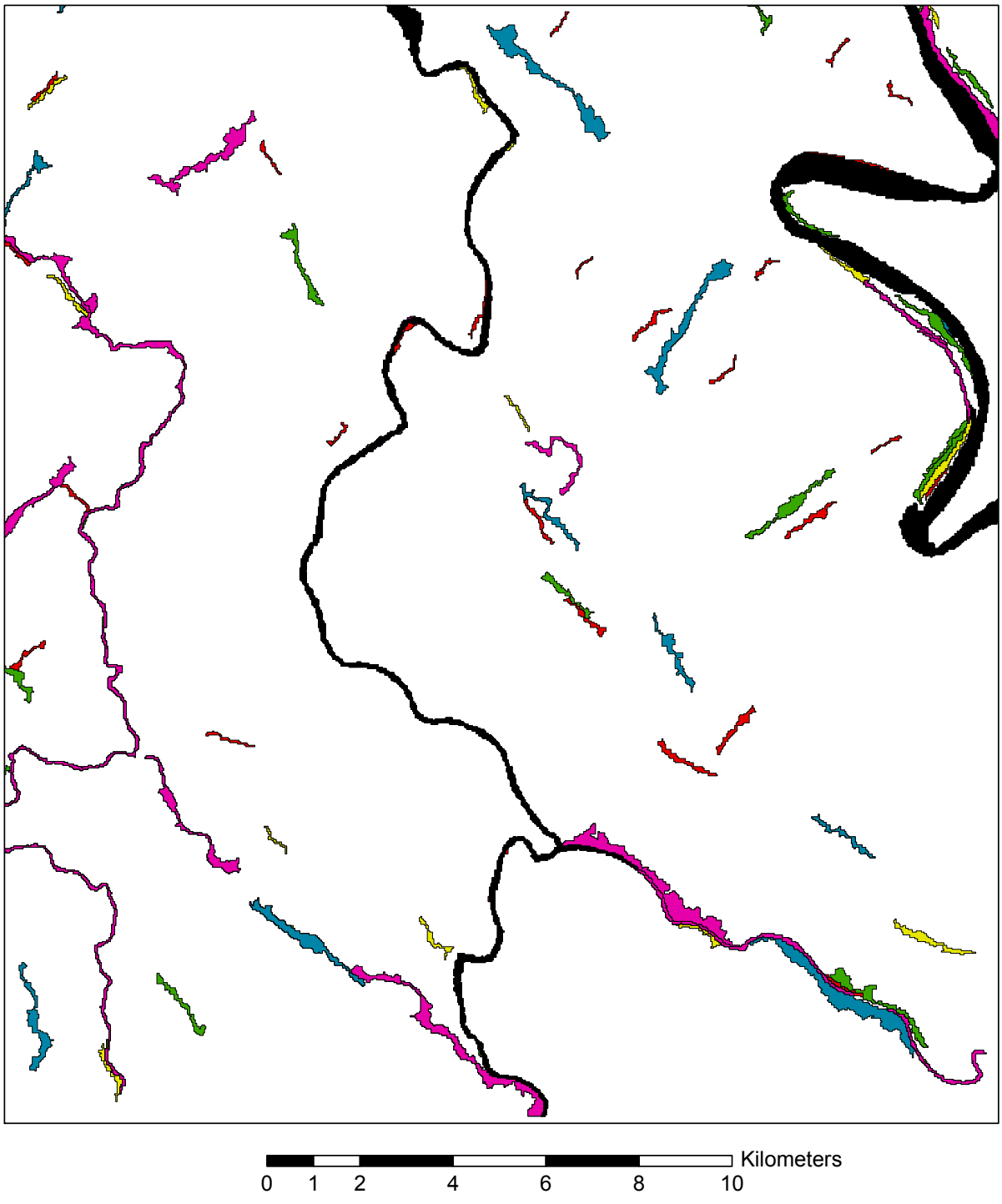

Figure 57: Subset of all meander objects combined showing objects that resulted from larger scale parameters values on top of those that resulted from smaller values. The scale colours are the same as in figure 59.

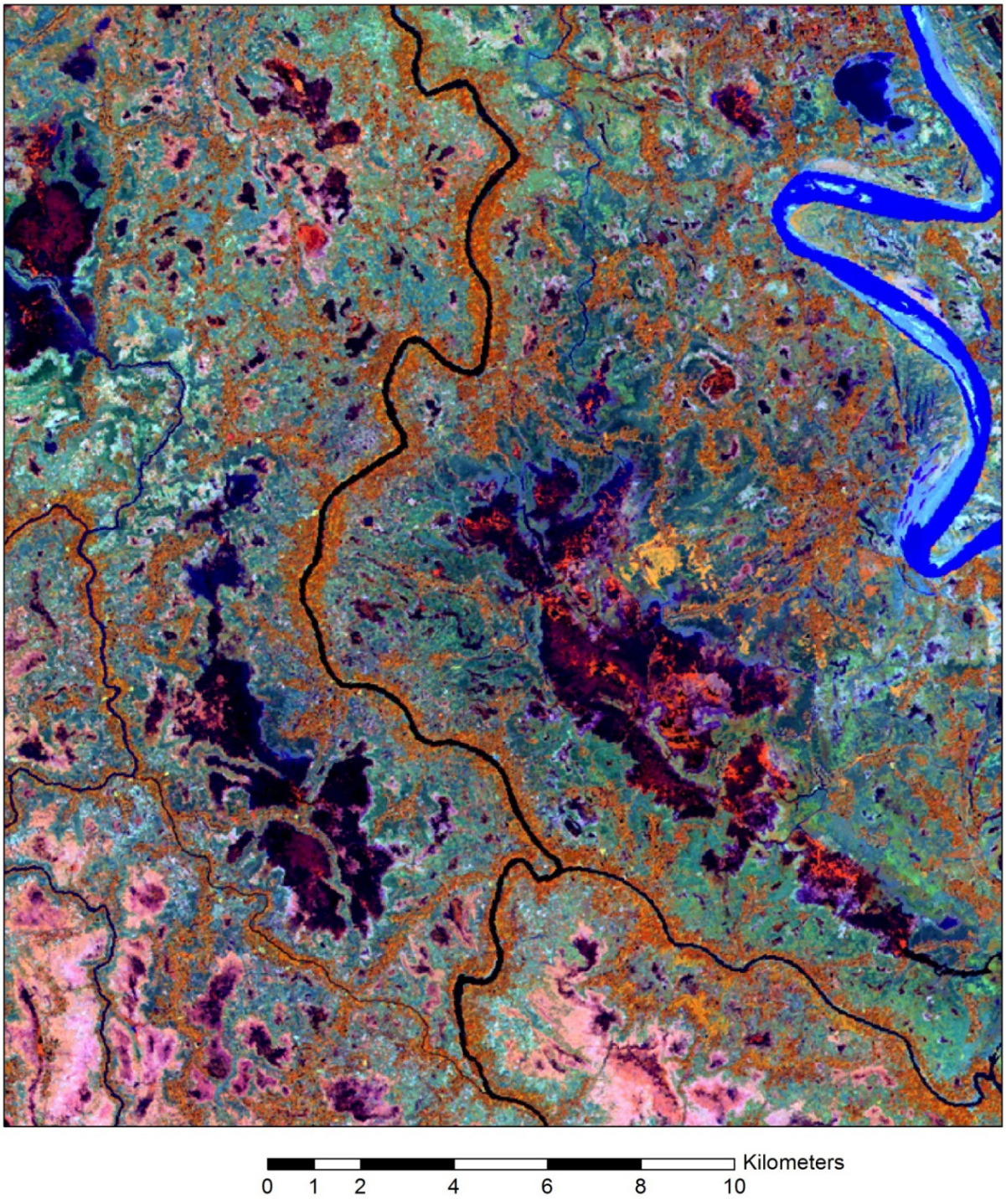

Figure 58: Subset of the Landsat 5 TM image, RGB=453.

5.1.2 Determined basic object contents

Subsets of the results of the tasselled cap transformation and the unsupervised k-means classification of the transform image (§ 4.2.3) are shown in resp. figure 59 and 60. When compared to the Landsat image, the overall accuracy of the classification is acceptable, i.e. the assigned pixel classes appear to be correct for the large majority of pixels.

The resulted overall object contents distributions are shown in the histogram of figure 61. The histogram makes apparent that the pixels belonging to objects that are classified as meanders are dominated by the water and vegetation classes. The (semi-) bare class has a significant lower share with a mean of about 10%. A slight decrease of water and increase in vegetation content can be noted with an increase of the scale parameter. This is caused by the riparian pollution that is more abundant at higher scales, as can be noted when comparing figure 56 and 57 with figure 58. The trend is not valid for scale 20 and 100, presumably because those scales consist of relatively more objects that represent wide channels, which are generally less polluted with bare or vegetation pixels.

The merged segmentation levels have a vegetation content that is larger than the water content and also an increased bare content. This may again be ascribed to the larger pollution at higher scales. Namely, larger pollution in combination with the significantly larger number of pixels of the higher scale objects causes a biased influence in the merged objects.

The pixels of the segmentation level created with scale parameter 100 are nearly completely dominated by water, despite the fact that this is the largest scale and much pollution may therefore be expected. This does not occur because at this scale only wide meanders that truly have a larger scale are delineated, such as the Hooghly and Gorai.

Figure 62, 63 and 64 show the percentage of objects that contain a specific percentage of resp. water, vegetation and (semi-) bare. The histogram of water shows an inversed bell shape, i.e. a large increase at the low and high percentage bins. This is logical as at the base of the segmentation algorithm lies the minimizing of the internal spectral heterogeneity of an object. The resulting objects will therefore contain similar pixels only that will most likely have equal classification results. Increasing the scale parameter reduces the heterogeneity of the objects and results in an increased mixing of pixel types. The latter can be observed from figure 62 as the histogram shape is flattened slightly for the larger scales.

The vegetation and (semi-) bare class histogram show skewed right hand distributions. This suggests that these classes are predominantly present in active channel objects that are polluted. The objects that contain 80-100% vegetation of (semi-) bare pixels are likely fossil channels. The relative decrease of larger scale objects in that range can be explained by the fact that the larger an objects is the less homogeneous it becomes.

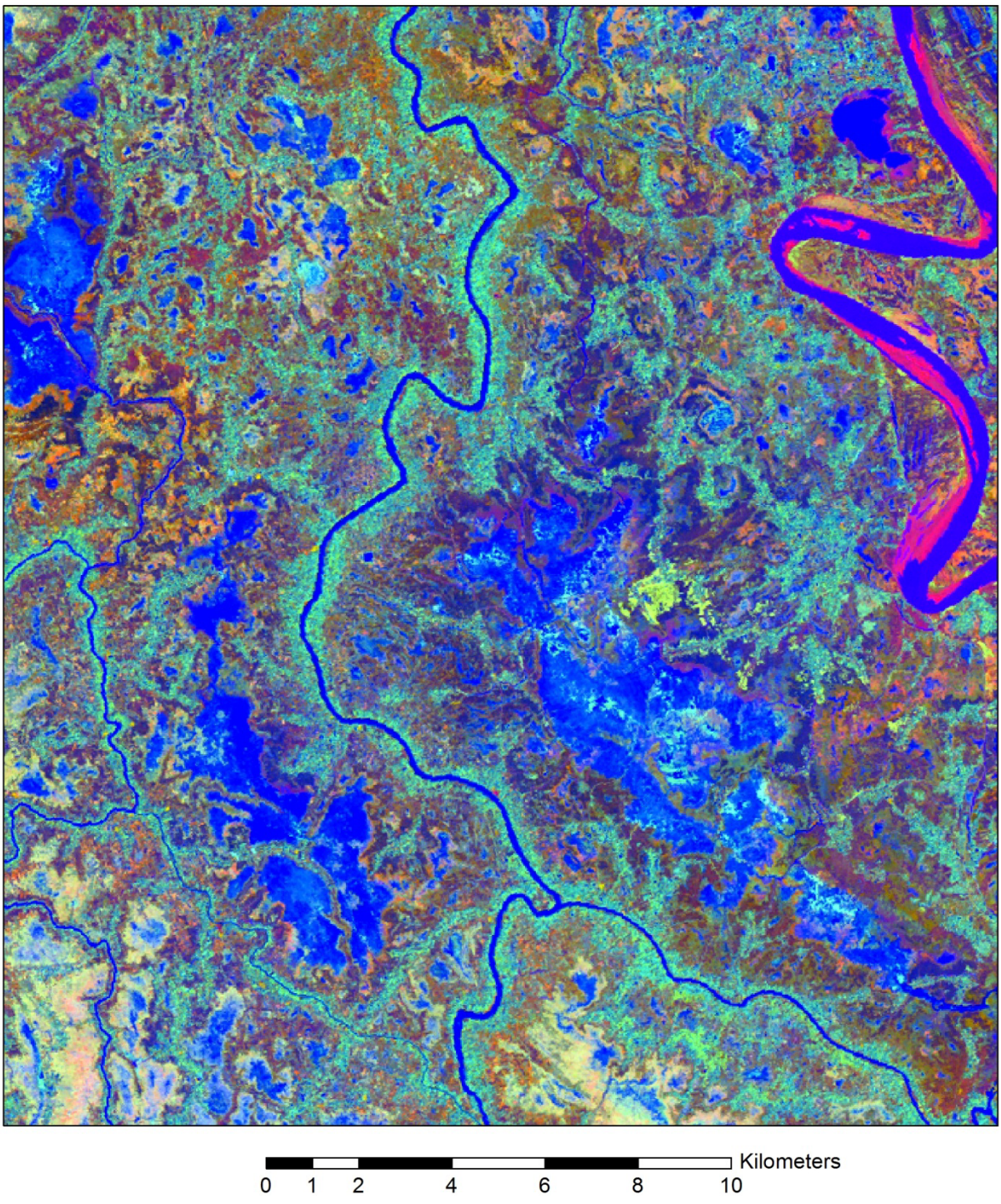

Figure 59: Subset of the tasselled cap transformed Landsat image, RGB = Brightness Greenness Wetness.

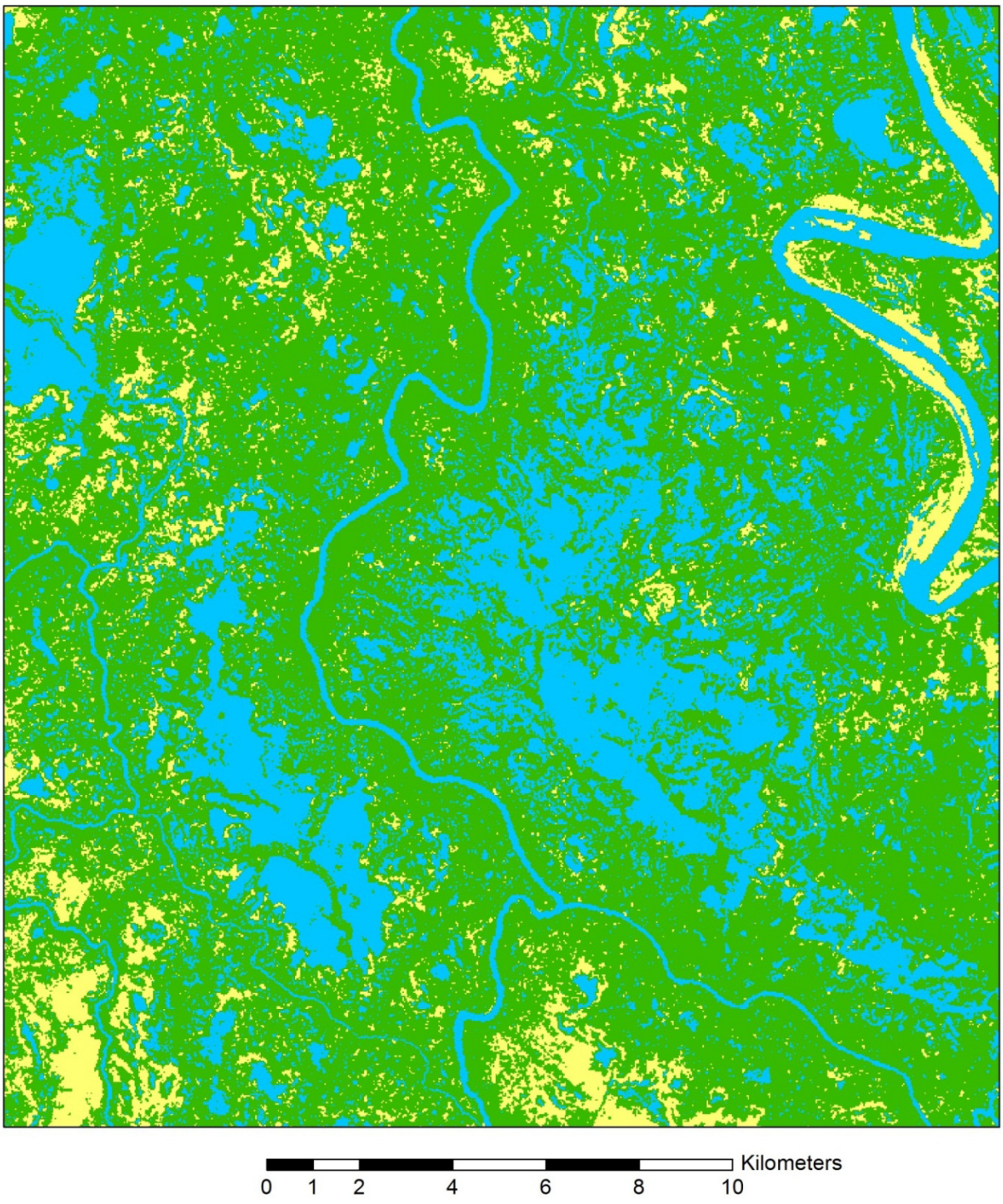

Figure 60: Subset of the unsupervised k-means classification of the tasselled cap transform. The classes water, vegetation and (semi-) bare are shown in resp. blue, green and yellow.

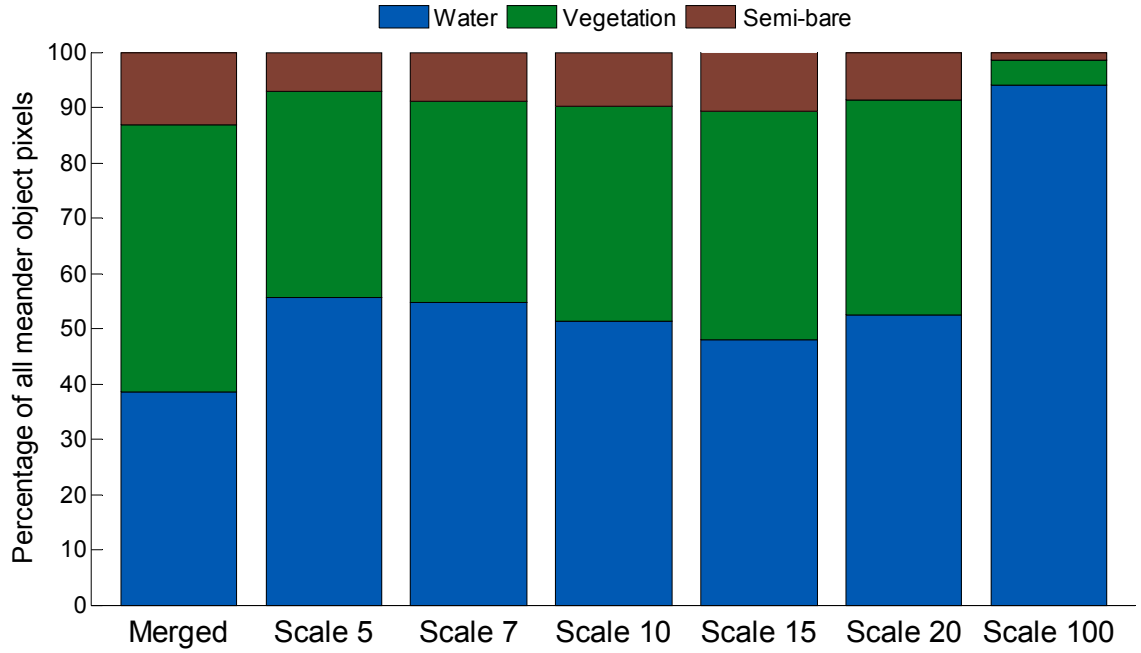

Figure 61: Overall distributions of the classes water, vegetation and (semi-) bare among the pixels of meander objects shown for all segmentation levels and for the merged dataset.

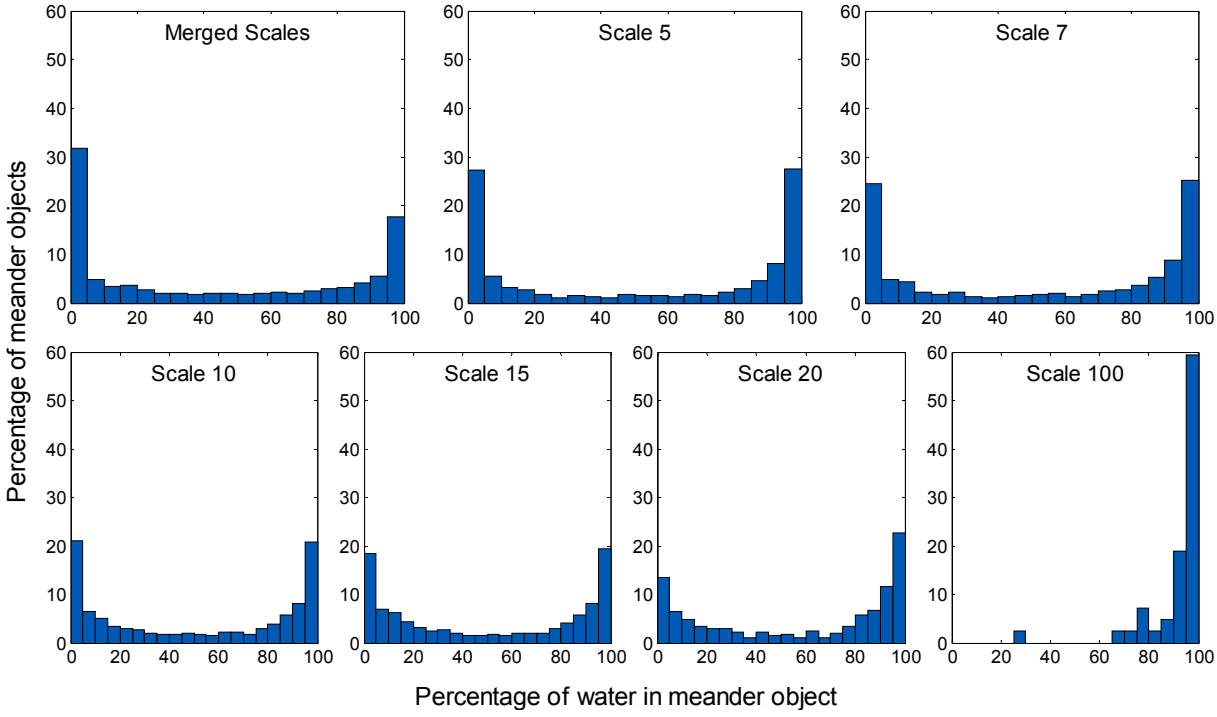

Figure 62: Histograms for all segmentation levels showing the distribution of the amount of water that is present in the meander objects.

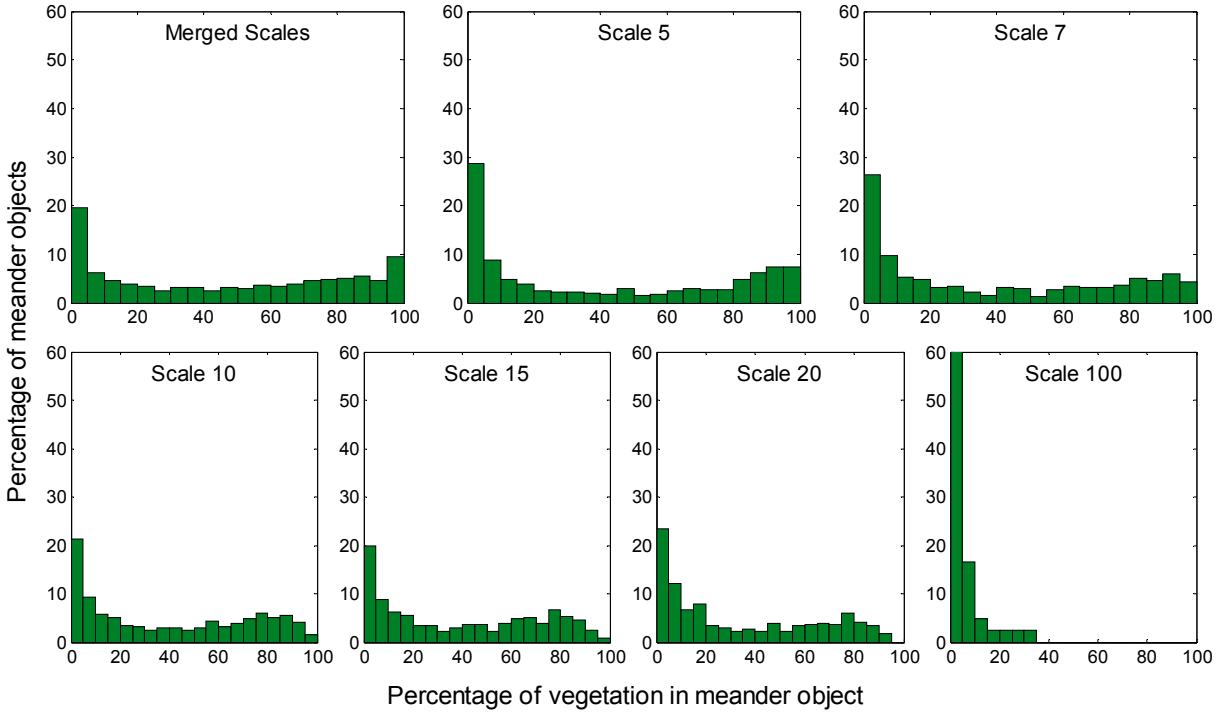

Figure 63: Histograms for all segmentation levels showing the distribution of the amount of vegetation that is present in the meander objects.

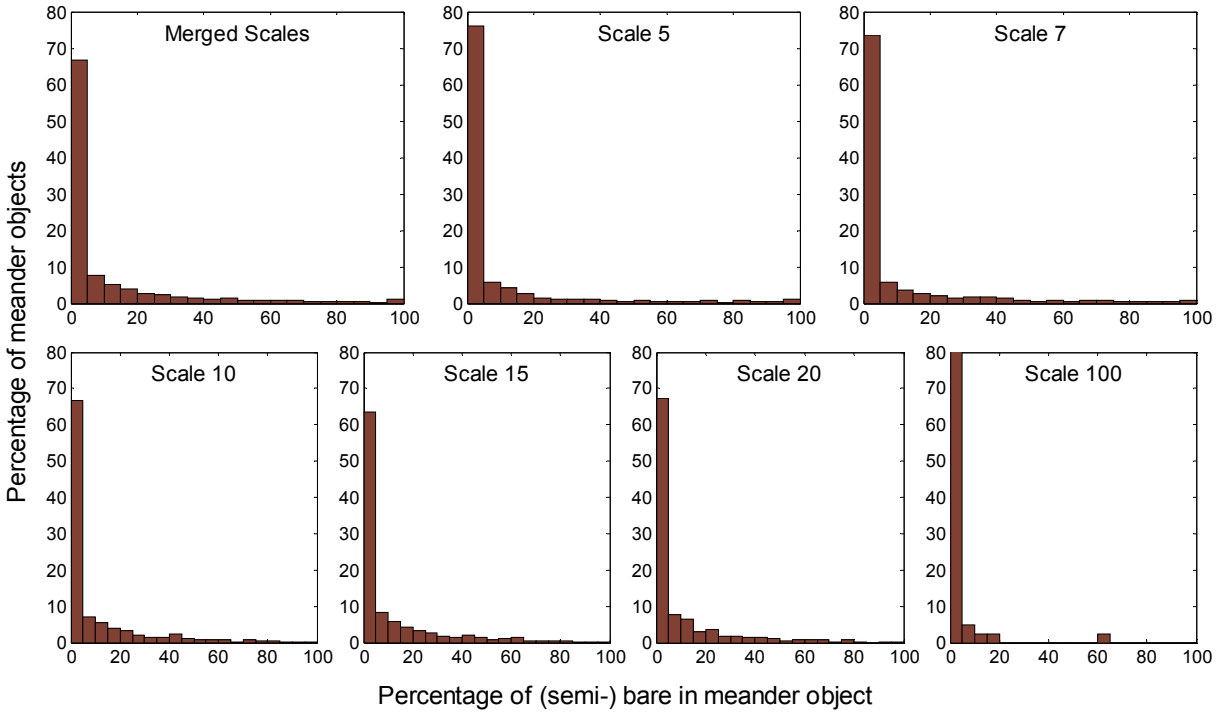

Figure 64: Histograms for all segmentation levels showing the distribution of the amount of (semi-) bare that is present in the meander objects.

A plot of the water content against the shape index for the objects that resulted from the image segmentation based on scale parameter 7 (fig. 65) shows there is no distinct relation between both attributes. The shape index values are a little larger at high water contents, caused by the presence of elongated, active channel objects. Though there seem to be many objects that have a low water content and a relatively high shape index, this is not true from a relative aspect, as the quartiles decrease in this region.

In the plot two types artefacts occur, i.e. horizontal and curved striping. These are both caused by the fact that the used data is not scalar, as both the water content as the shape index are originally based on numbers of pixels of an object. Objects can therefore only have certain fixed ratios in their water content as well as fixed shape indices. Naturally, this effect is more distinct for smaller objects of only a few pixels in size.

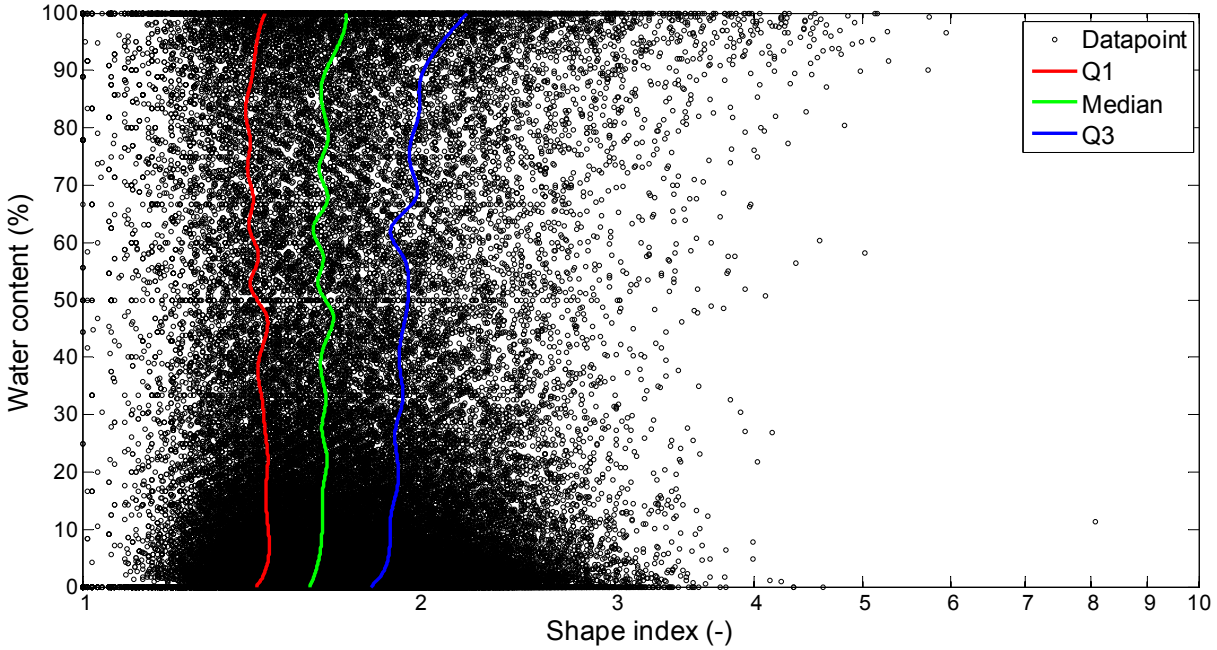

Figure 65: Plot of the water content against the shape index of all objects of scale 7. The lines in the figure represent the quartiles of the shape index, defined with a water content bin size of 2.5%.

5.2 Obtained single object set

The results of the merging of the six segmentation scales and the subsequent merging of individual objects (§ 4.3) are shown in resp. figure 66 and 67. The figures clearly show that the many small objects from multiple segmentation levels are successfully transformed into objects that represent larger parts of channels, but also that there is a remainder of small objects that hold little information on channel geometry.

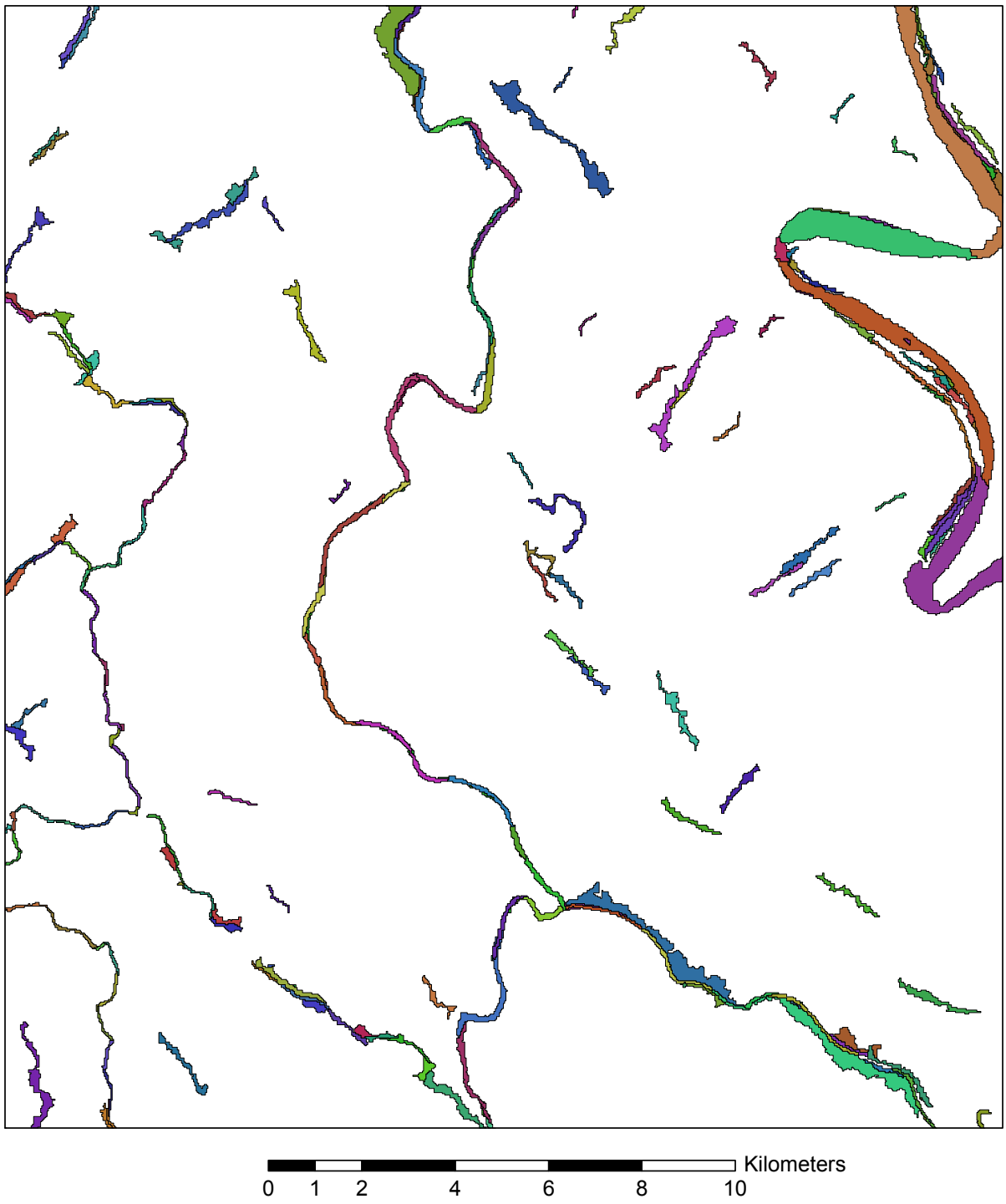

Figure 66: Subset of the merged segmentation levels. The various colours denote different objects.

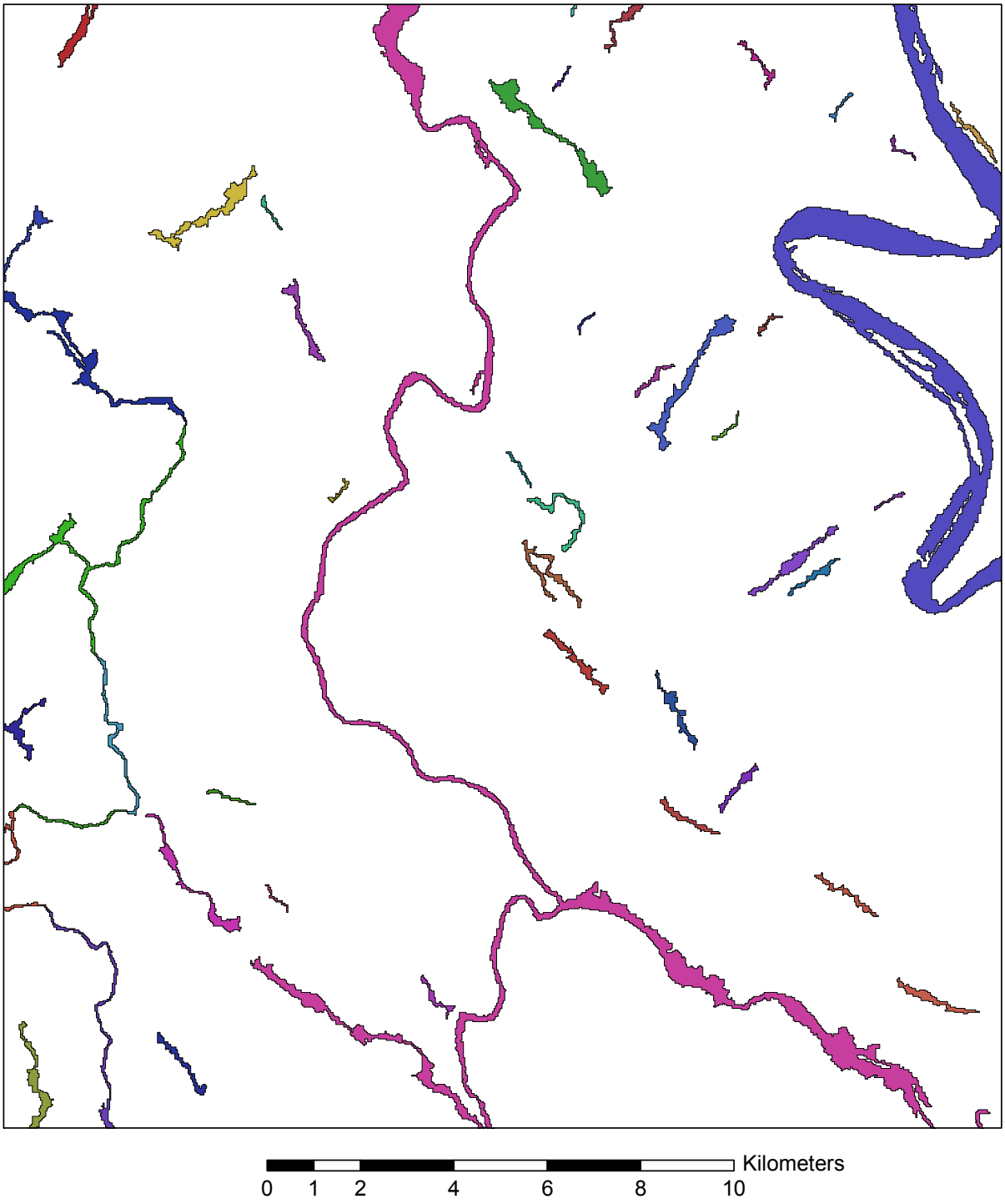

Figure 67: Subset of the merged objects that represent larger parts of the channels. The various colours denote different objects.

5.3 Performed channel network enhancements

5.3.1 Manually added objects

The objects that were manually added to the classification (§ 4.4.2) are shown in the map of figure 68. The complete set of merged meander objects are shown in figure 69 for comparison. A larger map combining both is included as appendix A3. The relation between the manually added objects, merged objects and total image objects are shown in figure 70 on a pixel basis. It shows that the pixel count of the manually added objects is resp. 0.30% and 5.59% of that of resp. the total image pixel count and the merged meander objects pixel count.

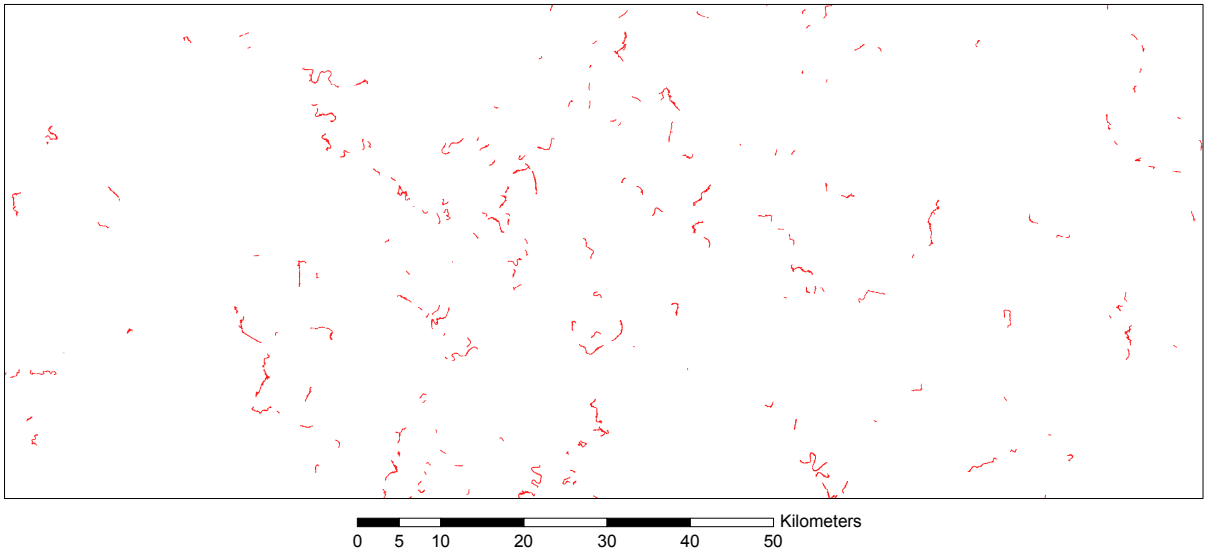

Figure 68: The manually added objects for the complete study area.

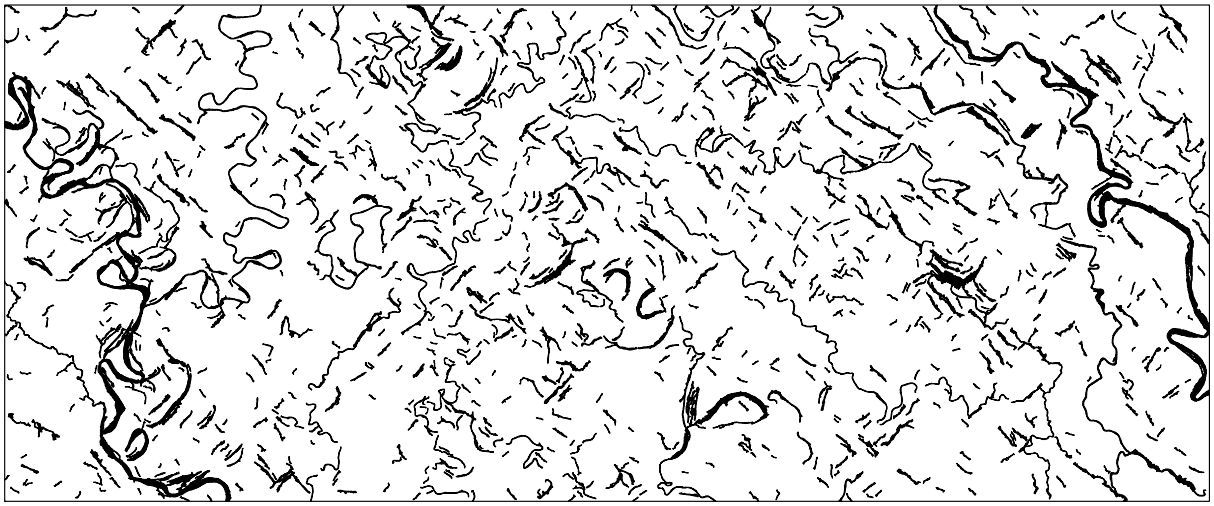

Figure 69: The merged objects for the complete study area.

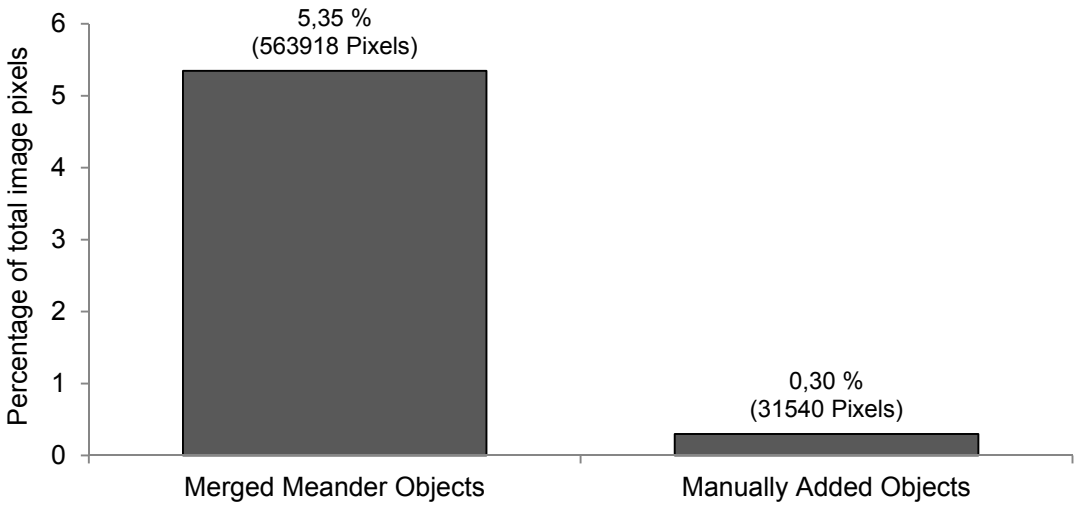

Figure 70: Comparison of pixel count of the merged and manually added objects to the total image pixels count (10550100). The manually added pixels count is 5.59% of that of the merged objects.

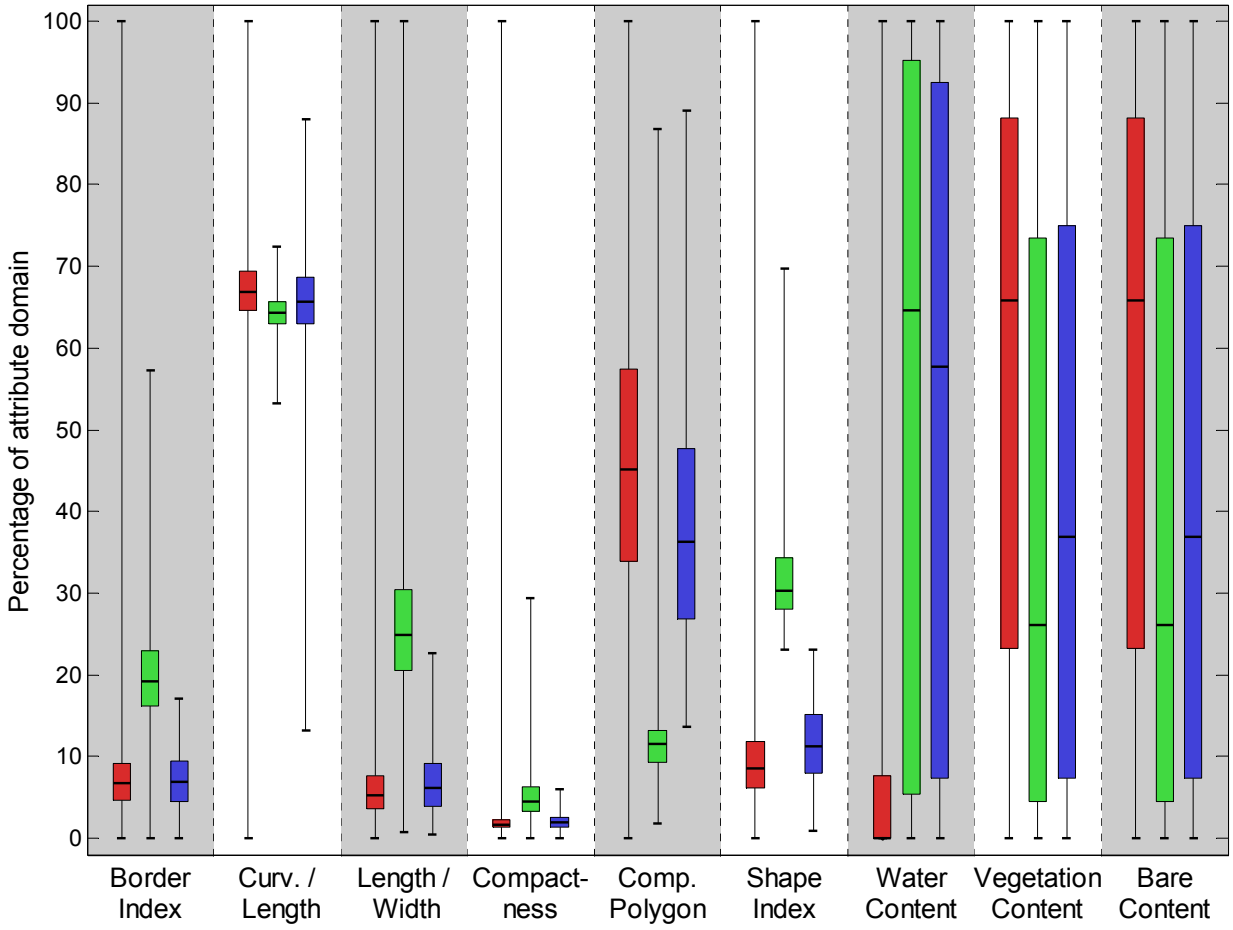

Figure 71: Boxplots showing the distribution of various attributes for all objects (red) and the meander objects (green) of segmentation scale 7, as well as the manually added objects (blue). The values are scaled per attribute to values between 0 and 100. As can be noted, the attributes cannot be used to discriminate between manually added objects and all objects as the distributions overlap each other to a great extent.

Figure 71 shows the distributions of the attributes of the manually added and meander objects compared to all objects from scale parameter 7. As can be noted, the attribute values for the manually added objects and all objects are overlapping to a great extent. Therefore no discriminating threshold values can be defined and thus the automatic delineation of objects that are similar to the manually added objects is impossible. The meander delineation that resulted from the use of the shape index thresholds as performed in this research appears to approach the most thorough delineation possible in this study area using object-based image analysis of a Landsat image.

5.3.2 Obtained channel centerlines

A subset of the results from the skeleton processing (§ 4.4.4), i.e. the removal of the skeleton branches, is shown in figure 73. A complete map of the results is included on the appendix A4**.** A comparison of the line lengths related to every step as well as the lines that are manually removed and merged are shown in table 6.

From the table follows that a substantial amount of skeleton lines is removed automatically and manually, a total of 80.43%. Most of the branches are removed in step 1, which removed the dangles smaller than 2000 m. It is a large percentage of the total lines, as the length of all the small branches that are removed in this step quickly add up. In the subsequent two steps mainly the small channel parts that cannot be accurately analysed are removed as well as some larger branches. The length of the lines that are manually merged and the lines that are manually deleted are only a small part of the total as well as a relatively small part of the remained lines.

Processing step	**Length (m)**	**% of initial skeleton**	
Initial skeleton	8823183	-	
Removed in 1st step	6256492	70,91	
Removed in 2nd step	497037	5,63	
Removed in 3rd step	214237	2,43	
Remained after 3rd step	1855417	21,03	
			% of the remaining lines
Removed manually	132442	1,50	7,14
Merged manually	67795	0,77	3,65

Table 6: Line lengths related to the each step in the skeleton processing. For comparison with the initial and remained lines, percentages are shown as well.

5.3.3 Determined channel line attributes

The class contents attributes of the channels lines that were obtained by the aggregation of the split meander object attributes (§ 4.5.1) are shown in figure 72. The aggregated skeleton width is shown as a colourmap. The figure shows that most channel lines consist of objects with a varying fraction of water and vegetation. The maximum vegetation content of any line is ca. 68% and the minimum water content ca. 12%. There are few channel lines that have an (semi-) bare attribute that is larger than 8%, with the maximum bare content being about 33%. The skeleton width ranges from about 44 to 359 m, with a median of 82 and first and third quartiles of resp. 68 and 98 m.

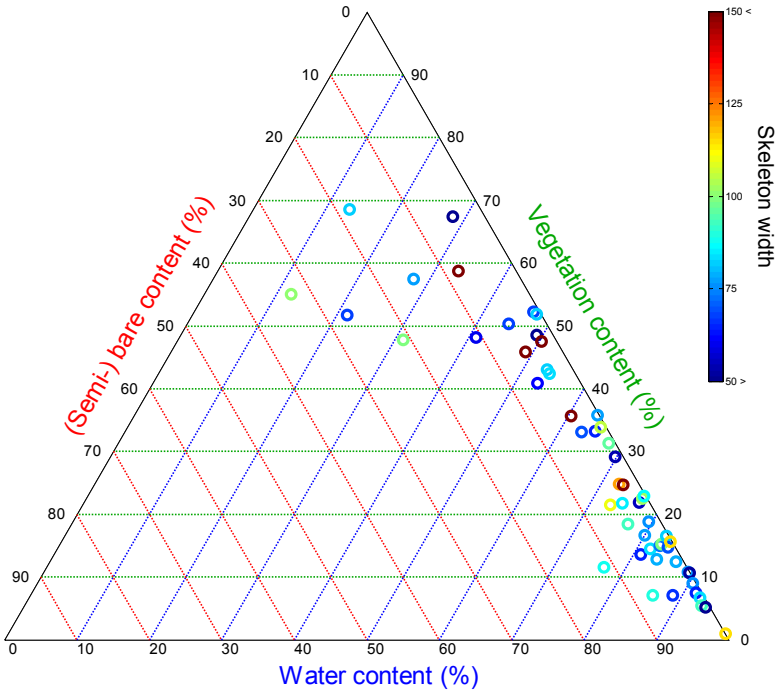

Figure 72: Ternary plot of channel line attributes that result from aggregating the attributes of the intersecting objects. On the axes the water, vegetation and (semi-) bare attributes of the lines are the plotted, the arrows show the corresponding axis directions. The colourmap denotes the skeleton width, cut-off at 50 and 150 m.

5.3.4 Smoothed channel lines

Figure 74 shows a subset of the results of the smoothing of the channel lines (§ 4.5.2). The smoothing significantly alters the channel lines and at some occasions creates curving bends where there are none in the real channel, e.g. in the middle right and lower left of the figure. The benefits are apparent as well, as the abundant small curvature changes are effectively removed. This is especially the case for larger channels, as their curves are from a relatively much larger scale than the curvature artefacts present in the skeletons. For smaller channels there is less difference with the artefacts. The benefits are clearly noticeable for the line of the Gorai, i.e. the centre channel in the subset.

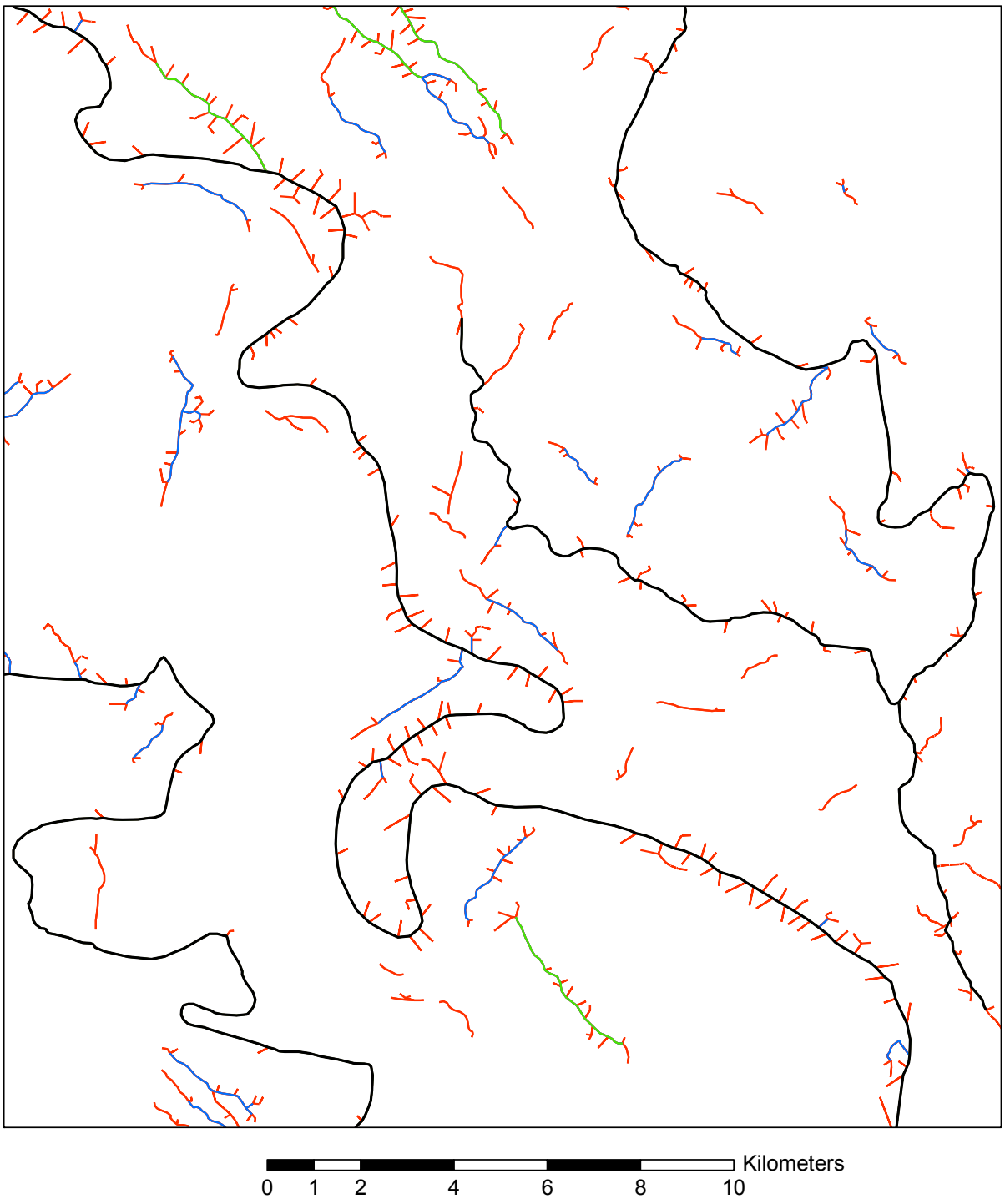

Figure 73: The stepwise removal of dangling skeleton lines and skeleton lines of small irrelevant channel parts. All lines together represent the complete object skeletons. The lines removed in the first step (dangles < 2000 m) are shown in red. The lines removed in the second removal step (dangles < 3000 m) are shown in blue. The lines removed in the third removal step (dangles < 6000 m) are shown in green. The lines that remain after all steps, i.e. the channel centerlines, are shown in black.

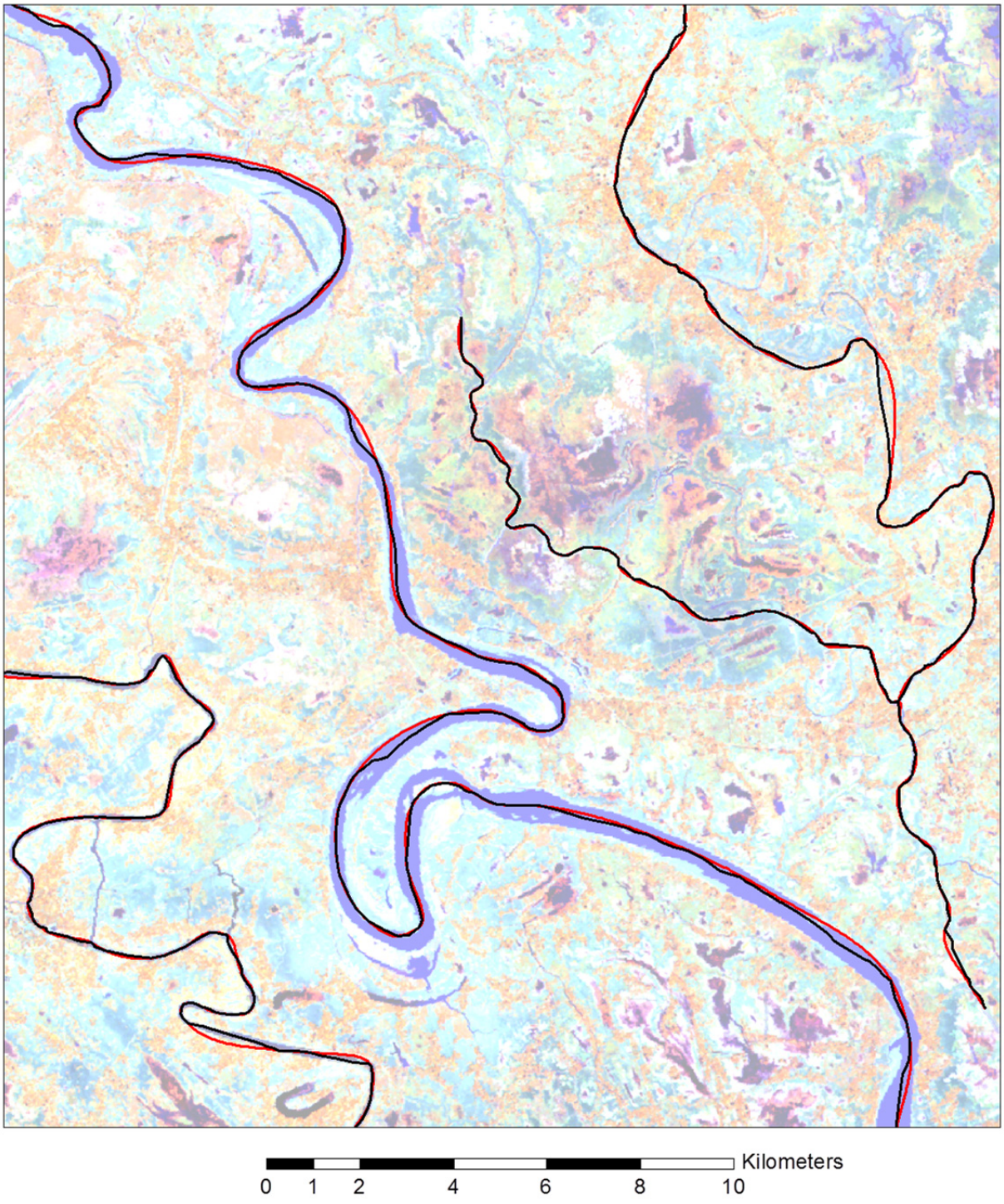

Figure 74: Subset of the Landsat image overlain with the unsmoothed (black) and the smoothed lines (red).

5.4 River geometry analysis

5.4.1 Determined inflection points

The used method to determine inflection points (§ 4.6.4) is able to determine all inflections of the meander accurately. As is shown in figure 75 the inflection points are placed at the position of lowest curvature at a direction change of the meander bend. For the total of 60 river lines that resulted from the skeleton processing, a total number of 1365 inflection points are determined.

The calculation of the spline (§ 4.6.6) is not performed for 4 meanders, as they have less than 6 inflection points. For another 11 meanders the spline is removed as the channel lines were manually determined to have no larger scale meander bends present. This means that for 45 rivers the splines as well as the second order inflection points (fig. 76) are determined. The calculation of the second order inflection points is similarly accurate to that of the first order inflection points. A map with the meander lines, inflection points, splines and second order inflections is enclosed as appendix A5.

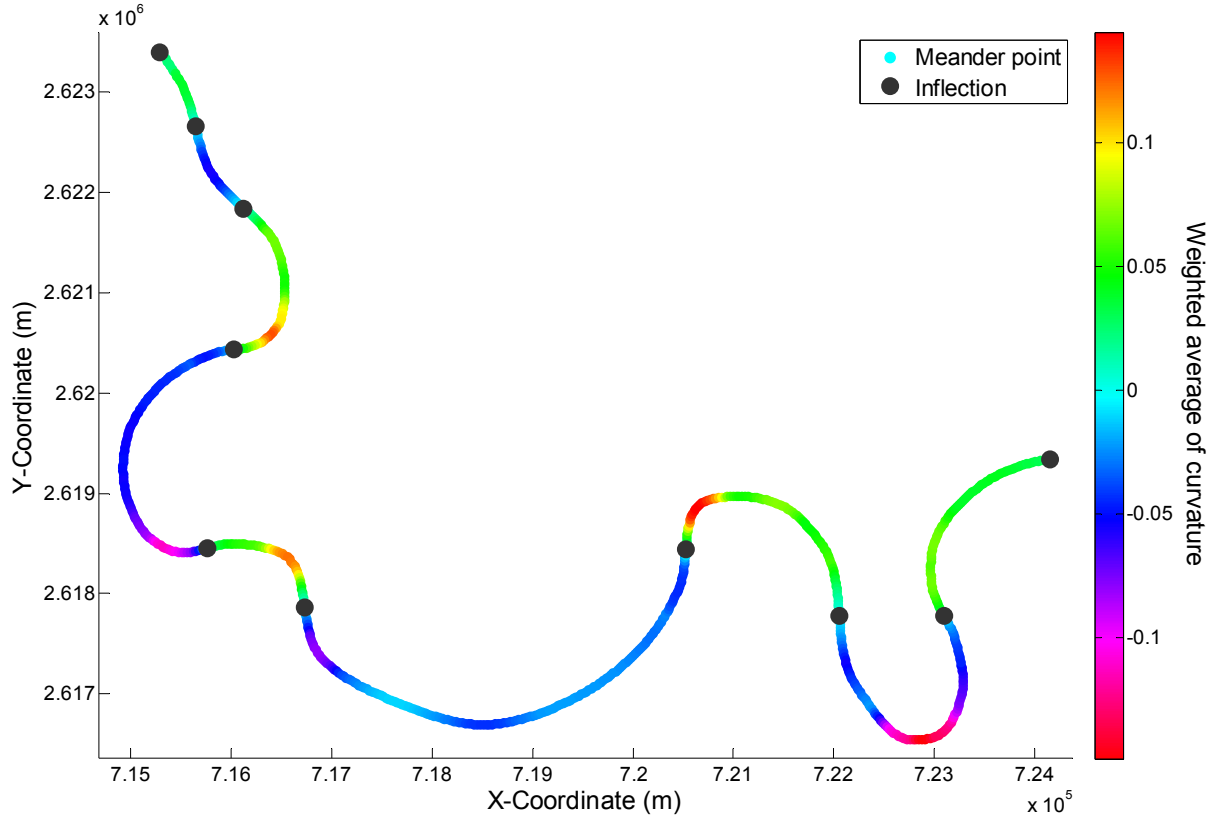

Figure 75: Subset showing the regridded points of a meander (ID=37) and the determined inflection points. The colourmap denotes the averaged curvature (§ 4.6.3) at each point.

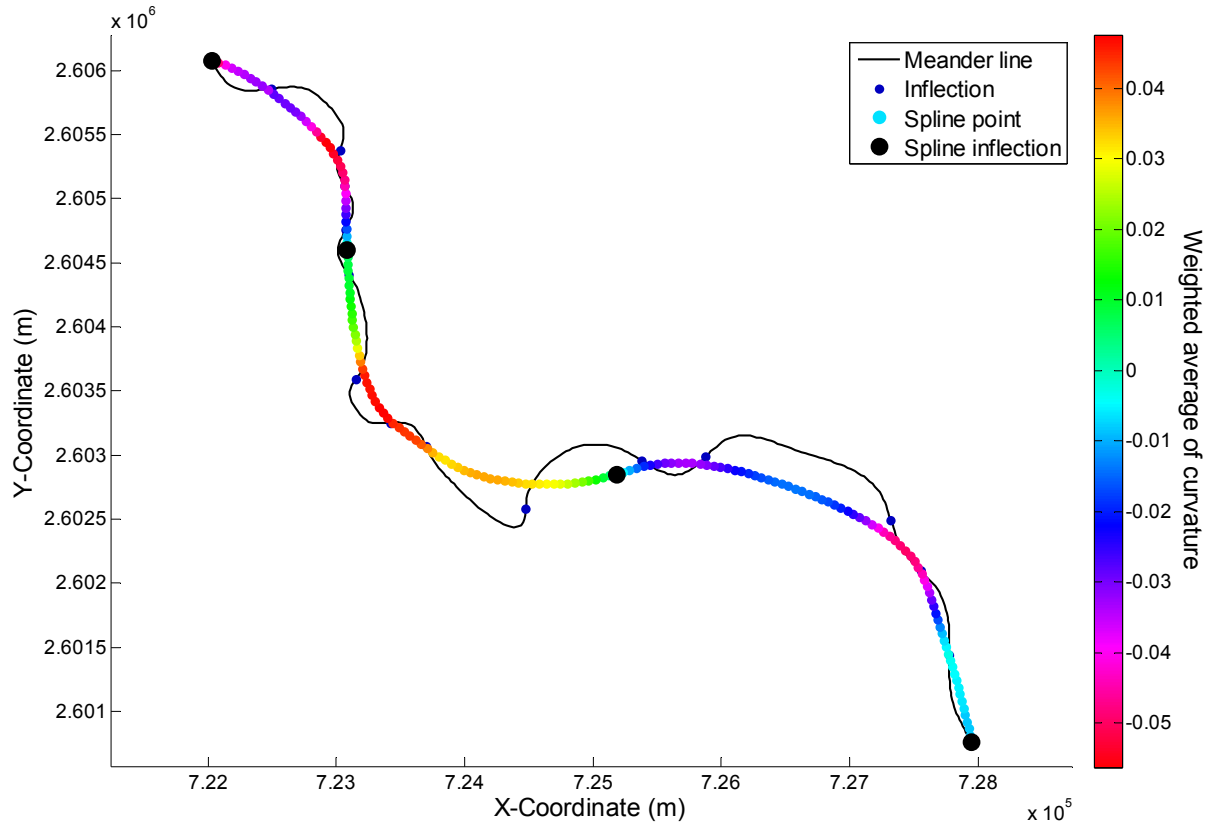

Figure 76: Subset showing a meander (ID=36), its inflections, the determined spline and second order inflections (*sp*=500 and *ip*=1). The colourmap denotes the averaged curvature (§ 4.6.3) of the spline at each spline point.

5.4.2 Determined meander wavelengths

The distribution of wavelengths for all the meanders that is calculated using two times the median inflection interspacing (§ 4.6.5) is shown in the histogram of figure 77. The overall wavelength minimum, first quartile, median, mean, third quartile and maximum are resp. 596, 1187, 1574, 1734, 1931 and 5343 m.

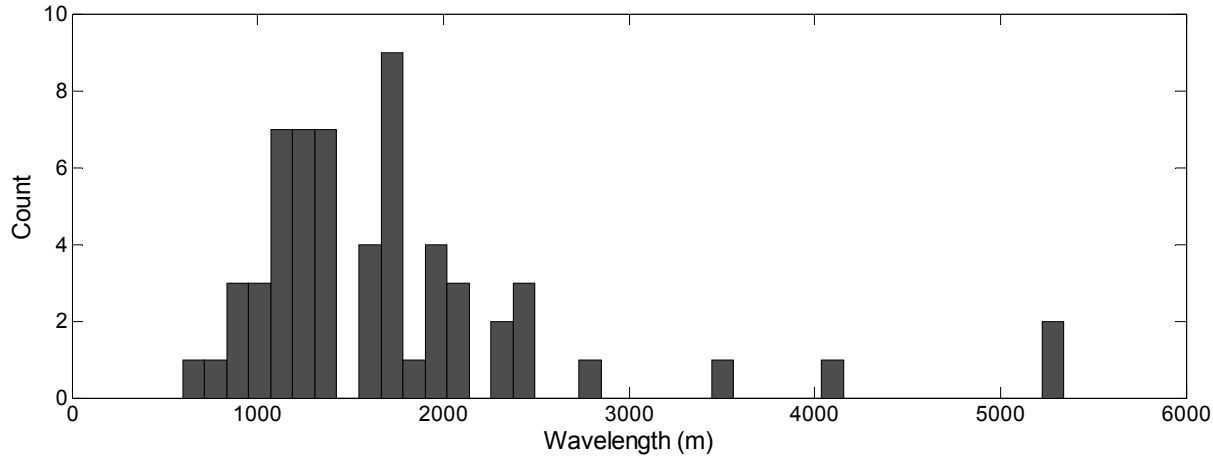

Figure 77: Histogram of the first order wavelength for all meanders. Wavelengths are based on the average inflection interspacing per meander.

5.4.3 Calculated discharges

A data overview of the results is presented in table 7. Spreadsheet data is enclosed as appendix C. For comparison with the channel lines a map with the channels and their corresponding IDs is presented (fig. 82) that is also enclosed as appendix A6.

The first order discharges that are calculated using the wavelength that is based on the median inflection point interspacing are shown in the histogram of figure 78. The discharge distribution is heavily skewed with a right hand tail, something already expected as there are many more small rivers in the area than larger ones. The calculated discharges range from 74 to 6537 m^3/s, with a first quartile, median, mean and third quartile of resp. 303, 539, 849 and 818 m^3/s.

5.4.4 Calculated discharges for the larger meander scales

The second order discharge calculations (fig. 80) result in significantly larger discharges than the first order ones. They range from 2082 to 133240 m^3/s and the first and third quartiles are 3841 and 12456 m^3/s. The minimum and quartiles are in a realistic range for medium to large rivers, e.g. compared to the value for the Ganges that has a bankfull discharge of ca. 75000 m^3/s (Jian et al., 2009). The maximum value, belonging to the Gorai, is unrealistic as it is comparable with nearly twice the bankfull discharge of the Ganges. The calculated second order discharge for the Hooghly is 85221 m^3/s.

5.4.5 Calculated sinuosities

The sinuosity calculations (fig. 79) that are based on the first order inflection point interspacings show a slightly skewed right hand tail distribution. Furthermore, the distribution seems multimodal. It is however impossible to determine this accurately, even with a smaller histogram bin size, as the population size is too limited. The range in sinuosities is 1.06 to 2.01, which is realistic. The bulk of the analysed rivers have a sinuosity in between 1.15 and 1.45, i.e. the first and third quartiles.

The sinuosities calculated using the splines to approximate the channel belt centerline are shown in the histogram of figure 81. Their distribution is spread more than that the first sinuosity approximations and they are generally a bit higher, as the range is 1.13 to 2.25 and the quartiles are 1.22 and 1.60. The apparent multimodal distribution of the other sinuosities is not distinctly present for the spline-based sinuosities.

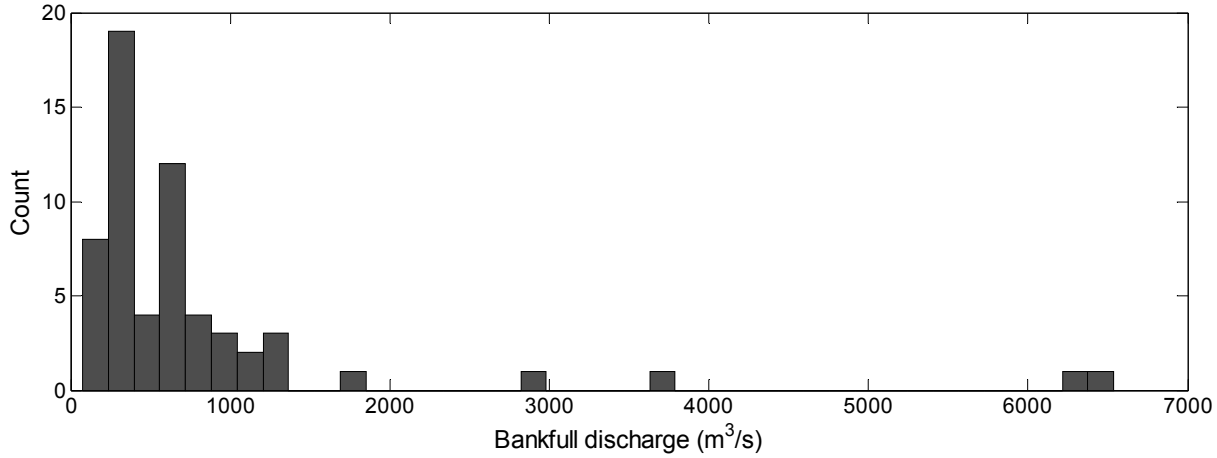

Figure 78: Histogram of the first order discharge results for all meanders, based on the median inflection interspacing.

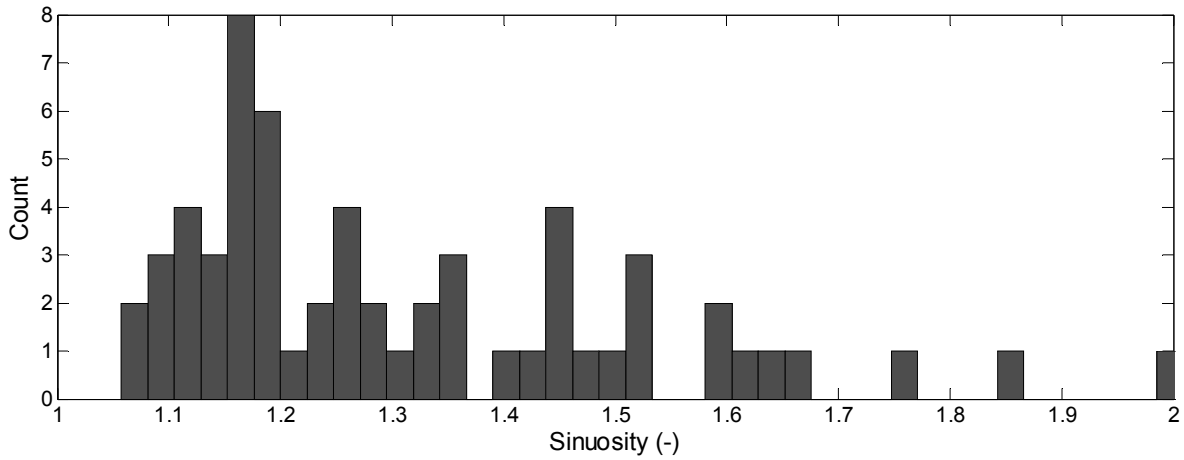

Figure 79: Histogram of the first order sinuosity results for all meanders.

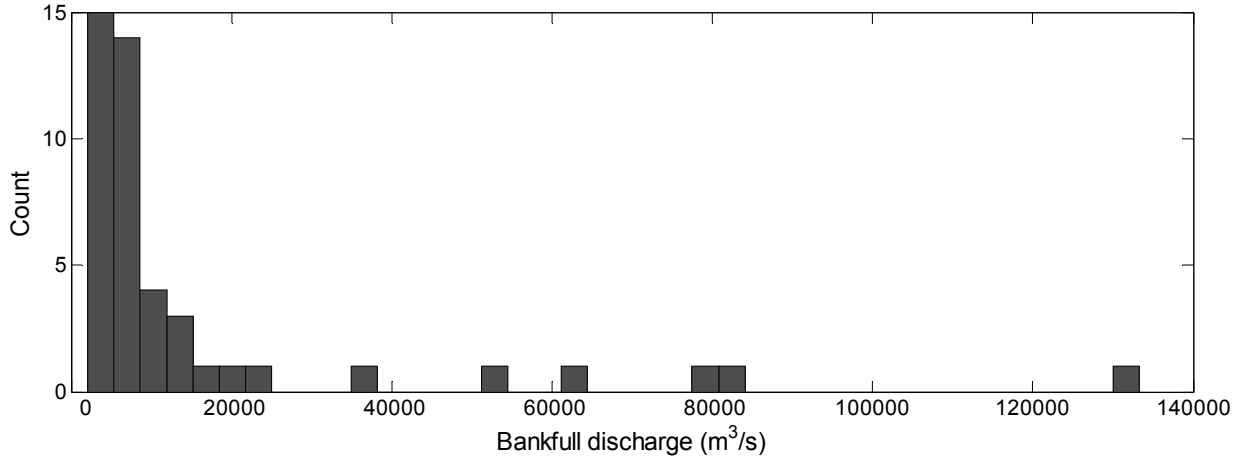

Figure 80: Histogram of the second order discharge results for all meanders, based on the mean inflection interspacing.

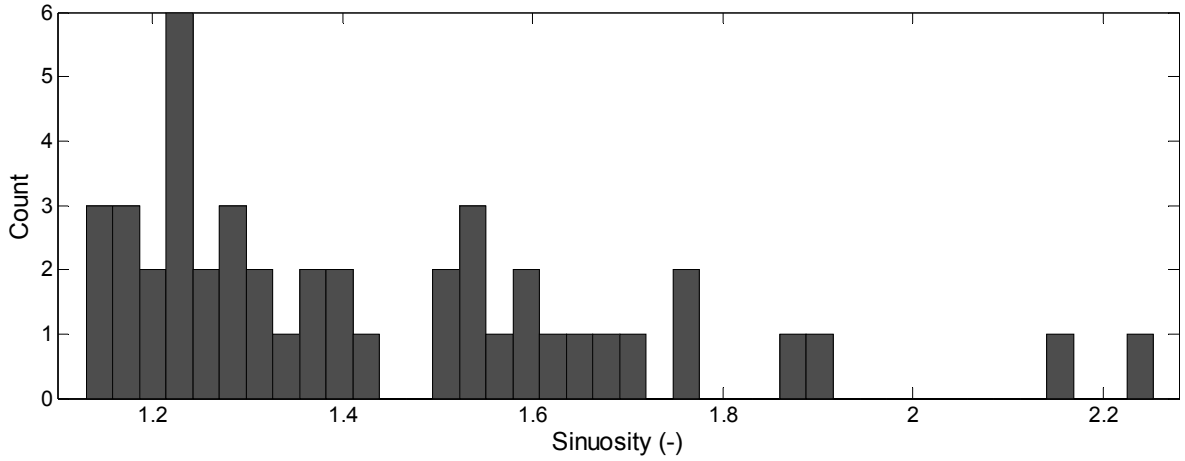

Figure 81: Histogram of the spline based sinuosities for all meanders.

General properties/results								1st order discharge statistics (m^3/s)						2nd order analysis					
ID	Length (m)	Water %	Vegetation %	Bare %	Skeleton width (m)	Inflections	Sinuosity	Min	Q1	Median	Mean	Q3	Max	Inflections	Discharge (m^3/s)	Sinuosity	SP	IP	End points
1	9083	83	13	4	100	15	1,12	64	161	233	289	420	1259	3	6475	1,13	300	2,0	False
2	16360	90	9	0	68	14	1,32	131	332	904	801	1170	3907	4	9511	1,37	300	0,5	False
3	5945	99	1	0	82	11	1,11	41	129	194	247	400	800	-	-	-	-	-	-
4	11516	13	68	18	-	14	1,19	93	159	390	484	905	1943	2	78928	1,27	300	0,5	True
5	33959	56	42	2	99	22	1,50	24	454	662	1026	1352	7419	5	11767	1,67	600	2,0	False
6	4811	81	14	5	77	7	1,14	97	97	391	432	534	1823	-	-	-	-	-	-
7	6245	44	50	5	0	4	1,10	283	771	3731	3228	7242	8674	-	-	-	-	-	-
8	6537	33	59	8	286	11	1,06	29	116	279	330	517	1234	-	-	-	-	-	-
9	12192	83	16	0	60	12	1,16	232	397	685	800	1308	2320	-	-	-	-	-	-
10	33893	73	21	6	68	39	1,17	37	127	290	506	1009	4927	9	5737	1,22	500	1,0	False
11	95607	77	12	11	359	24	1,37	144	3500	6537	8536	14830	42541	6	133240	1,50	1500	2,0	True
12	40128	77	18	5	68	29	1,52	47	423	826	776	1193	2694	9	3915	1,71	500	2,0	True
13	19898	83	15	2	81	19	1,46	25	180	416	496	599	5016	6	3029	1,60	500	2,0	True
14	12309	47	52	1	44	11	1,15	95	244	812	1003	2136	4092	-	-	-	-	-	-
15	9764	28	67	4	62	16	1,15	65	140	156	274	256	3688	-	-	-	-	-	-
16	9223	21	51	27	-	12	1,10	22	82	318	501	1398	2464	3	11217	1,16	500	0,3	False
17	14482	27	46	27	175	15	1,06	115	150	389	840	553	11901	-	-	-	-	-	-
18	78377	89	11	0	82	65	1,29	122	264	553	790	1093	12451	16	9274	1,36	500	2,0	False
19	11181	41	48	11	84	22	1,24	15	50	74	158	181	1270	-	-	-	-	-	-
20	7218	56	41	2	-	8	1,36	61	107	278	499	972	2209	-	-	-	-	-	-
21	7118	28	57	15	-	15	1,12	35	105	132	175	200	869	3	6303	1,15	500	0,2	False
22	6618	53	41	6	311	6	1,19	233	336	678	1092	2660	2954	-	-	-	-	-	-
23	41582	93	5	1	70	26	1,52	245	635	925	1058	1527	3184	6	16604	1,66	1000	2,5	True
24	8231	76	23	0	65	7	1,62	139	166	344	626	1892	2052	-	-	-	-	-	-
25	8762	52	43	4	77	11	1,22	55	125	187	447	467	4137	3	4064	1,30	300	0,5	False
26	40780	84	16	0	106	24	1,28	87	719	1174	1716	3283	9553	5	8424	1,40	700	1,5	True
27	8963	60	35	4	89	6	1,84	205	271	960	830	1670	1681	-	-	-	-	-	-
28	9539	92	7	1	97	6	1,66	732	815	1363	1174	1528	1547	-	-	-	-	-	-
29	8610	0	0	0	-	9	1,51	70	106	526	440	872	1172	4	2201	1,76	50	0,3	False

Table 7: Overview of the results from the geometry analysis per channel line. Table continues on next page.

ID	Length (m)	Water %	Vegetation %	Bare %	Skeleton width (m)	Inflections	Sinuosity	Min	Q1	Median	Mean	Q3	Max	Inflections	Discharge (m^3/s)	Sinuosity	SP	IP	End points
30	6050	94	5	1	110	9	1,19	190	197	301	351	453	947	3	3376	1,22	1	0,8	False
31	16596	65	33	2	54	8	1,76	368	922	1304	1613	2891	3697	3	2627	2,15	500	1,0	False
32	9824	31	48	21	121	11	1,19	121	224	620	599	1143	1777	3	13910	1,21	50	1,5	False
33	15441	54	42	4	85	10	1,45	319	465	583	1235	1371	9582	3	8524	1,63	500	1,0	False
34	120160	86	7	7	312	24	1,60	1959	4069	6319	9859	19957	57169	7	83126	1,77	300	2,0	True
35	12086	67	31	1	93	17	1,17	69	133	270	360	705	1020	7	2306	1,22	250	0,2	True
36	10867	49	46	5	55	16	1,14	66	115	228	351	551	2084	4	6524	1,18	500	1,0	False
37	21320	74	22	4	64	10	1,45	586	919	1777	2408	3298	13692	6	5840	1,55	250	1,0	True
38	7522	77	22	1	103	8	1,09	144	326	696	855	1588	3528	-	-	-	-	-	-
39	19607	50	47	2	87	20	1,44	46	157	371	447	681	1925	8	2395	1,58	400	1,0	True
40	30256	83	15	2	77	38	1,22	61	210	289	386	455	3572	12	3622	1,26	50	2,4	True
41	28103	65	34	1	76	33	1,16	42	148	366	499	844	3903	9	5898	1,21	400	2,0	True
42	29059	89	11	0	84	31	1,27	65	177	315	510	485	4059	11	3286	1,33	250	1,8	True
43	32847	49	48	2	90	19	1,16	74	281	1151	2237	5384	18442	8	12165	1,23	100	2,0	True
44	51811	70	27	3	79	41	1,34	20	342	626	817	1430	5503	12	7639	1,41	500	3,0	True
45	11478	12	55	33	72	14	1,20	90	180	432	471	765	1874	5	4218	1,23	300	0,9	True
46	27624	76	22	1	100	10	2,01	211	350	1294	2090	5023	10356	4	8014	2,25	500	1,0	False
47	67146	79	19	2	82	46	1,40	29	370	825	1005	1570	9418	14	6350	1,53	300	2,0	False
48	46232	80	17	3	69	36	1,45	101	441	691	726	1162	2541	8	6959	1,60	400	2,0	False
49	99429	86	12	1	115	76	1,18	64	392	799	1107	1812	18731	17	13330	1,25	400	2,5	False
50	19215	64	36	0	66	18	1,26	125	176	597	711	1505	2582	8	2836	1,29	50	4,0	True
51	12230	91	7	1	79	14	1,27	71	229	385	478	863	1605	7	2083	1,30	100	1,5	True
52	17236	84	15	1	76	29	1,15	23	95	183	245	324	2003	6	6547	1,18	750	2,5	True
53	29803	70	29	1	52	37	1,33	68	199	306	334	442	1330	13	2445	1,39	300	2,0	True
54	38262	72	25	3	76	42	1,44	58	196	290	365	521	2651	9	6257	1,51	400	2,0	True
55	23390	47	52	1	64	30	1,11	94	144	346	455	821	2488	4	36756	1,13	300	8,0	False
56	68723	82	14	4	83	54	1,34	46	310	666	819	1304	5751	4	52072	1,54	2000	8,0	True
57	37861	53	43	4	92	31	1,15	152	335	690	1056	1953	7123	5	21023	1,22	1000	4,0	True
58	32610	73	25	2	48	29	1,63	49	230	353	442	490	3673	7	4033	1,88	500	3,0	True
59	113490	88	7	4	114	35	1,60	244	1775	2856	3969	7098	21662	10	22076	1,89	750	3,5	True
60	88234	63	33	4	86	68	1,25	108	304	623	980	981	33808	6	61705	1,35	1200	11,0	True

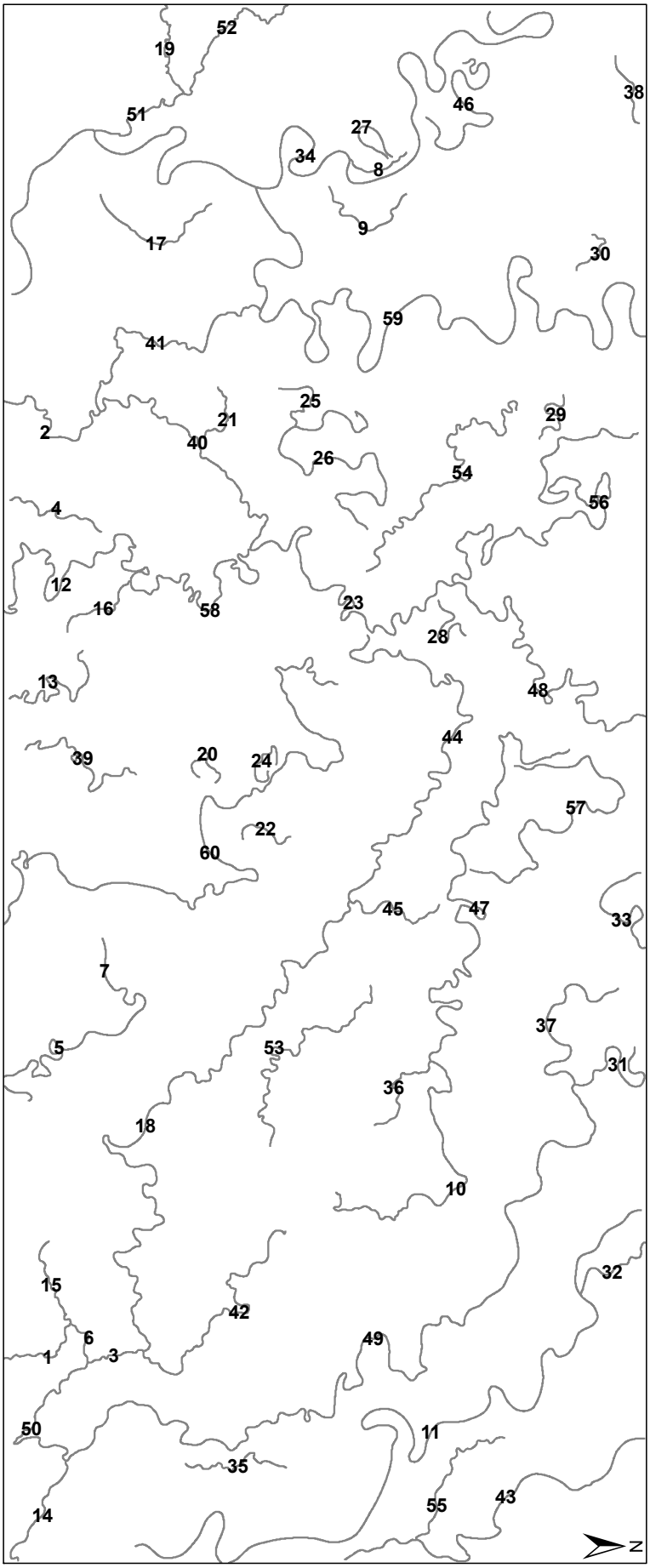

Figure 82: The channel lines labelled with their corresponding IDs. Note that the map is rotated 90 degrees clockwise.

6. DISCUSSION

6.1 Accomplishments of the study

The method to delineate meander objects in satellite imagery, assessed by Addink & Kleinhans (2008) and Kraaijenbrink (2010), has already proven to be a great improvement over traditional pixel-based classification methods as true meanders, both active and fossil, could be classified. Major issues were present however with channel continuity that hampered further analysis of the channel objects, i.e. only many small individual meander objects could be obtained.

By a refinement of the meander delineation method, by a merge of the objects from the different segmentation scales and by the extraction of channel centerlines, the method presented this study has yielded significant improvements. Namely, with the developed method an extensive network of channels in a study area can be derived from satellite imagery nearly automatically, which was previously not possible without manual digitization. Furthermore, the quality of the extracted data is at a level at which it can be used to analyse the geometry of the meandering channels in the network to determine river characteristics such a discharge and sinuosity.

6.2 Comments on the developed method

6.2.1 Complications of data reduction into a single object set

The combining of segmentation levels (§ 4.3) that is used in this study is relatively simple, i.e. the objects from the different scales are merely merged. In this process there are many locations where, for a given channel, an object of a relatively small segmentation scale is overlaid with an object from a larger scale. As a result, applying merge processes causes the larger scale to be preserved and the smaller scale to be lost. As the larger scale objects generally contain more pollution and are less accurate representations of the actual channel, the skeletons as well as all the attributes of the merged objects are less accurate as well. This is of course not what is preferred as it decreases the accuracy of the channel analysis.

Other approaches for merging the scales were already proposed in prior research (Kraaijenbrink, 2010). It mainly consisted of developing an algorithm that determines which object is used in the merge at a given channel part. This solution has been explored in this study. However, a correct and accurate algorithm is not found because numerous difficulties emerged. An example of such a difficulty is given in the next paragraph. To overcome the difficulties the algorithm has to become complex, in a way that is beyond the scope of this

study. Dedicated research though is likely to be able to improve the merging of the scales significantly.

It is often the case that a small scale object misses a tiny part of the channel, i.e. only several pixels in length, and that these pixels are present in an overlaid object from a larger scale. The ideal situation in this case would be that the least polluted small scale object is retained as well as the channel part that is missing, extracted from the larger scale object. However, while it is already difficult to determine if an object misses a channel part algorithmically, it is presumably impossible to determine which pixels of the larger scale object make up the missing channel pixels.

6.2.2 Complications of gap removal

A more daunting task appears subsequent to the merging of the different segmentation scales as the various mentioned error types (§ 4.4) are abundant. Fixing the channel discontinuity that is due to presence of diagonally bordering pixels is simple with the border growth process. There are however two negative side effects to this process. Firstly, channels that are two or less pixels near each other are also unintentionally merged. Secondly, as the objects are widened, the centerline of the objects' skeletons is slightly altered, especially in sharp bends where the line is drawn towards the inner bend. Both side effects are however not that severe that they outweigh the benefits of the appliance of the border growth process.

Several assessed methods to remove the larger gaps in the network algorithmically were unsuccessful. Again, an improvement may be made if a dedicated, comprehensive research is performed to develop a proper algorithm. Although suggested by Kraaijenbrink (2010) to use the endpoint direction of classified objects to narrow the search for neighbouring unclassified channel parts, this is not explored in this study. It should be possible to implement such classifying rules that may work in combination with thresholds on object attributes.

6.2.3 Usage of manual object addition

It is the question whether improving the meander classification algorithm is worth it. It is likely that there will always be channel objects that cannot be classified automatically. The majority of unclassified meander objects do not have attributes that can properly distinguish them from non-meander objects, as determined in the attribute analysis of the manually added objects. Manual editing of the classification remains inevitable if to obtain a channel network without discontinuities.

Manual and subjective actions are required to clean the object set from skeleton looping at meander cut-offs. It is very difficult to impossible do this algorithmically, as it requires extensive analysis of the local polygon and the possible paths along the river to determine potential cut locations.

In general it must be considered whether the manual editing that is required in the developed method outweighs a manual digitization of the channels line in terms of quality and required time. Based on own experience, the quality of the channel lines is better when manual digitization is performed. Line smoothing is not required if arcs are used in the digitization and channel gaps are not present. Furthermore, a human view on the image will yield a complete network coverage that is designed for the specific needs of the study. In terms of required time, it depends on the size of the input data. The larger the area, the more time it will cost to digitize the meanders manually in comparison with the method presented in this study.

The major downside to manual digitization is that true subjectivity is involved and resulting channel networks will differ every time and per individual, i.e. the precision is low. The precision cannot be improved as it is practically impossible to define a standard on how to draw lines. The low precision of manual digitization will greatly hamper a widespread use of the method as a standard to obtain discharge distributions. Though the method that is presented in this study requires a certain extent of subjectivity as well, it is of another scope as merely computer-generated objects are selected. Furthermore, it is possible to completely diminish it by defining clear rules that standardize how individuals should handle network gaps and skeleton looping. It can then be used as a true standard for the obtainment of relative discharge dynamics of an area, with minimized variability in the accuracy among different studies.

6.2.4 Insight in the river geometry analysis

The river geometry analysis performed in this study (§ 4.6) is thought to be the most feasible method to analyse the geometry of the extracted channels using empirical relations. The other known relations that use the channel width or the radius of curvature are more difficult to use. Prior research of Kraaijenbrink (2010) has shown that using the object width as an indicator for channel width is inaccurate and does not yield realistic results. Using the radius of curvature is a possibility that is not yet explored, however the algorithmic implementation is thought to be more difficult and the accuracy of the empirical relation is not significantly better than that of relation that uses the wavelength (Bridge, 2003).

Still, the empirical relation used has a significant uncertainty in the accuracy of about a factor 2 to 3, due to differences in the geology and geography present at different rivers (Bridge, 2003). However, the substrate and yearly discharge fluctuations of all rivers systems in the study area are relatively similar (Sarkar et al., 2009), which should diminish the scatter around the empirical relation. Concluding, the calculated discharge cannot be firmly trusted to be correct before a calibration is performed, but the relative discharges are thought to be reliable.

The analysis of the larger meandering scales of rivers in the study area is more difficult to evaluate on its accuracy. On top of the error that is related to the empirical relation, subjectivity in the setting of the smoothing parameter is required. Furthermore, it is not certain if a larger scale is indeed present, or that it is just caused by local topography. Finally, the calculated spline depends on the locations of the first order inflections and these are not undoubtedly the best indicators of the general course of the channel as they heavily depend on the local bend planform.

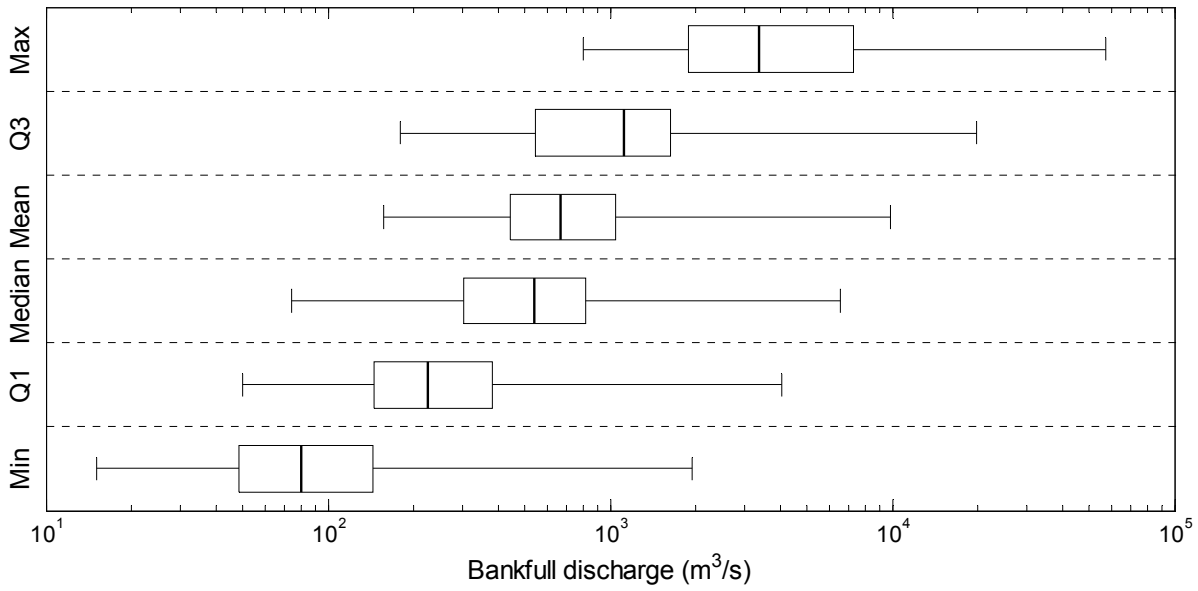

Figure 83: Boxplots showing six distributions of bankfull discharges for all meanders. The discharges in the distributions are calculated using different inflection interspacing statistics that are denoted on the y-axis.

As stated in the methodology section, various inflection interspacing statistics are used to calculate discharge. The overall distributions of the first order discharges that result from the various statistics are shown in figure 83. This approach followed from the findings in the literature review. Namely, it was found to be unclear which statistic is best to use to describe meandering rivers if numerous bends per river are sampled or, such as in this case, practically all bends are sampled. This lack of clarity caused inconsistency in the results of different studies due to the potentially large differences in the presented values; the latter is

shown evidently in figure 83. Thus, to improve comparability of this study, different statistics are calculated. However, the discharges that are used in this study for evaluation of the analysis results are those that are based on the median inflection interspacing.

The supporting idea about using the median is that it is less susceptible to outliers than the mean (Davis, 2002). Those outliers are thought to be non-representative for the overall geometry of the channels that resulted from a certain channel forming discharge. It is likely that where the outlier wavelengths are located other external effects play a role, e.g. a difference in substrate or anthropogenic influences. In case of the second order analysis the mean is used instead of the median. This is done because for the second order analysis only a limited number of inflections are available, with little spread in the wavelength distribution per river. In that case the mean in a more reliable statistic (Davis, 2002).

6.2.5 Severity and consequences of the overall error

It is difficult to determine the overall error that is related with the method of this study. There are many different steps and assumptions involved that can all have influences on the outcome and their errors may add up or diminish each other. An error analysis is not performed in the research mainly because of this high number of potential sources of error and the significant extra workload it would therefore require. Furthermore, many of the variables have errors that are very difficult to determine, e.g. the skeleton accuracy, effects of smoothing, and the quality of training set sampling.

Although the potential of errors is clearly present, the results are satisfying when considering the intention was to obtain a relative discharge distribution in the study area. Many of the potential sources of errors will result in an equal amount of error for each meander, and therefore have no effect on relative aspects. If one wants to determine the overall error, the best way is by comparing the results of each river with ground truth. This is however a difficult task as data on the rivers in the study area is sparse and strictly controlled by the local governments. If obtained though, the error information can be used to calibrate the method. The calibration will only be valid for this study area, as significant changes in geographic boundary condition cause changes in parameters of the empirical relation.

6.3 Value of the determined river characteristics

6.3.1 Accuracy of the calculated discharges

The discharges that are found using the mean inflection point interspacing are in a realistic range. They seem to be relatively accurate as well, taken into account the many

potential sources of error and the factor 2 to 3 accuracy of the used empirical relation. The accuracy is however difficult to state with strong confidence due to the sparse ground truth.

Supporting data is provided by Sarker (2005), in the figure that presents the mean daily discharges of the Gorai (fig. 19). For the measured pre-Farakka period of 10 years, the annual maximum of mean daily discharges is ca. 5500 m^3/s. As already mentioned, the bankfull discharge roughly equals a discharge with a recurrence period of 1.5 to 2 years. Because the data provided by Sarker is a 10 year average, the bankfull discharge likely is among the higher range of values of which the average is calculated and thus is slightly higher than 5500 m^3/s, e.g. ca. 6000 m^3/s. Compared with the calculated bankfull discharge of 6537 m^3/s, the difference is therefore must be less than a factor 1.18, i.e. 6537/5500.

Another indication for the accuracy of the discharge results can be deduced from the ratio between the bankfull discharge and the mean annual discharge. Data of the latter is available for the Hooghly, Gorai and Ganges rivers. Although generally the ratio differs from river to river due to differences in local geographic characteristics, these three rivers have a shared catchment and therefore have the same precipitation regime and discharge variability. To a certain extent the substrates are similar as well and it is therefore assumed to be valid to compare them this way for indicating purposes. The Hooghly and Gorai rivers have a calculated bankfull discharge of resp. 6319 and 6537 m^3/s and both an annual mean discharge of ca. 1200 m^3/s (Mirza, 2004), i.e. $Q_{bf}/Q_{ma} \approx$ 5.4. The Ganges has a bankfull discharge of ca. 75000 m^3/s and a annual mean discharge of ca. 12500 m^3/s (Jian et al., 2009), i.e. $Q_{bf}/Q_{ma} \approx 5.6$. Thus, the ratio resulting from the calculated discharges of the Hooghly and Gorai is very similar to the ground truth ratio of the Ganges, indicating a high accuracy of the discharge calculations.

Using the available data, a tentative conclusion is made that the calculated discharges are an overestimation of around 15%. As no discharge data can be obtained for other rivers in the study area, further comparisons cannot be made and a true confirmation and confidence remains absent. Especially the absence of data for the smaller rivers renders their accuracy indistinct. It is expected that the very small channels have larger deviations, as they tend to have more pollution by riparian pixels. This means that they have significantly larger scaled skeleton errors while they are much smaller scaled themselves. Driven by the same line of thought, the skeleton error for medium sized rivers is expected to be of less influence, hence the accuracy of the results to approach the estimated 15%.

6.3.2 Evaluation of the discharge continuity

The meander lines used in this study predominantly represent channel sections in between bifurcation and confluence nodes. Although few actual nodes exist due to the presence of gaps, the calculated discharges can be evaluated on their continuity. Some channel parts seem to match to their tributaries and distributaries reasonably well, while most are completely off. Two good results as well as a bad one are shown in figure 84. The three small channel sections in the far left as well as the three larger sections in the middle of the figure have a clear change in wavelength after the confluence, and this is also reflected in the discharge calculations. Namely, after the confluences the continuing channels show absolute differences with the sum of the upstream branches of resp. 57 (12%) and 84 m^3/s (10.5%). In the far right of the image the discharge topology is however completely wrong, as a channel with a mere 422 m^3/s splits in two channels with a combined discharge of 1277 m^3/s, a more than 300% difference.

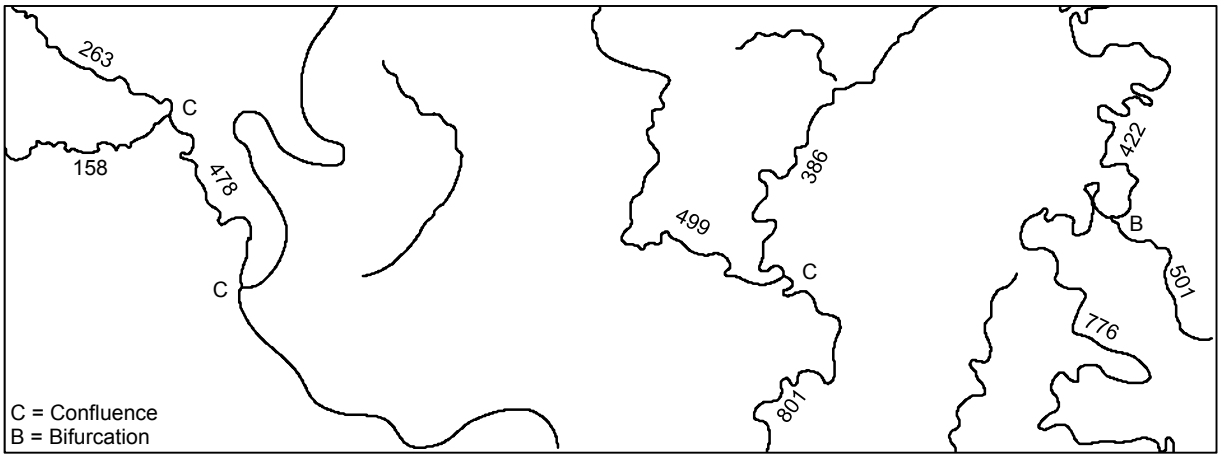

Figure 84: Subset of meander lines labelled with their calculated first order discharges (m^3/s). Flow direction of the channels is either from west to east or from north to south.

A quick evaluation of the percentage differences in discharge at the gross of the nodes indicate that half of the nodes have a difference between up- and downstream discharges of more than 63% and three quarters of the nodes have a difference of more than 14%. Causes for this inaccuracy may lie at a wide range of sources. It could be that it there is an avulsion or late stage bifurcation present. In that case one of the downstream branches must be (partly) left out of the equation. Avulsions are not likely as all large branches in the river analysis seem to have a water flow, but late stage bifurcations are a possibility.

It can also be that some branches just contain too little inflection points for an accurate wavelength calculation. Maybe only a part of a river located in a relatively harder substrate is classified, causing the used empirical relation to be invalid. There may be channel branches

that are not classified with the used methods causing fluxes of water that are unknown. The latter would cause the calculations for certain present channels to be wrong as well, as they should have been split at a certain location, likely changing the calculated mean meander wavelength.

Besides the possibility of avulsions or late stage bifurcations, the causes for the errors could be overcome by further improvements of the channel network. In the latter case, the low accuracy of the discharge continuity compared to the apparent accuracy of the sole channels leads to the hypothesis that is the calculated discharges are not accurate and that as a result the relative distribution of discharges is incorrect. It is however difficult to determine if this hypothesis is correct. It is presumably not true, as the relatively similar boundary conditions are thought to result in much less spread than the continuity errors show. The effect of late stage bifurcations is therefore a more likely cause.

6.3.3 Accuracy and value of the determined sinuosities

Sinuosity is an important description of the meandering nature of a river, it is however more a side product of this study than the main focus. It cannot be used to determine river dynamics and is therefore not a significant contribution to further research on bifurcations, avulsions, changing discharge regimes and channel network evolution.

Like the presented discharge results, the sinuosities obtained by this study are difficult to validate. The only data found in literature is for the upper reach of the Gorai, from the off-take to the Karmarkhali bend. The latter is the late stage bend of the Gorai shown in lower middle of the subsets shown in fig. 73 and 74. In 1992 the sinuosity of that river section is reported to be 1.38 (Sarker, 2005). This is a ca. 1% difference with the calculated 1.37 of the first sinuosity approximation of the Gorai.

The spline-based sinuosity of the Gorai is 1.50, which is higher with a difference of 8.7%. Thus, although the spline based sinuosity is assumed to more accurately describe the sinuosity this is probably not the case. It is most likely caused by corner cutting of the spline of the channel belt bends. Overall, the higher accuracy of the sinuosities compared to the discharges can be easily explained. It does not rely on empirical relations and can directly be deduced from the geometry of the channels, removing a major source of error.

6.4 Insights in the evolution of the Ganges distributaries

The results of the second order analysis can be used to explore the discharges related to past discharge regimes that channels encountered. Great caution must however be used

in doing so as the larger meander scales that were analysed are not undoubtedly caused by meandering of larger channels. Other factors like geologic conditions could have forced them as well. Nevertheless it is likely that many of the local rivers encountered larger discharges in the past, as the Ganges flowed through the area at different locations.

Especially interesting is to evaluate the statements that are made in literature about the channels that are suggested to have been the Ganges main course. For this evaluation the calculated second order discharges of these channels are compared with the bankfull discharge of the present Ganges. An important note is that it is not certain that the Ganges encountered similar discharges in the past, but this is the only way to compare them discharge-wise. Furthermore, the inaccuracy of the empirical relation that is used makes the absolute discharges used here also uncertain. As relative discharges are more reliable and the Hooghly certainly was the Ganges main course (Goodbred Jr. & Kuehl, 2000), it is best to compare the other channels with the Hooghly.

The calculated first and second order discharges of the Hooghly, Jalangi, the upper and lower sections of the Bhairab and of the Gorai are shown in figure 85 together with the present Ganges discharge. The figure shows that second order discharge of the Hooghly and the two Bhairab sections are relatively close to the present Ganges discharge while the Jalangi and the Gorai are very different with resp. large negative and positive differences. Solely based on these results the hypothesis arises that the Hooghly and Bhairab once were the main Ganges while the Jalangi and Gorai were not. This hypothesis is supported by the fact that large scale oxbow lakes are present for the Hooghly and Bhairab while absent for the Jalangi and Gorai (fig. 15).

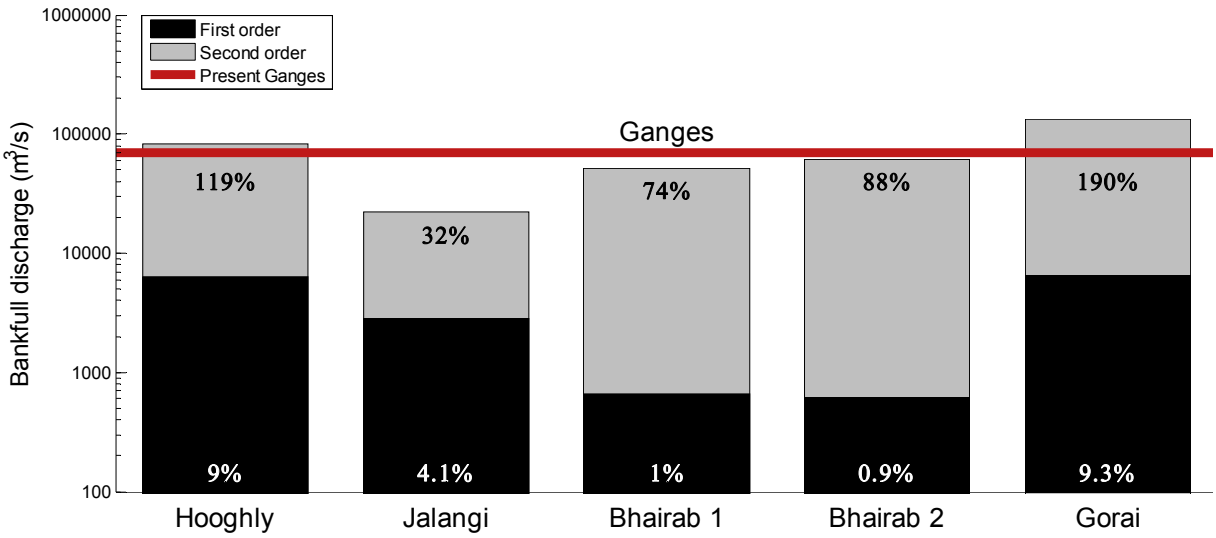

Figure 85: Comparison of the first and second order bankfull discharges with that of the present Ganges. The numbers that are shown per river and per discharge order denote the percentage of the Ganges discharge.

The two Bhairab sections have a lower second order discharge relative to the Hooghly, which shows that the larger scale geometry of the two rivers is significantly different. A hypothesis is that, in contrary to the Hooghly, the Bhairab was initially abandoned by the Ganges main course at a slow rate. This provided sufficient time for the Bhairab's geometry to adapt to the decrease in discharge. Then suddenly the speed of the discharge decrease increased and the geometry could no longer catch up to the discharge decrease. As result, a smaller meander scale was imposed onto the remaining larger scale bends, i.e. the situation at present (fig. 15 & 86f).

When adding the calculated the second order discharge of the Jalangi to that of the upper section of the Bhairab the resulting discharge is similar to that of the Hooghly and thus of the paleo-Ganges. This yields the idea that the hypothesized initial slow discharge decrease in the Bhairab course was caused by an upstream bifurcation that resulted in the Jalangi. As the bifurcation evolved slowly, a direct linear relation existed between the Bhairab and the Jalangi discharges. At some moment in time another bifurcation occurred more upstream than the Jalangi one. This new bifurcation developed faster and it quickly became the Ganges main course with the Bhairab and Jalangi as its distributaries.

The absence of oxbow lakes with a dimension similar to that of the larger scale meandering of the Jalangi can be explained by this idea as well. As the discharge continuously increased at a slow rate until the discharge suddenly dropped quickly, the largest discharges only occurred for a very short time span. This amount of time was probably not enough to form the oxbow lakes. The absence of abundant differently scaled oxbow lakes that were formed in the period between the beginning of the Jalangi and the sudden decrease in discharge is difficult to explain. Possibly the whole period of discharge increase was too short to form oxbow lakes, while it was enough to change the geometry of the Bhairab.

The larger scale meandering of the Gorai is not at all distinct, rendering the second order analysis not accurate. This makes it impossible to compare them with the other channels confidently. However it maintains the hypothesis that it was not the Ganges main course. Namely, if it was, the larger scale meandering is expected to be similarly present as for the other channels. The hypothesized evolution of the main distributaries is shown in the sketches of figure 86.

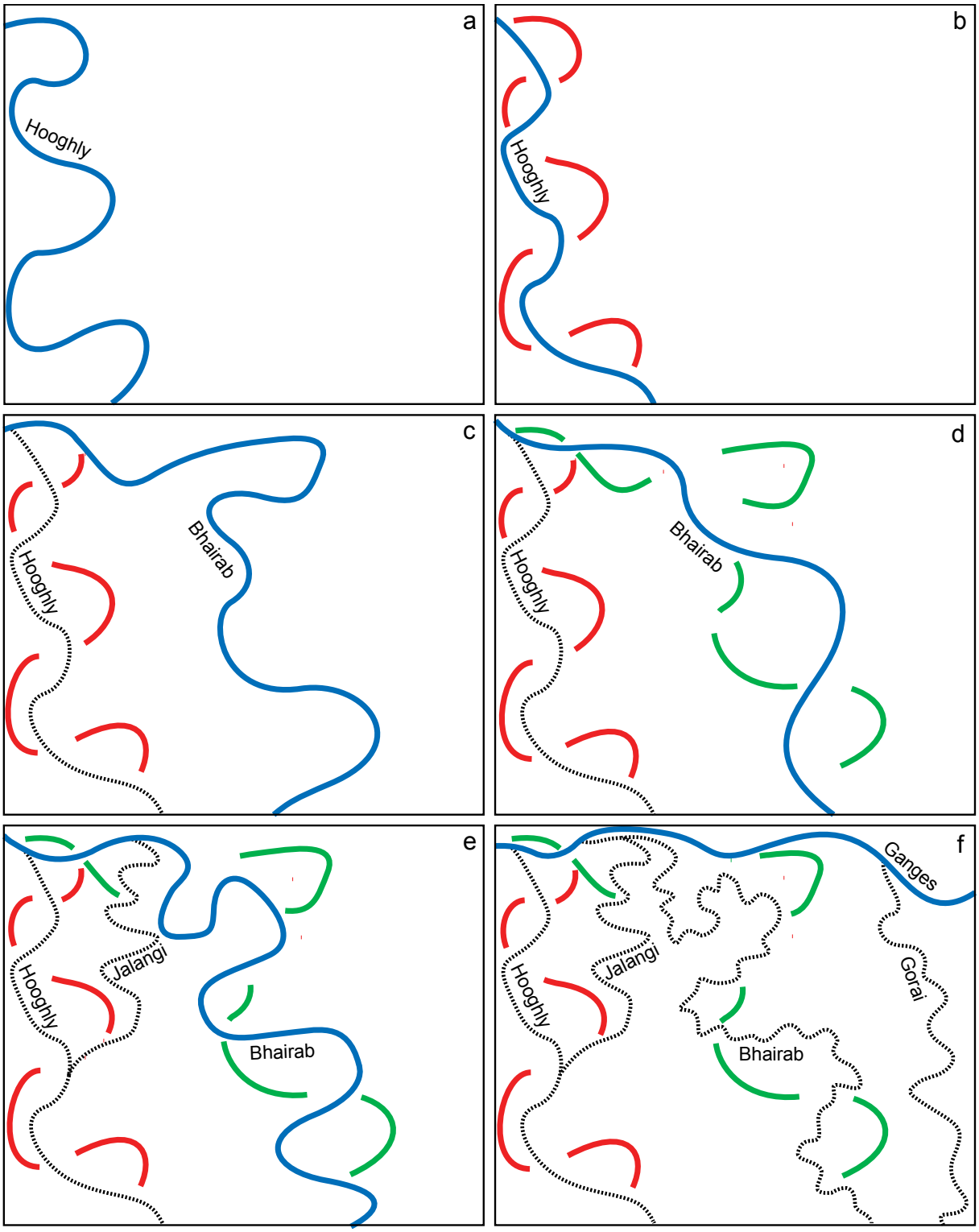

Figure 86: Sketches showing the hypothesized evolution of the major distributaries. The Ganges main course (blue) once followed the course of the present Hooghly (a). During a period of planform evolution large oxbow lakes (red) were formed (b). Then a fast evolved bifurcation resulted in a main course that roughly followed the present Bhairab course (c), with the Hooghly acting as a distributary (black dashed). Again a period of planform evolution caused large oxbow lakes (green) to be formed (d). Then a new, slowly evolving bifurcation, i.e. the Jalangi, caused the Bhairab to decrease in discharge and slowly change its wavelength accordingly (e). Before the Jalangi could fully develop as the main course a new bifurcation occurred more upstream that developed quickly (f), i.e. roughly the present Ganges in this area. Due to the fast nature of the bifurcation, meanders with a short wavelength were imposed on the large Bhairab meanders. After some time a new bifurcation developed more downstream of the Ganges, i.e. the Gorai. It is likely this branch never became the main course.

6.5 Proposed further research

In the study area many naturally meandering rivers are located and it is therefore a good area to develop the channel extraction method. However, the lack of ground truth was hampering the determination of the accuracy and a calibration of the subsequent meander geometry analysis. An important point for further research is therefore to determine the accuracy of the method by applying it in another study area for which more data is available, e.g. Alaska. Another possibility is to use experimental flume conditions. In that case one could precisely vary the amounts of discharge, the substrate, discharge regime etc. to obtain data that can be used in different conditions. However this must be done with care as possible scaling issues could yield useless results for an application on satellite images.

To improve the channel extraction method, the effect of using higher resolution satellite imagery is useful to explore. Using the Landsat 5 TM data results in issues with rivers that have a width around 30 m, with the largest effects occurring when the rivers follow a diagonal course through the image. Of course, using higher resolution images yields the same problems with smaller scale rivers that are undetected in this study. But if to extract rivers with a similar scale as in this study, it is expected to be a great improvement.

The spectral homogeneity of water is very high and therefore patches of consecutive water pixels will maintain a high homogeneity on high resolution images. Non-water pixel patches do not maintain the homogeneity to a similar extent as smaller scale variation in vegetation and soils becomes visible. Thus, the contrast in homogeneity between water and non-water pixel patches increases. This results in an improved distinction between water and non-water during the image segmentation. Furthermore, most channel objects will be several pixels in width. This is expected to diminish the issues that occur in this study with gaps in the network. It is even possible that it completely removes the issues, yielding a fully automated method for channel extraction. This hypothesis is fed by the fact that in this study the multiple pixels wide Hooghly, Jalangi and Gorai were easily classified at the largest segmentation scale with no gaps present at all. Important to note here is that of course gaps will always remain in the network if their cause is unrelated to the quality of the analysis, e.g. if they are due to the presence of cross-cutting or anthropogenic alterations.

6.6 Contribution to science

Many processes related to river dynamics are extensively researched to date. However, many of the exact physical processes that are involved are not entirely understood at present, e.g. those of bifurcation evolution. Further research in this field is aided by an

availability of great amounts of spatial and temporal data. This data was however not available and acquiring it with traditional at-site measuring is time and resource consuming. Furthermore, it was impossible to obtain historical data. Meaningful temporal data can only be obtained by performing measurements from present to a date in the far future, causing a great time-lag in research capability.

The method developed in this study can be used to overcome the problems related to data acquisition. If the accuracy is improved and a calibration is performed, the method can be used to obtain channel widths, sinuosity and discharge for large study areas in a quick, inexpensive and, most importantly, feasible manner. As historical satellite images are available for about 40 years back in time, it is also possible to directly obtain temporal data with such a time span.

The developed method does not have to be limited to an appliance in terrestrial research. For example, we have seen an increase in conducted research about Mars in the last decades. The main focus was to explore if water is or was present on the planet. Using remotely sensed images and digital elevation models scientist have found abundant fossil channels (Di Achille & Hynek, 2010). The geometry of these channels can be analysed by the developed method to explore the related discharges and to learn more about the Martian processes and their scales. However, a major difficulty with absolute discharges arises, as the empirical relations may not be valid on other planets due to differences in gravity.

7. CONCLUSIONS

- A nearly automated method for channel extraction is developed that is a great improvement over traditional pixel-based classification methods. Important improvements over existing object-based channel extraction methods are:
  - To merge the meander objects that result from different segmentation levels to obtain objects that represent large parts of the river network.
  - To process the polyline object skeletons to obtain channel centerlines.

- The extracted channels can be used to determine discharges and river dynamics in a study area by:
  - Determining the channel inflection points to approximate the meander wavelength.
  - Fitting splines to analyse the larger scale meandering of the general course of a river.
- The geometry analysis method appears to be relatively accurate, though the sparse ground truth causes the need for further calibration. Relative discharges of the rivers in the study area are thought to be accurate.

- The Hooghly and Bhairab are likely to have been the main course of the Ganges River for a significant amount of time.
- It is unlikely that the Jalangi and Gorai have been the Ganges main course, though they could have been important distributaries.

REFERENCES

Addink, E.A., S.M. De Jong & E.J. Pebesma. (2007), The importance of scale in object-based mapping of vegetation parameters with hyperspectral imagery. Photogrammetric Engineering and Remote Sensing 73(8), pp. 905-912.

Addink, E.A. & M.G. Kleinhans. (2008). Recognizing meanders to reconstruct river dynamics of the ganges. Paper presented at the GEOBIA 2008 - Pixels, Objects, Intelligence: GEOgraphic Object Based Image Analysis for the 21st Century, University of Calgary, Canada.

Ahmed, R. & S. Karmakar. (1993), Arrival and withdrawal dates of the summer monsoon in Bangladesh. International Journal of Climatology 13(7), pp. 727-740.

Aichholzer, O., F. Aurenhammer, D. Alberts et al. (1995), A Novel Type of Skeleton for Polygons. Journal of Universal Computer Science 1(12), pp. 752-761.

Anton, H., Bivens, I. & Davis, S. (2005). Calculus Early Transcendentals Single VariableJohn Wiley & Sons, New York.

Aslan, A., W.J. Autin & M.D. Blum. (2005), Causes of river avulsion: insights from the late Holocene avulsion history of the Mississippi River, USA. Journal of Sedimentary Research 75(4), pp. 650.

Baatz, M. & A. Schäpe. (2000), Multiresolution segmentation: an optimization approach for high quality multi-scale image segmentation. Journal of Photogrammetry and Remote Sensing 58(3-4)

Bangladesh Studies. (2006). Teacher Support - Topic 1 (b): Drainage system [online]. Retrieved June, 2011. Available on the world wide web:

<http://projects.cie.org.uk/banglao/textbook/environmentanddevelopment/physical/drainage>.

Benz, U.C., P. Hofmann, G. Willhauck et al. (2004), Multi-resolution, object-oriented fuzzy analysis of remote sensing data for GIS-ready information. ISPRS Journal of Photogrammetry and Remote Sensing 58(3-4), pp. 239-258.

Biswas, K. R. (2002). Rivers of Bengal vol. III, West Bengal District of Gazetteers, Kolkata.

Blaschke, T. (2010), Object based image analysis for remote sensing. ISPRS Journal of Photogrammetry and Remote Sensing 65(1), pp. 2-16.

Brice, J.C. (1974), Evolution of meander loops. Bulletin of the Geological Society of America 85(4), pp. 581.

Bridge, J. S. (2003). Rivers and floodplains: forms, processes, and sedimentary record. Blackwell Science, Oxford, pp. 491.

Camporeale, C., P. Perona, A. Porporato et al. (2005), On the long-term behavior of meandering rivers. Water Resources Research 41(12), pp. 1-13.

Carlston, C.W. (1965), The relation of free meander geometry to stream discharge and its geomorphic implications. American Journal of Science 263(10), pp. 864-885.

Chen, D. & J.G. Duan. (2006), Modeling width adjustment in meandering channels. Journal of Hydrology 321(1-4), pp. 59-76.

Constantine, J.A. & T. Dunne. (2008), Meander cutoff and the controls on the production of oxbow lakes. Geology 36(1), pp. 23.

Copeland, R., P. Soar & C. Thorne. (2005). Channel-forming discharge and hydraulic geometry width predictors in meandering sand-bed rivers. Paper presented at the 2005 World Water and Environmental Resources Congress, Anchorage, AK, pp. 568. Retrieved 30 June 2011.

Crist, E.P. & R.C. Cicone. (1984), A physically-based transformation of Thematic Mapper data---The TM Tasseled Cap. Geoscience and Remote Sensing, IEEE Transactions on(3), pp. 256-263.

Crosato, A. (2007), Effects of smoothing and regridding in numerical meander migration models. Water Resources Research 43(1)

Da Silva, A.M.F. (2006), On why and how do rivers meander. Journal of Hydraulic Research 44(5), pp. 579-590.

Davis, J. C. (2002). Statistics and data analysis in geology. New York City: John Wiley, pp. 638.

de Groot, J.K. & P. van Groen. (2001), The Gorai: Re-excavation project. Terra et Aqua(85), pp. 21-25.

Definiens AG. (2007). Developer 7 Reference Book.

Definiens AG. (2008), Definiens Enterprise Image Intelligence.

Di Achille, G. & B.M. Hynek. (2010), Ancient ocean on Mars supported by global distribution of deltas and valleys. Nature Geoscience 3(7), pp. 459-463.

Doyle, M.W., D. Shields, K.F. Boyd et al. (2007), Channel-forming discharge selection in river restoration design. Journal of Hydraulic Engineering 133, pp. 831.

Drăguţ, L., D. Tiede & S.R. Levick. (2010), ESP: A tool to estimate scale parameter for multiresolution image segmentation of remotely sensed data. International Journal of Geographical Information Science 24(6), pp. 859-871.

Dury, G.H. (1976), Discharge prediction, present and former, from channel dimensions. Journal of Hydrology 30(3), pp. 219-245.

Eaton, B.C., R.G. Millar & S. Davidson. (2010), Channel patterns: Braided, anabranching, and single-thread. Geomorphology 120(3-4), pp. 353-364.

Ferguson, R. (1987), Hydraulic and sedimentary controls of channel pattern. Inst. British Geographers Special Publication 18, pp. 129-158.

Ferguson, R.I. (1975), Meander irregularity and wavelength estimation. Journal of Hydrology 26 (3-4), pp. 315-333.

Goodbred Jr., S.L. & S.A. Kuehl. (2000), The significance of large sediment supply, active tectonism, and eustasy on margin sequence development: Late Quaternary stratigraphy and evolution of the Ganges-Brahmaputra delta. Sedimentary Geology 133(3-4), pp. 227-248.

Güneralp, I. & B.L. Rhoads. (2008), Continuous characterization of the planform geometry and curvature of meandering rivers. Geographical Analysis 40(1), pp. 1-25.

Hey, R.D. & C.R. Thorne. (1986), Stable channels with mobile gravel beds. Journal of Hydraulic Engineering 112(8), pp. 671-689.

Hickin, E.J. (1974), The development of meanders in natural river-channels. American Journal or Science 274, pp. 414-442.

Hildebrand, W.J. (1990), Connecting the Dots Parametrically: An Alternative to Cubic Splines. College Mathematics Journal 21(3), pp. 208-215.

Höfer, T. & B. Messerli. (2006), Floods in Bangladesh: history, dynamics and rethinking the role of the Himalayas. Ecology 29, pp. 254-283.

Hooke, J.M. (1984), Changes in river meanders: a review of techniques and results of analyses. Progress in Physical Geography 8(4), pp. 473-508.

Jian, J., P.J. Webster & C.D. Hoyos. (2009), Large-scale controls on Ganges and Brahmaputra river discharge on intraseasonal and seasonal time-scales. Quarterly Journal of the Royal Meteorological Society 135(639), pp. 353-370.

Kleinhans, M.G. (2005), Flow discharge and sediment transport models for estimating a minimum timescale of hydrological activity and channel and delta formation on Mars. Journal of Geophysical Research E: Planets 110(12), pp. 1-23.

Kleinhans, M.G. (2010), Sorting out river channel patterns. Progress in Physical Geography 34(3), pp. 287-326.

Kleinhans, M.G., H.R.A. Jagers, E. Mosselman et al. (2008), Bifurcation dynamics and avulsion duration in meandering rivers by one-dimensional and three-dimensional models. Water Resources Research 44(8).

Kleinhans, M.G. & J.H. van den Berg. (2011), River channel and bar patterns explained and predicted by an empirical and a physics-based method. Earth Surface Processes and Landforms 36(6), pp. 721-738.

Knighton, A.D. (1974), Variation in width-discharge relation and some implications for hydraulic geometry. Bulletin of the Geological Society of America 85(7), pp. 1069.

Kraaijenbrink, P.D.A. (2010). Reconstructing river dynamics of the Gorai with object-based image analysis. Bachelor thesis, Utrecht University), pp. 37.

Langbein, W. B. & Leopold, L. B. (1966). River meanders-theory of minimum variance. United States Government Printing Office, Washington, pp 19.

Leopold, L.B. & M.G. Wolman. (1960), River meanders. Geological Society of America Bulletin 71(6), pp. 769.

Leopold, L. B., Wolman, M. G., Wolman, M. G. & Wolman, M. G. (1957). River channel patterns: braided, meandering, and straight. US Govt. Print. Off, Washington, pp. 49.

Lillesand, T. M., Kiefer, R. W. & Chipman, J. W. (2003). Remote sensing and image interpretationJohn Wiley & Sons New York. pp. 763.

Maniruzzaman, M. (2008). Need for codifying international law/obligations for ensuring environmental flow downstream: Lessons from Bangladesh. Paper presented at the IWRA World Water Congress 2008, Montpellier, France.

Mertes, L.A.K. (2002), Remote sensing of riverine landscapes. Freshwater Biology 47(4), pp. 799-816.

Mirza, M.M.Q. (2004). The Ganges water diversion: Environmental effects and implications. Kluwer Academic Publishers, New York, pp. 373.

Mirza, M.M.Q. (1997), Hydrological changes in the Ganges system in Bangladesh in the post-Farakka period. Hydrological Sciences Journal 42(5), pp. 613-631.

Rhoads, B.L. & M.R. Welford. (1991), Initiation of river meandering. Progress in Physical Geography 15(2), pp. 127.

Rudra, K. (2010), Dynamics of the Ganga in West Bengal, India (1764-2007): Implications for science-policy interaction. Quaternary International 227(2), pp. 161-169.

Sarkar, A., S. Sengupta, J.M. McArthur et al. (2009), Evolution of Ganges-Brahmaputra western delta plain: Clues from sedimentology and carbon isotopes. Quaternary Science Reviews 28(25-26), pp. 2564-2581.

Sarker, M. (2005). Impact of upstream human interventions on the morphology of the Ganges-Gorai system. pp. 49-80.

Sarker, M., M.M. Kamal & K. Hassan. (1999). Identifying the morphological changes of a distributary of the ganges in response to the declining flow using remote sensing. Paper presented at the Asian Conference for Remote Sensing, Hong Kong, China.

Schumm, S.A. (1967), Meander wavelength of alluvial rivers. Science 157(3796), pp. 1549.

Schuurman, F. (2008). Dynamics of Sharp Meander Bends on an Intertidal Mudflat. Master of Science thesis, Utrecht University.

Slingerland, R. & N.D. Smith. (1998), Necessary conditions for a meandering-river avulsion. Geology 26(5), pp. 435-438.

Slingerland, R. & N.D. Smith. (2004), River avulsions and their deposits. Annual Review of Earth and Planetary Sciences 32, pp. 257-285.

Stouthamer, E. & H.J.A. Berendsen. (2001), Avulsion frequency, avulsion duration, and interavulsion period of holocene channel belts in the Rhine-Meuse delta, the Netherlands. Journal of Sedimentary Research 71(4), pp. 589-598.

The Mathworks. (2011), MATLAB 2011b. Natick, MA, USA.

Trimble. (2009), eCognition Developer 8. Sunnyvale, CA, USA.

Umitsu, M. (1993), Late quaternary sedimentary environments and landforms in the Ganges Delta. Sedimentary Geology 83(3-4), pp. 177-186.

USGS. (2012). Global Visualization Viewer [online]. Retrieved December 12, 2011. Available on the world wide web: <http://glovis.usgs.gov/>.

van der Werff, H.M.A. & F.D. van der Meer. (2008), Shape-based classification of spectrally identical objects. ISPRS Journal of Photogrammetry and Remote Sensing 63(2), pp. 251-258.

Vyatkina, K. (2008). On the structure of straight skeletons. Paper presented at the International Conference on Computational Sciences and its Applications, ICCSA 2008, Perugia, pp. 452-460.

Williams, G.P. (1986), River meanders and channel size. Journal of Hydrology 88(1-2), pp. 147-164.

Yang, C.T. (1971), On river meanders. Journal of Hydrology 13, pp. 231-253.

Yuan, D. & C.D. Elvidge. (1996), Comparison of relative radiometric normalization techniques. ISPRS Journal of Photogrammetry and Remote Sensing 51(3), pp. 117-126.